Mineral Chemistry and Sulfur Isotope Insights into Magmatic and Hydrothermal Processes Leading to Porphyry Cu Mineralization at Grasberg, Indonesia

By

ADI SULAKSONO

Dissertation

In Partial Fulfillment of the Requirements for the Degree of

"Doctor of Science"

Graduate School of International Resource Sciences

AKITA UNIVERSITY

March 2021

Statement by Author

This dissertation is deposited in the University Library to be made available to readers under the rules of the Library. Brief quotations from this dissertation are allowable without special permission, provided accurate acknowledgement of source is made. Request for permission for extended quotation from or reproduction of this manuscript in whole or in part may be granted by the author.

Signed: Adi Sulaksono

Date: 01/03/2021

Approval by Research Committee

As members of the Research Committee, we recommend that the following thesis:

Mineral Chemistry and Sulfur Isotope Insights into Magmatic and Hydrothermal Processes Leading to Porphyry Cu Mineralization at Grasberg, Indonesia

be accepted as fulfilling the research requirement for the degree of "Doctor of Science".

Prof. Yasushi Watanabe (Major Advisor)

Prof. Andrea Agangi

Prof. Tsukasa Ohba

Prof. Antonio Arribas

Date: 01/03/2021

Dedication

To my parents, wife and son.

Acknowledgement

Foremost I would like to express my gratitude to my major advisor Prof. Yasushi Watanabe, who accepted me as his student. More importantly, his guidance and support were invaluable to me. I would also like to acknowledge helpful contributions from supervising committee members: Prof. Antonio Arribas, Prof. Andrea Agangi and Prof. Tsukasa Ohba. None of this project would have been completed without Takuya Echigo, Keiko Hattori, Jeffrey Hedenquist, Samuel Morfin, Shogo Aoki, Osamu Nishikawa, Ryohei Takahashi, Hinako Sato, Pearlyn Manalo, Renaldi Suhendra and Mayuko Fukuyama. They contributed to many discussions and analytical works that helped to shape this project. This project was completed with the help of many geologists and support staff in PT Freeport Indonesia and PT Eksplorasi Nusa Jaya. This study was funded by the Leading Program of Akita University, and the fieldwork component was supported by PT Freeport Indonesia and PT Eksplorasi Nusa Jaya.

Abstract

Preparation for sufficient amounts of Cl, S and metals during magma evolution is of paramount importance for the generation of porphyry Cu deposits. Reduction of oxidized S is essential for precipitation of sulfides in such deposits, in which mineralization predominantly comprises Cu sulfides, whereas their source magmas are oxidized with most of their S as SO_4^{2-} and with exsolved fluids having SO_2>>H_2S. I explore how magma evolution and oxidation state affected the degassing of Cl- and S-bearing fluids from the source magma at Grasberg, based on igneous mineral paragenesis and amphibole, zircon and apatite chemistries. The process of S reduction required for sulfide mineralization during hydrothermal processes is also evaluated in this study on the basis of S isotope and biotite chemical composition.

The low-Al amphiboles formed at approximately 730–700 °C, 1.1–0.7 kbar and FMQ+3.4 are contained in the syn-mineralization Main Grasberg Intrusion (MGI). The MGI magmatism was followed by the emplacement of the syn-mineralization Early South Kali Dike (ESKD) that contains amphibole with a disequilibrium texture of chemically distinct core and rim; the high-Al cores crystallized at approximately 900–850 °C, 4.3–3.3 kbar and FMQ+1, whereas the low-Al rims and associated low-Al amphibole phenocrysts formed at approximately 790–720 °C, 1.9–1.0 kbar and FMQ+2.7. The high-Al amphibole is anhydrite-, titanite-magnetite-quartz- and zircon-free, whereas the low-Al amphibole hosts inclusions of, and/or is associated with such minerals that indicate a high magma oxidation state. The low-Al amphiboles of both MGI and ESKD are

characteristically low in REE+Y (particularly MREE) and V, and having large negative Eu, Ba, and Sr anomalies compared with the ESKD high-Al amphiboles. This confirms that the low-Al amphibole crystallized from a melt in equilibrium with plagioclase, K-feldspar, biotite, titanite (-magnetite-quartz), zircon, apatite and anhydrite, at lower pressure and temperature and higher fO_2 than the conditions for the high-Al amphibole. Zircons from the MGI yield the elevated mean Ce^{4+}/Ce^{3+} value of 519, whereas the ESKD zircons record a lower value of 248. Zircon Ce/Ce*, Ce/Nd and Eu/Eu* values also indicate that the MGI magma was more oxidized than the ESKD. The changes in melt Cl and S concentrations calculated from apatite chemistry indicate a degassing sequence which can be divided into: 1) degassing of Cl from the MGI magma after low-Al amphibole and plagioclase crystallizations, 2) degassing of S from the ESKD magma at ~800 °C and ~2 kbar, prior to the crystallizations of low-Al amphibole and plagioclase, 3) degassing of Cl from the ESKD magma after low-Al amphibole and plagioclase crystallizations.

Initial hydrothermal events formed sulfide-free, anhydrite-rich K-feldspar and biotite alteration, followed by successive vein stages of 1) magnetite, 2) biotite, 3) quartz, 4) anhydrite-chalcopyrite, 5) chalcopyrite ± sericite selvages, and 6) pyrite-chalcopyrite- quartz + sericite selvages. Hydrothermal biotite within the potassic alteration zone is characterized by higher Mg# and lower Fe contents than igneous biotite. The ranges of $\delta^{34}S$ values of S-bearing minerals hosted in the anhydrite-chalcopyrite veins are 1.2–4.2‰ for chalcopyrite (n=24; avg. 2.3‰), 1.1 and 2.1‰ for bornite (n=2) and 10.5–13.8‰ for anhydrite (n=26; avg. 12.2‰). Two chalcopyrite samples that occur along the centerlines of comb-textured quartz veins

have $\delta^{34}S$ values of 2.4 and 2.5‰ (n=2). One chalcopyrite vein that is accompanied by sericite alteration has $\delta^{34}S$ = 2.1‰. The $\delta^{34}S$ values for pyrite in a veinlet with sericite selvage are 2.8 to 4.8‰ (n=3; avg. 3.7‰), and those of anhydrite are 14.6–15.2‰ (n=2). A sample of the syn-mineralization ESKD MD yields a $\delta^{34}S$ of 9.4‰.

The combined igneous mineral paragenesis and geochemistry indicate that a less oxidized magma batch containing high-Al amphibole injected into a strongly oxidized MGI-related upper-crustal magma chamber, forming a hybrid magma from which the ESKD porphyry was derived. The degassing of Cl both from MGI and ESKD magmas is likely related to the crystallization of phenocryst in the upper crust, whereas the partitioning of S from the ESKD magma into fluids may require another process that occurs at higher pressure and temperature, prior to the crystallization of phenocrysts in the upper crustal magma chamber. I suggest that mixing of magmas of two distinct oxidation states generated SO_2 by the reduction of sulfate from the oxidized magma via oxidation of Fe^{2+} derived from the other reduced or less oxidized magma:

$$CaSO_4 + 2FeO = CaO + SO_2 + 2FeO_{1.5}$$

Magmatic degassing that occurred intermittently at Grasberg implies that localized accumulation of ore-forming fluids before a sudden discharge is required for an efficient hydrothermal system. Ore-forming fluids may have been accumulated and stored in a stable fluid pocket beneath the cupola zone before a sudden discharge. Such a short-lived fluid discharge is in agreement with the fact that most porphyry deposits occur in a short period of time (<100 k.y.) compared to their associated

magmatic systems.

Just after the discharge, S is not ready for economic mineralization due to its unsuitable valences (SO_2>>H_2S). The $\delta^{34}S$ values of sulfide-sulfate mineral pairs indicate SO_2-derived SO_4^{2-} and H_2S in SO_4^{2-}/H_2S molar proportions of ~4:1 to ~3:1 at >550 °C. The hydrothermal fluid then likely followed a rock-buffered trajectory and became more reduced at <550 °C. Hydrothermal biotite that replaces igneous amphibole and biotite has a phlogopitic composition, suggesting that Fe^{2+} was liberated from igneous mafic minerals and oxidized by reaction with SO_4^{2-} to form magnetite, resulting in sulfide formation by the simplified reaction:

$$12FeO + SO_4^{2-} + 2H^+ \rightarrow 4Fe_3O_4 + H_2S$$

Table of Contents

List of Figures

List of Tables

Chapter 1: Introduction

The skarn-style ore mineralization of the Ertsberg deposit was first observed and sampled in 1936 by Jacques J. Dozy, a Dutch geologist who explored the district on an expedition to the Carstensz glacier (Dozy et al., 1939). Ertsberg was surveyed again in the early 1960s by Forbes Wilson and Delos Flint of the Freeport Sulphur Company (Wilson, 1981). The development of Ertsberg open pit mine began in 1969 (Wilson, 1981), where production continued until 1989 (Leys et al., 2012). Grasberg was discovered by PT Freeport Indonesia in 1988 when the vertical drill hole of GRS-4 encountered 600 m averaging 1.65% Cu and 1.4 g/t Au (Van Nort et al., 1991; MacDonald and Arnold 1994). Ore production began in December of 1989 (Leys et al., 2012).

The Grasberg porphyry Cu-Au deposit (Fig. 1) is the world's largest Au-rich porphyry Cu deposit (Cooke et al. 2005) and is also associated with large proximal and distal skarn deposits. On the basis of a non-economic cutoff grade of 0.1% Cu, the Grasberg-related system (the Grasberg porphyry Cu-Au and the Kucing Liar skarn) contains 7.5 billion tons of ore at 0.7 % Cu and 0.64 ppm Au (Leys et al. 2012) for a contained 52.5 Mt Cu and 4,800 t (154 Moz) Au.

Porphyry Cu systems are genetically related to oxidized intermediate to felsic magmas (Ishihara, 1977; Hedenquist and Lowenstern, 1994; Sillitoe, 2010; Richards, 2015; Hattori, 2018). These magmas generate in magmatic arcs where the oceanic plate and overlying sediments subduct and transfer water and soluble components into the overlying mantel wedge (Hildreth and Moorbath 1988; Tatsumi, 1989; Mungall 2002). Hydrous mafic magmas from the mantle wedge is

transferred into MASH (melting, assimilation, storage, homogenization) zones, followed by ascent of magmas to the upper crust to form batholiths at depths of approximately 5 to 10 km from which a small proportion of the magma and most of the volatile rises toward the surface (Sillitoe 2010; Wilkinson 2013; Richards, 2018). Porphyry Cu deposits form in the cupola zone at 2–5 km depth, where bubbly magma and ore-forming fluids are channeled (Burnham, 1979; Shinohara and Hedenquist, 1997; Cloos, 2001; Weis, 2015; Richards 2018). In this zone, supercritical fluids and high-density vapors can efficiently transport metals such as Cu, Mo and Au and produce porphyry Cu-type mineralization (Cline and Bodnar, 1991; Muntean and Eunadi, 2000; Rusk et al., 2008).

Chlorine and S are critical elements of porphyry-related fluids due to their role in complexing, transporting and precipitating metals such as Cu and Au (Candela and Holland, 1984; Williams et al., 1995, 1997; Simon et al., 2004, 2006; Pokrovski et al., 2015; Tattitch and Blundy, 2017). I revisit the Grasberg porphyry Cu-Au deposit located in the Ertsberg-Grasberg mineral district in the province of Papua, Indonesia (Fig. 2A) to investigate if and how magmatic evolution and oxidation state affect the degassing of volatiles from the source magma in this setting. I present igneous mineral paragenesis and compositions of amphibole and zircon to establish the physicochemical conditions of the parent magmas at Grasberg. The calibrated thermodynamic apatite/melt S and Cl partitioning models (Parat el al., 2011; Li and Hermann, 2017) are applied to monitor the fluctuation of S and Cl concentrations in the melt during magma evolution. The combined physical and chemical data are then utilized to discuss the evolution of the magma, timing and

the mechanisms that govern the separation of metalliferous fluids from the melt to form porphyry Cu deposit.

The hydrothermal fluids exsolved from oxidized magmas are expected to have a high oxidation state, similar to that of their parental magmas (Richards 2015). However, the bulk of porphyry Cu mineralization occurs as Cu sulfides (i.e., reduced sulfur species). Recent studies at Grasberg indicate that the disproportionation of SO_2 gas by a Ca-bearing phase could have increased the concentration of H_2S in hydrothermal fluids that combined with dissolved base metals to precipitate sulfide mineralization (Henley et al. 2015; Mavrogenes and Blundy 2017; Henley and Seward 2018). Liang et al. (2009) proposed an alternative process at the Yulong porphyry Cu-Au deposit in China where large amounts of H_2S required to precipitate abundant Cu-Fe-sulfides were formed by the reduction of aqueous SO_4^{2-} via oxidation of Fe^{2+} in mafic minerals to Fe^{3+}. To understand how oxidized sulfur is reduced to form porphyry Cu mineralization, this study aims to measure the evolution of the redox state of sulfur in Grasberg to determine its role in deposit formation. I start by documenting the Grasberg hydrothermal vein and wallrock alteration sequence from petrography, mineral chemistry, magnetite content (from magnetic susceptibility), and sulfur isotopes of drill core samples spanning a ~2 km depth range through the deposit. I then use the paragenetic sequences to investigate the source of SO_4^{2-} in the hydrothermal fluids and discuss the sulfur reduction processes that formed the deposit.

Figure 1. 2006 aerial photograph of the Grasberg open pit mine (internal report by PT Freeport Indonesia; photo by Aditya W. Pringgoprawiro).

Chapter 2: Geological Background

2.1. District geology

The New Guinea island is subdivided into four tectonic provinces from south to north (Fig. 2A; Hamilton, 1979; Cooper and Taylor, 1987; Sapiie and Cloos, 2004): (1) the New Guinea foreland that is underlain by the Australian continent, (2) the Central Range fold-and-thrust belt, (3) the metamorphic belt, overlain by an ophiolite complex and (4) the Melanesian arc terrane. The Ertsberg-Grasberg mineral district lies within the Central Range fold-and-thrust belt. This district contains deformed Cretaceous and Tertiary sedimentary rocks (Fig. 2B; Sapiie and Cloos, 2004) that are cut by Pliocene intrusions. Magmatism in the district was previously believed to be the result of subduction at the New Guinea trench, following a convergence reversal event (Dewey and Bird, 1970; Hamilton, 1979). However, Cloos et al. (2005) proposed that the north-dipping slab of the oceanic end of the Australian plate subducting beneath the Pacific plate broke off and continued to sink after collision jammed the subduction zone, which began at approximately 8 Ma.

Most of the porphyry-style mineralization in the Grasberg-Ertsberg district is associated with Pliocene igneous breccias and intrusions of the Grasberg Igneous Complex (GIC) (Peterson and Cloos, 2005) that were emplaced into mainly siliciclastic Cretaceous Kembelangan Group and carbonate-dominated Tertiary New Guinea Limestone Group rocks (Figs. 2B, 3; Leys et al., 2012). The GIC consists of several igneous units (MacDonald and Arnold 1994; McMahon 1999)

that are divided into the following units: pre-mineralization Dalam Igneous Complex (DIC), which is composed of minor subaerial volcanics, near-surface breccias and deeper intrusions interpreted by MacDonald and Arnold (1994) to represent a maar diatreme complex; Main Grasberg Intrusion (MGI), immediately before the mineralization; syn-mineralization Early South Kali Dike (ESKD) and the post-mineralization Late South Kali Dike (LSKD). Zircon U-Pb geochronology shows that the pre-mineralization DIC magmatism occurred between 3.60 and 3.30 Ma and was followed by emplacement of the MGI at 3.22 ± 0.04, ESKD at 3.20 ± 0.04 and LSKD at 3.09 ± 0.05 Ma respectively (Wafforn, 2017). Field relationships indicate that an earlier porphyry Cu-Mo mineralizing event predates MGI emplacement, but porphyry Cu-Au mineralization closely post-dates the MGI, overlaps the ESKD and predates the LSKD (Leys et al., 2012).

2.2. Alteration and mineralization

The Grasberg porphyry deposit is dominated by a sub-vertical, cylindrical zone of potassic alteration centered on the MGI that is surrounded by a selvage of sericite alteration that extends to the margins of the GIC. The highest Cu grades (>2% Cu) are associated with the strongest and most pervasive potassic, and to a lesser extent sericite alteration zones. These alteration zones are patchily overlap the margins of the ESKD but are truncated by the LSKD (Leys et al., 2012).

Potassic alteration is dominated by K-feldspar, biotite, magnetite, quartz and anhydrite. Chalcopyrite is the main ore mineral in the potassic alteration zone. It occurs mainly in anhydrite-rich vein (Fig. 4A), in the center of inward-growing

symmetric quartz vein (Fig. 4B), as monomineralic chalcopyrite vein and as dissemination in the host rocks (Fig. 4C). Bornite is associated with chalcopyrite, but subordinate in amount. The amount of bornite increases with depth (Leys et al., 2012). In general, the the amount of Cu sulfides in the potassic alteration zone has a positive correlation with the abundance of hydrothermal magnetite, which is inversely correlated with the abundance of hydrothermal anhydrite. The majority of Au in the potassic alteration occurs as free inclusions in chalcopyrite, bornite and digenite (MacDonald and Arnold, 1994; Rubin, 1996). Gold is typically of high fineness (Leys et al., 2012).

Sericite alteration comprises white mica, quartz, chlorite, anhydrite, pyrite, chalcopyrite, bornite, covelite, apatite and rutile. This alteration typically replaces plagioclase and K-feldspar in centimeter-scale alteration selvages to 1–10 mm-wide quartz-pyrite-chalcopyrite and chalcopyrite veins.

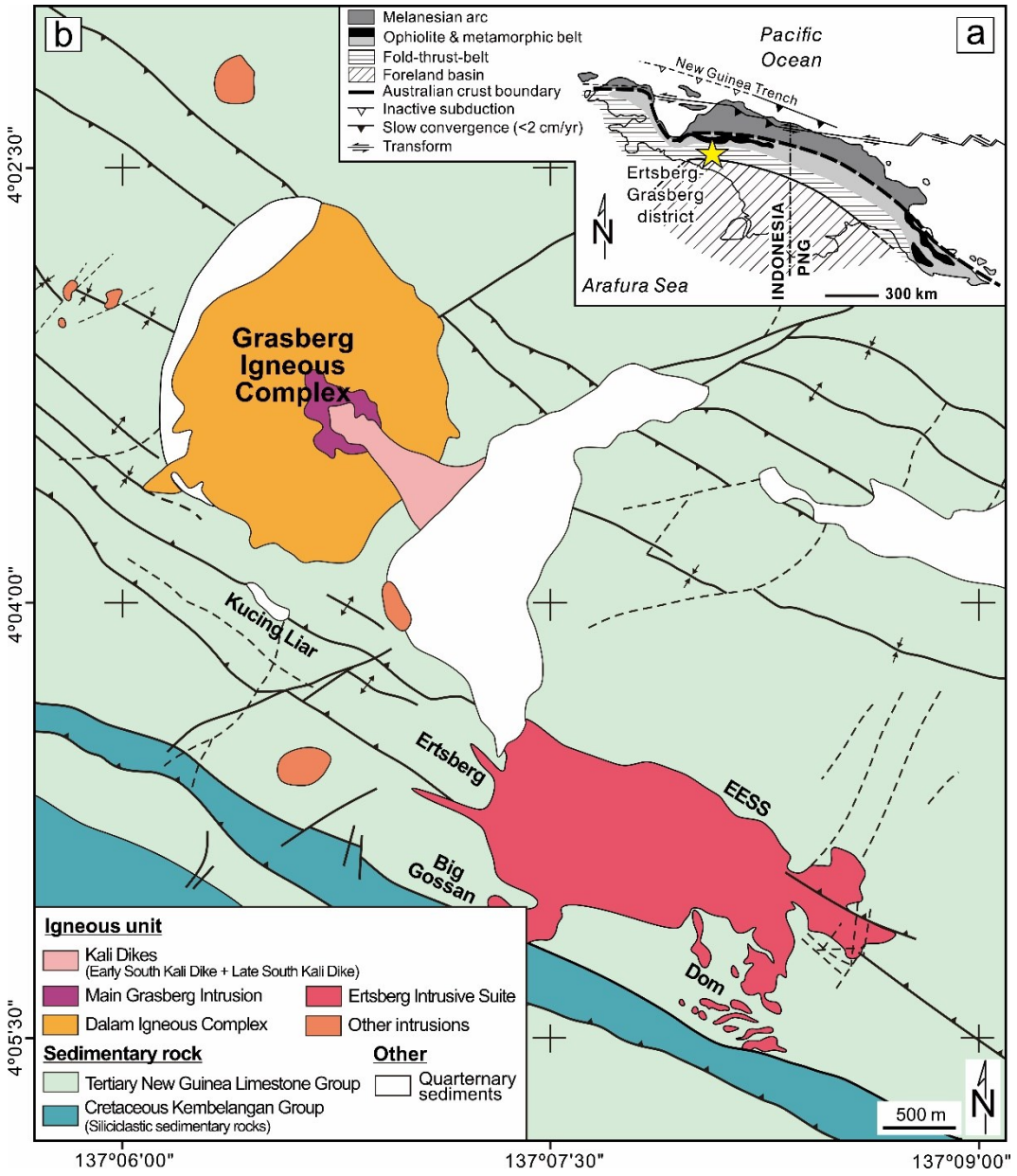

Figure 2. (A) Lithotectonic map of the island of New Guinea (modified from Sapiie and Cloos, 2004). (B) Geological map of the Erstberg-Grasberg district modified from Leys et al (2012) after New (2006). The Grasberg porphyry Cu-Au deposit is hosted by the GIC. Also shown are locations of skarn ore bodies: Kucing Liar, Ertsberg, Ertsberg East skarn system (EESS), Big Gosan and Dom.

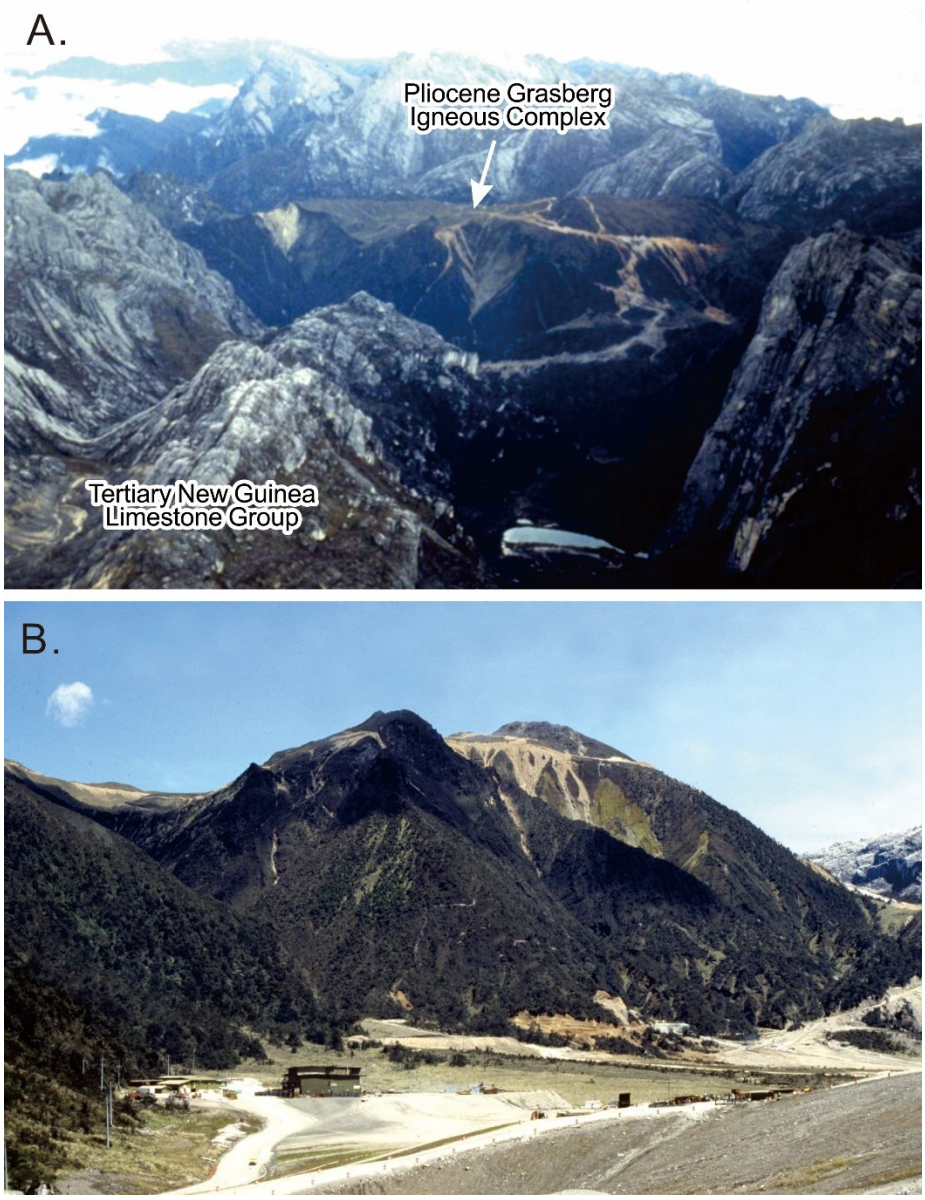

Figure 3. A. 1990 view to the NW from near Puncak Jaya (internal report by PT Freeport Indonesia). B. Grasberg in 1990 (4150 m elevation; internal report by PT Freeport Indonesia)

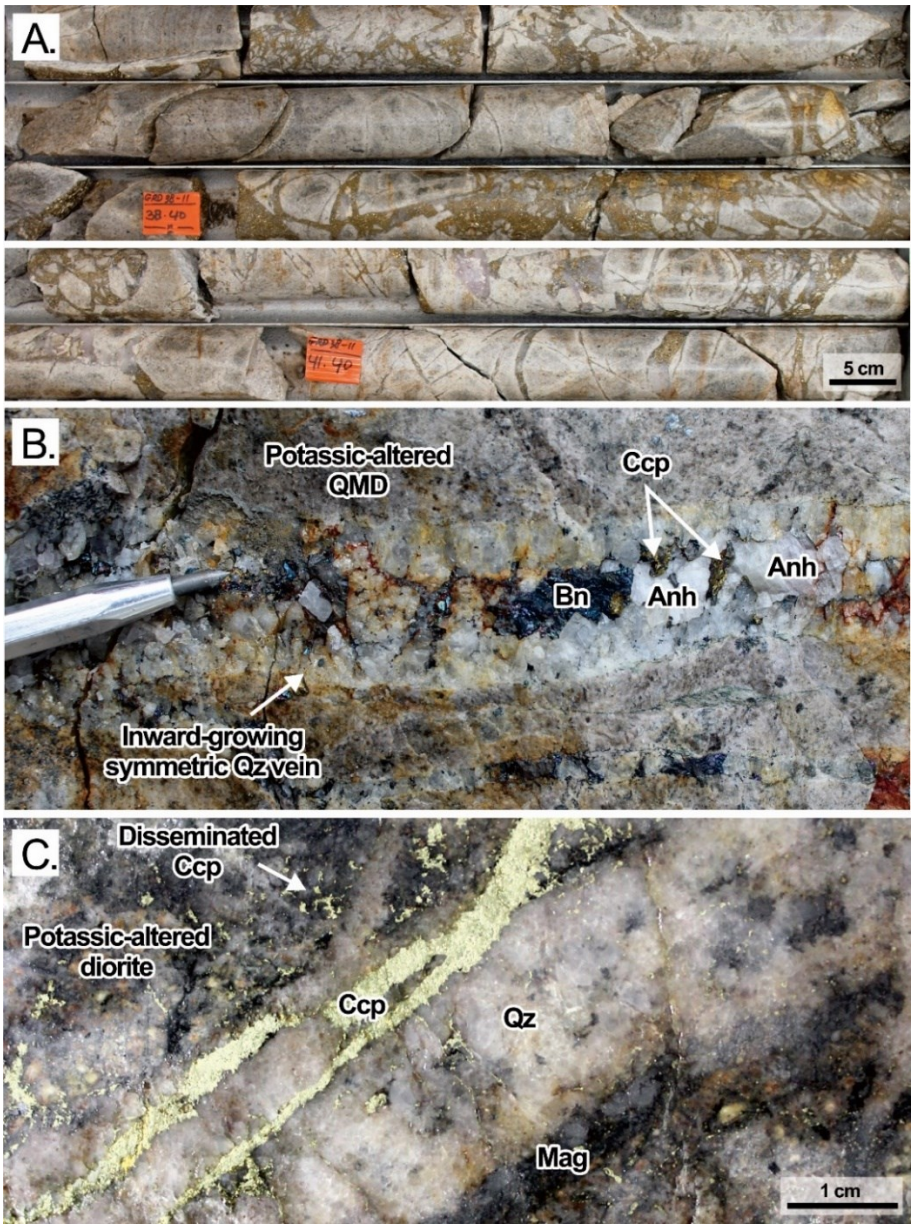

Figure 4. Copper mineralization at Grasberg. (A) Anhydrite-chalcopyrite vein occurs as a matrix in the brecciated DIC diorite. (B) Chalcopyrite in the opening of inward-growing quartz vein. (C) Monomineralic chalcopyrite vein cutting the previously formed quartz vein. Also shown is the disseminated chalcopyrite in the potassic-altered diorite wall rock. Mineral abbreviations: Amp, amphibole; Anh, anhydrite; Ap, apatite; Bt, biotite; Bn, bornite; Ccp, chalcopyrite; Kfs, K-feldspar; Mag, magnetite; Pl, plagioclase; Py, pyrite; Qz, quartz; Ser, sericite; Ttn, titanite; Zrn, zircon.

Chapter 3: Magma Redox and Degassing of Volatiles

3.1. Samples and analytical methods

For this study, 12 igneous rock samples were collected from drill holes GRD38-11, GRD39-01, GRD42-06 and KL98-10-21. These samples represent a ~1600 m vertical sampling span within the Grasberg system (Fig. 5). The abundance, texture and paragenesis of igneous minerals were determined on the basis of thin-section observation. Bulk rock geochemical analyses were carried out at Activation Laboratories (analytical codes: 4B ICP-OES and 4F C, S; LOI = H_2O + C + S) and using Agilent Technologies 7500 Series Inductively Coupled Plasma Mass Spectrometry (ICP-MS) at Akita University for major and trace elements, respectively. Major elements in amphibole and apatite were analyzed using electron microprobe at Akita University. Laser ablation ICP-MS (LA-ICP-MS) analyses of trace element in amphibole were performed at Okayama University of Science. Zircon grains were mounted in epoxy pucks and were imaged using scanning electron microscope (SEM) in cathodoluminescence (CL) mode at Akita University. LA-ICP-MS analyses were conducted on selected zircon grains at the University of Ottawa.

1. Amphibole

Thin sections were examined using a Nikon ECLIPSE LV100N POL microscope and a JEOL® JSM-6610 LV scanning electron microscope equipped with an Oxford X-MaxN energy-dispersive X-ray detector at Akita University (accelerating voltage

= 15 kV, beam current = 2.2 nA). Quantitative mineral microanalyses were conducted using a JEOL® JXA-8230 SuperProbe at Akita University with an accelerating voltage of 15 kV, a 20 nA beam current, and a 5 μm electron beam size. Astimex Inc., USA mineral standards were used such as fluorite (F), jadeite (Na), periclase (Mg), An65 plagioclase (Al and Ca), quartz (Si), tugtupite (Cl), orthoclase (K), rutile (Ti,), rhodonite (Mn) and hematite (Fe) for biotite and amphibole. All analytical data were corrected using the ZAF matrix-correction program.

Amphibole trace element analyses were performed using a Teledyne Cetac Technologies Analyte G2 193 nm laser ablation system coupled to a Thermo Fisher Scientific iCAP-RQ ICP-MS at the Okayama University of Science. For the amphibole samples, the following elements were monitored: ^{7}Li, ^{29}Si, ^{42}Ca, ^{51}V, ^{59}Co, ^{60}Ni, ^{63}Cu, ^{66}Zn, ^{85}Rb, ^{88}Sr, ^{89}Y, ^{90}Zr, ^{93}Nb, ^{95}Mo, ^{147}Ba, ^{139}La, ^{140}Ce, ^{141}Pr, ^{146}Nd, ^{147}Sm, ^{151}Eu, ^{157}Gd, ^{159}Tb, ^{163}Dy, ^{165}Ho, ^{167}Er, ^{169}Tm, ^{173}Yb, ^{175}Lu, ^{177}Hf, ^{208}Pb, ^{232}Th, and ^{238}U. NIST SRM 610 was used as the primary standard to calculate elemental concentrations (using ^{29}Si as the internal standard element). At the sample ablation, the laser fluence was set to 7.92 J/cm^2 at the sample surfaces with a laser repetition rate and laser diameter set to 5 Hz and 35 μm, respectively. Raw data were reduced using Thermo Scientific Qtegra Intelligent Scientific Data Solution (ISDS) platform software. The elemental concentrations of the amphiboles were finally calculated using an in-house Microsoft Excel spreadsheet.

2. Apatite

The occurrences of apatite were observed using a Nikon ECLIPSE LV100N POL microscope and a JEOL® JSM-6610 LV scanning electron microscope equipped with an Oxford X-MaxN energy-dispersive X-ray detector at Akita University (accelerating voltage = 15 kV, beam current = 2.2 nA). Systematic quantitative mineral microanalyses were conducted using a JEOL® JXA-8230 SuperProbe at Akita University with an accelerating voltage of 15 kV, a 20 nA beam current, and a 5 μm electron beam size. Astimex Inc., USA mineral standards were used such as fluorite (F), albite (Na), periclase (Mg), An65 plagioclase (Al and Ca), quartz (Si), apatite (P), celestite (S), tugtupite (Cl), rutile (Ti,) and rhodonite (Mn) for apatite. All analytical data were corrected using the ZAF matrix-correction program. Pulse height analyzer (PHA) was used to avoid the overlap between S and F.

3. Zircon

Zircons from six samples representing all the major porphyry intrusions were prepared for this study. Rock samples were prepared in a steel jaw crusher and steel disk grinder to a powder. A traditional panning methods was used on the <500-μm-size fraction to produce a heavy mineral concentrate, from which zircons were picked under binocular microscope. Careful cleaning was performed such as using water and alcohol to minimize possibility of cross sample contamination.

Separated zircon grains mounted in epoxy pug were polished to expose grain centers. The grains were then imaged using a CL detection system at Akita University using a JEOL scanning electron microscope JSM‐6610LV, equipped with a Gatan Mini‐CL detector and photomultiplier. Most zircons have a

combination between oscillatory and sector zonings. Inherited cores, fractures and melt and mineral inclusions are common. Inherited cores are differentiated from their rim overgrowths by irregular or dissolution boundaries, which truncate internal zoning or separate unzoned or chaotically zoned cores from growth zoned rims. Apatite inclusions are common, and were avoided for LA-ICP-MS analysis because they can cause unrealistically high LREE concentrations. Oscillatory-zoned zircons with no or minor combination of sector zoning were also selected to avoid a significant variation in trace element concentrations in a single zircon crystal.

All zircon trace element analyses were conducted using a Teledyne Cetac Technologies Analyte Excite 193 nm excimer laser ablation system coupled with an Agilent 7700x ICP-MS at the University of Ottawa. Zircons were analyzed for the following isotope masses: ^{29}Si, ^{31}P, ^{42}Ca, ^{45}Sc, ^{49}Ti, ^{56}Fe, ^{88}Sr, ^{89}Y, ^{91}Zr, ^{95}Mo, ^{139}La, ^{140}Ce, ^{141}Pr, ^{146}Nd, ^{147}Sm, ^{151}Eu, ^{157}Gd, ^{159}Tb, ^{163}Dy, ^{165}Ho, ^{167}Er, ^{169}Tm, ^{173}Yb, ^{175}Lu, ^{177}Hf, ^{206}Pb, ^{232}Th, and ^{238}U. NIST SRM 612 was used as the primary standard to calculate elemental concentrations (using ^{29}Si as the internal standard element). The zircons were ablated by a laser with a repetition rate of 12 Hz, a energy of 5.9 J/cm^2, and a diameter of 32 μm. Raw counts for trace elements were reduced using the GLITTER! software (Griffin et al., 2008). Sample analyses were discarded if an inclusion was detected by the GLITTER! software, using ^{31}P, ^{42}Ca or ^{56}Fe as proxies for common zircon inclusions (apatite and Fe-oxides).

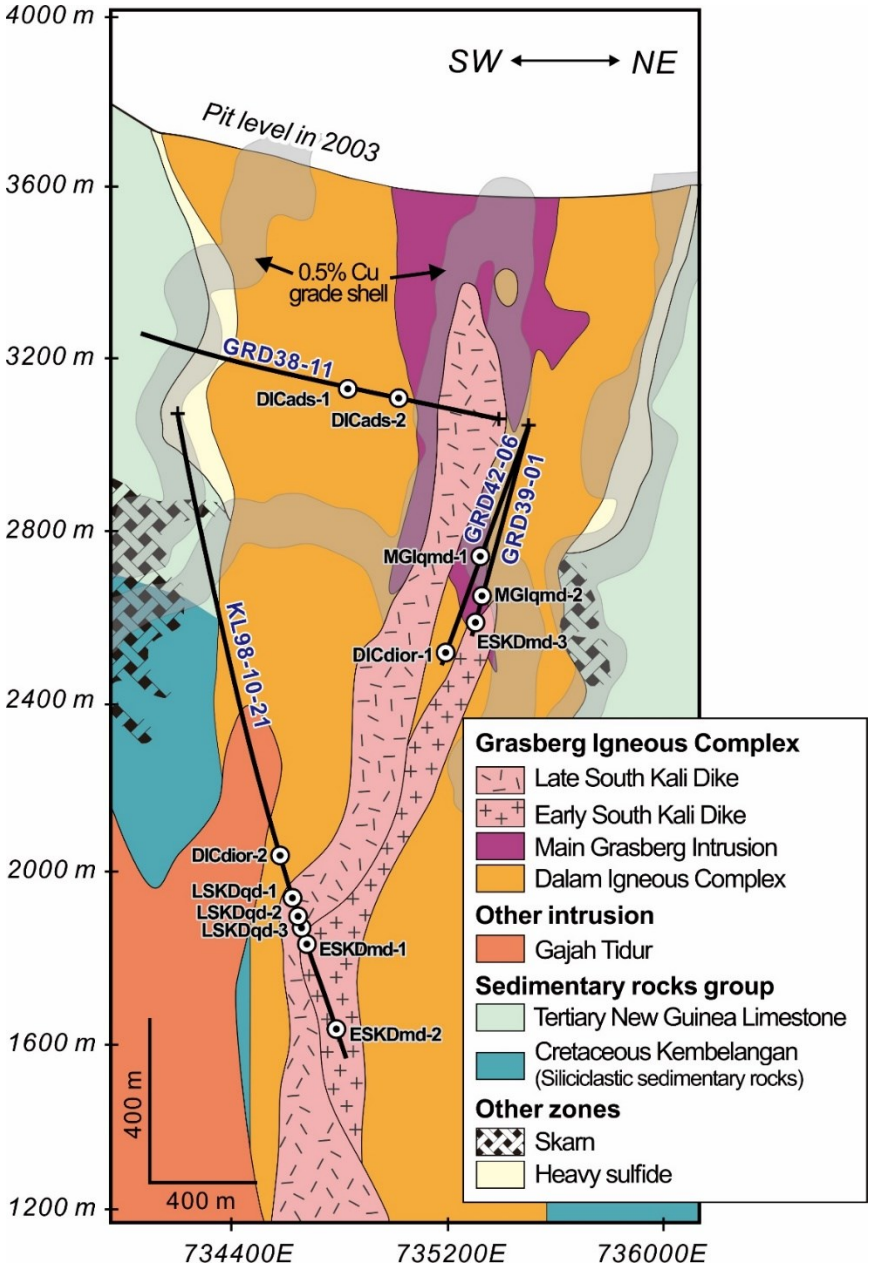

Figure 5. General SW-NE cross section of the GIC with the drill holes and samples studied for this chapter. Heavy sulfide zone contains >20% pyrite, with covellite, galena, enargite, and sphalerite.

3.2. Results

3.2.1. Igneous rock petrography

1. Pre-Mineralization DIC

Four samples from the DIC were collected, including two samples of diorite (DICdior-1, DICdior-2) which are pervasively and moderately altered and two samples of andesite (DICads-1, DICads-2), which are pervasively altered. A porphyritic texture with approximately 70% phenocrysts relics, 1–10 mm in length, of plagioclase and mafic minerals is observed in moderately altered sample collected at 2000 m elevation (DICdior-2; Fig. 6), bellow the Grasberg ore body. The groundmass consists of fine-grained hydrothermal quartz with some hydrothermal biotite, K-feldspar and sericite. Plagioclase is partly to pervasively altered to K-feldspar and sericite. Sericite tends to occur in the cores of some plagioclase crystals, whereas K-feldspar replaces the rims. Hydrothermal biotite occurs in pseudomorphs of igneous amphibole and less commonly replaces biotite phenocrysts. Amphibole pseudomorphs contain hydrothermal anhydrite in several levels. Diorite samples at 2550 m elevation (DICdior-1) is pervasively altered. Igneous amphibole is replaced by shreddy hydrothermal biotite with K-feldspar, quartz, rutile, apatite, anhydrite and minor chalcopyrite and bornite. Igneous biotite is replaced by fine-grained biotite aggregates. Plagioclase is completely altered to K-feldspar and sericite. The groundmass consists of mostly hydrothermal quartz, K-feldspar and biotite, with magnetite, anhydrite and sulfide minerals. Hydrothermal anhydrite is remarkably abundant, in which hydrothermal magnetite

is nearly absent.

Andesite samples (DICads-1, DICads-2) collected from between 3100 and 3200 m elevations are pervasively altered (Fig. 7). These rock samples are dominated by groundmass, which consists of mainly hydrothermal quartz, K-feldspar, biotite, magnetite and sulfide minerals. Phenocryst relics are less than 4 mm in size, including pseudomorphs of amphibole and plagioclase. Amphibole is replaced by shreddy hydrothermal biotite with some magnetite, K-feldspar, quartz, rutile, apatite and minor sulfide minerals. Plagioclase is completely altered to K-feldspar and/or sericite.

2. Syn-Mineralization MGI

Two weakly altered quartz monzodiorite (QMD) samples (MGIqmd-1: 2750 m elevation, MGIqmd-2: 2630 m elevation) contain amphibole, biotite and plagioclase phenocrysts up to 65 vol.%, generally from 0.5 to 4 mm in size (rarely 10 mm), in a groundmass that consists of K-feldspar, quartz and less commonly anhydrite, magnetite, ilmenite, apatite and zircon (Fig. 8). Microphenocrysts of anhydrite and titanite are also observed. Plagioclase is the most dominant mineral in this intrusion. It composes up to 55 vol.% of the rock. Anhydrite and apatite inclusions are observed in plagioclase. Amphibole phenocrysts (~5 vol.%) are texturally homogeneous (Fig. 9A) and some of them occur in contact with plagioclase and titanite-magnetite-quartz assemblage. Mineral inclusions such as magnetite, apatite, anhydrite and zircon are common. Biotite phenocrysts comprise up to 7 vol.% of the rock and are distinguished from hydrothermal biotite by their

subhedral- to euhedral-shaped crystals that vary from 0.2 to 5 mm in length and the presence of mineral inclusions of magnetite, anhydrite and zircon.

3. Syn-mineralization ESKD

Three monzodiorite (MD) samples collected from between 1600 and 2600 m elevations (ESKDmd-1, ESKDmd-2 and ESKDmd-3) show a porphyritic texture with phenocrysts of amphibole, biotite, plagioclase and K-feldspar (Fig. 10). These phenocrysts occupy approximately 80 vol.% of the rock and are up to 7 mm in size. This MD contains accessory anhydrite, titanite, magnetite, ilmenite, zircon and apatite. The only sulfides observed are very small (10 μm) chalcopyrite and pyrite inclusions in igneous magnetite. Plagioclase phenocrysts comprise up to 70 vol.% of the rock. Two types of amphibole occur in the ESKD: homogeneous and heterogeneous amphibole crystals. Heterogeneous amphibole is generally larger (up to 7 mm) than homogeneous amphibole (<5 mm). Homogeneous amphibole phenocrysts (~3 vol.%) are euhedral to anhedral and contain mineral inclusions such as magnetite, apatite, anhydrite and zircon. Heterogeneous amphiboles (3~4 vol.%) are euhedral to subhedral and characteristically show a texture of distinct core and rim (Fig. 9B). This heterogeneous amphibole is present only in the ESKD. Magnetite grains frequently occur along the core-rim boundary of the heterogeneous amphibole. The core is anhydrite- and zircon-free, whereas the rim contains inclusions of the minerals that can also be seen in the homogeneous amphibole. Titanite-magnetite-quartz assemblage and anhydrite occasionally occur in contact with the rim of heterogeneous amphibole as well as in association with

homogeneous amphibole (Fig.11). Anhydrite also occurs as inclusions within plagioclase and biotite and in the groundmass dominated by K-feldspar and quartz. Anhydrite is more abundant in the ESKD MD than in the MGI QMD. Biotite crystals (up to 3 mm in size) comprise about 3 vol.% of the rock and are characteristically subhedral to euhedral. Mineral inclusions such as magnetite, anhydrite and zircon are present in biotite. Apatite crystals are associated with both core and rim overgrowth of amphibole phenocryst, anhydrite, plagioclase and are also contained in the groundmass. Zircons are also contained in the groundmass.

4. Post-mineralization LSKD

Three quartz diorite (QD) samples collected at 1940, 1890 and 1875 m elevations are relatively equigranular in texture (less than 10 vol.% groundmass), with phenocrysts approximately 3–4 mm in crystal size (Fig. 12). This rock consists mainly of plagioclase, amphibole, biotite, K-feldspar and quartz with accessory magnetite, ilmenite, anhydrite, zircon, apatite and sulfide minerals. Plagioclase comprises up to 70 vol.% of the rock. Amphibole, which occupy about 10 vol.% of the rock, are homogeneous. Titanite-magnetite-quartz assemblage are commonly in contact with amphibole, whereas anhydrite, magnetite, apatite and zircon occur as inclusion. Biotite crystals are euhedral in shape. They compose up to 5 vol.% of rock, and include apatite, magnetite, anhydrite and zircon. Coarse-grained quartz (up to 3 mm in size) occupies up to 10 vol.% of the rock. Anhydrite and apatite also occur as inclusions within plagioclase and in the groundmass dominated by quartz.

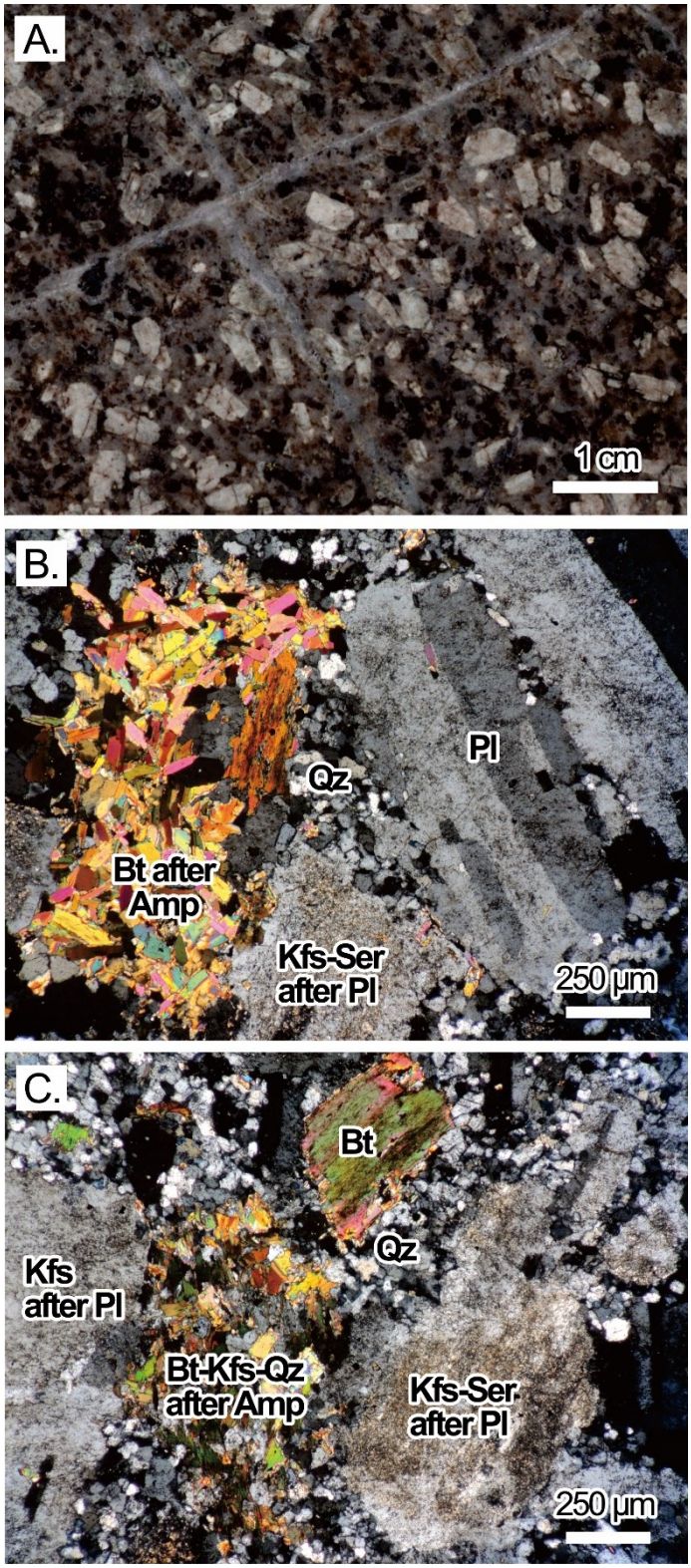

Figure 6. Polished slab (A) and cross-polarized light photomicrograph (B, C) of moderately altered pre-mineralization DIC diorite. Sample: DICdior-2

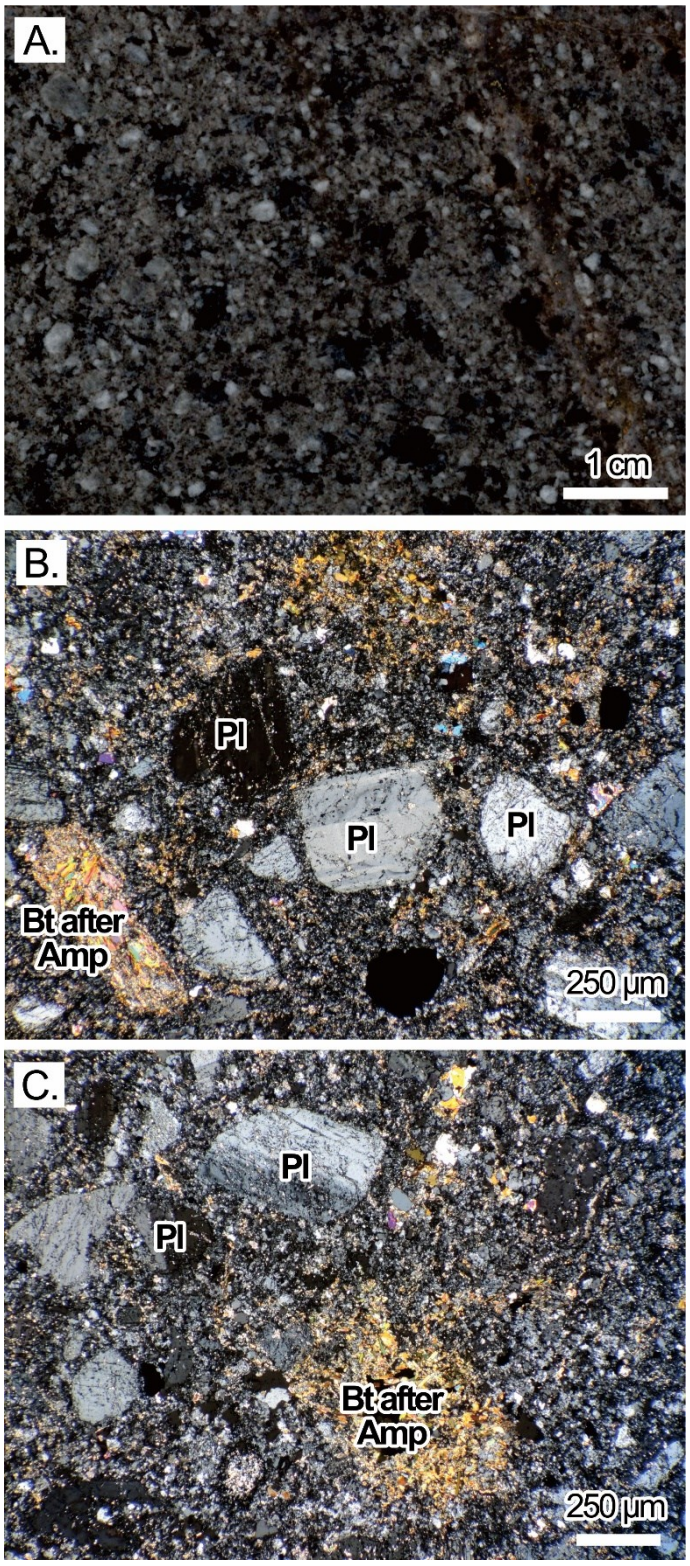

Figure 7. Polished slab (A) and cross-polarized light photomicrograph (B, C) of strongly altered pre-mineralization DIC andesite. Sample: DICads-1.

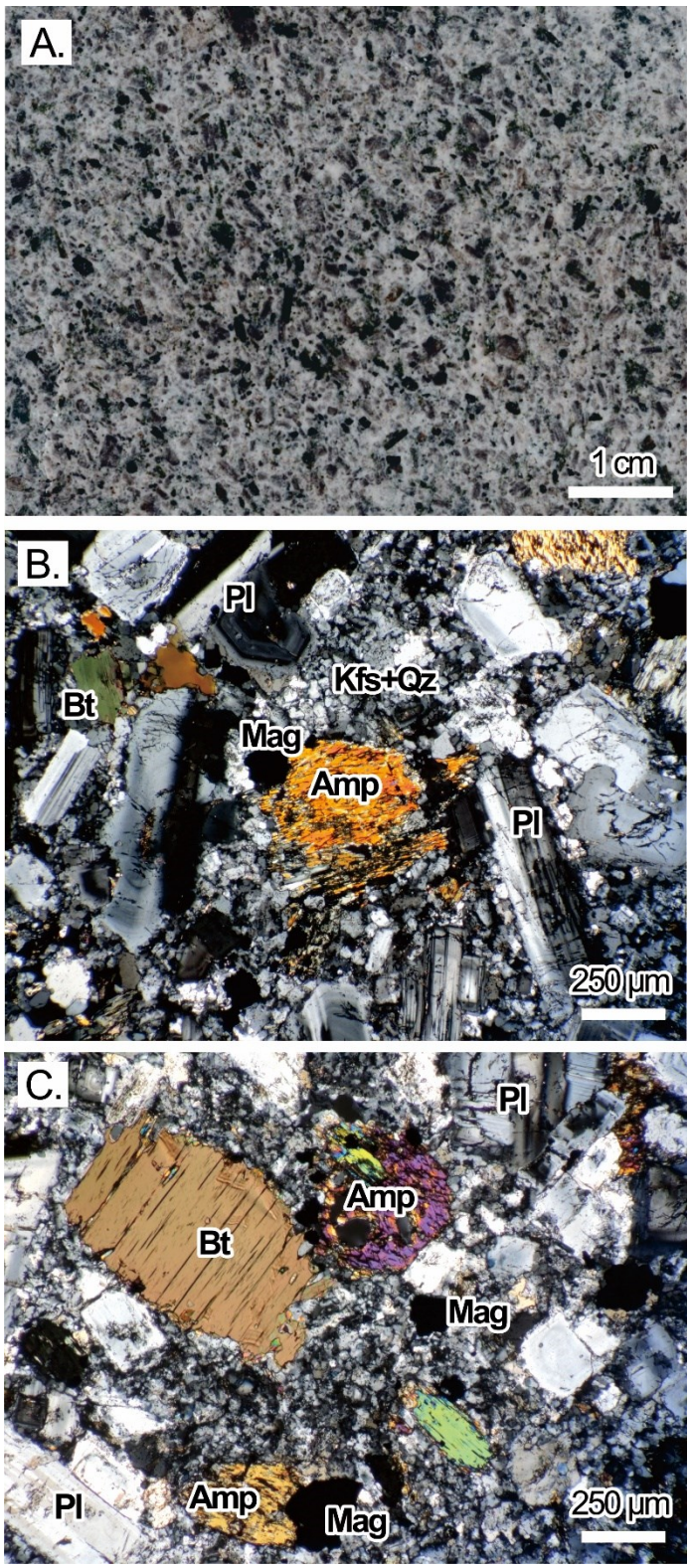

Figure 8. Polished slab (A) and cross-polarized light photomicrograph (B, C) of weakly altered syn-mineralization MGI QMD. Sample: MGIqmd-2.

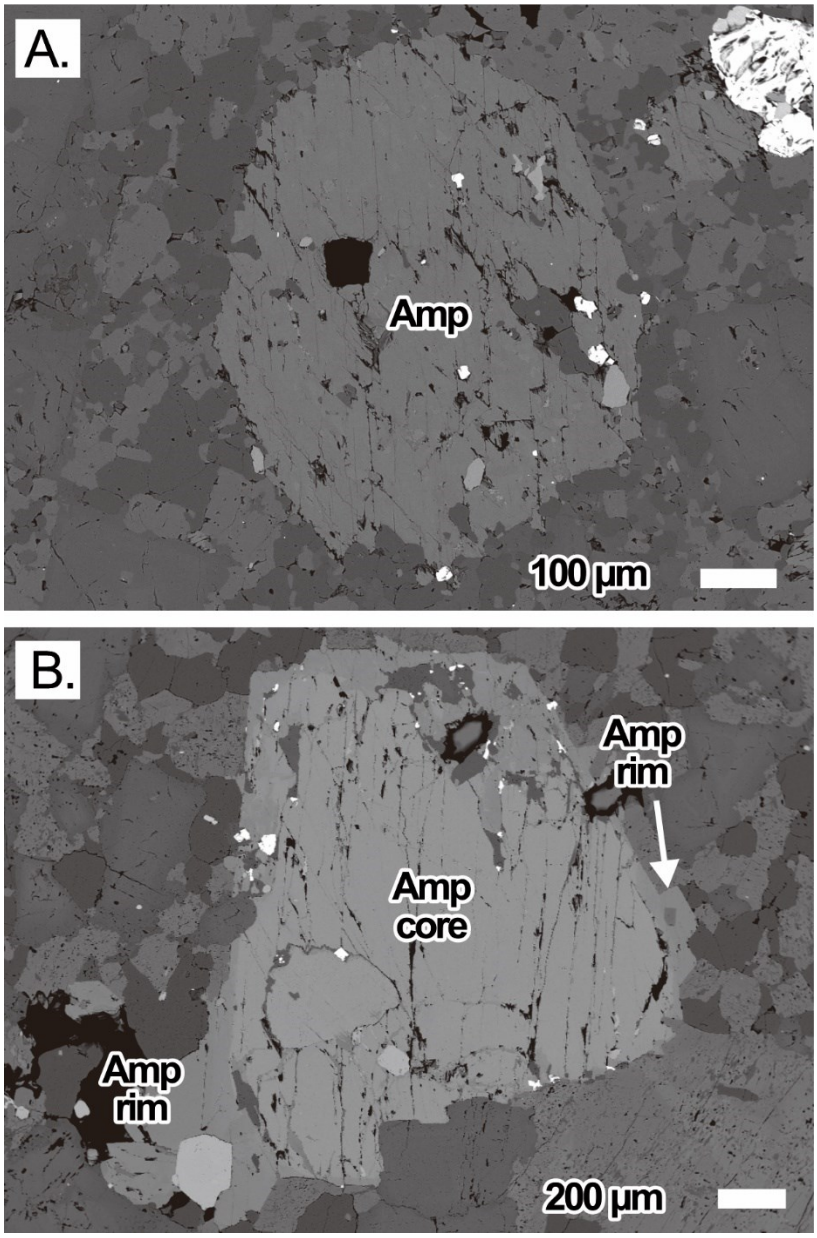

Figure 9. Backscattered electron images (BEI) of the homogeneous amphibole from the MGI QMD (A) and heterogeneous amphibole from the ESKD MD with a texture of distinct core and rim (B).

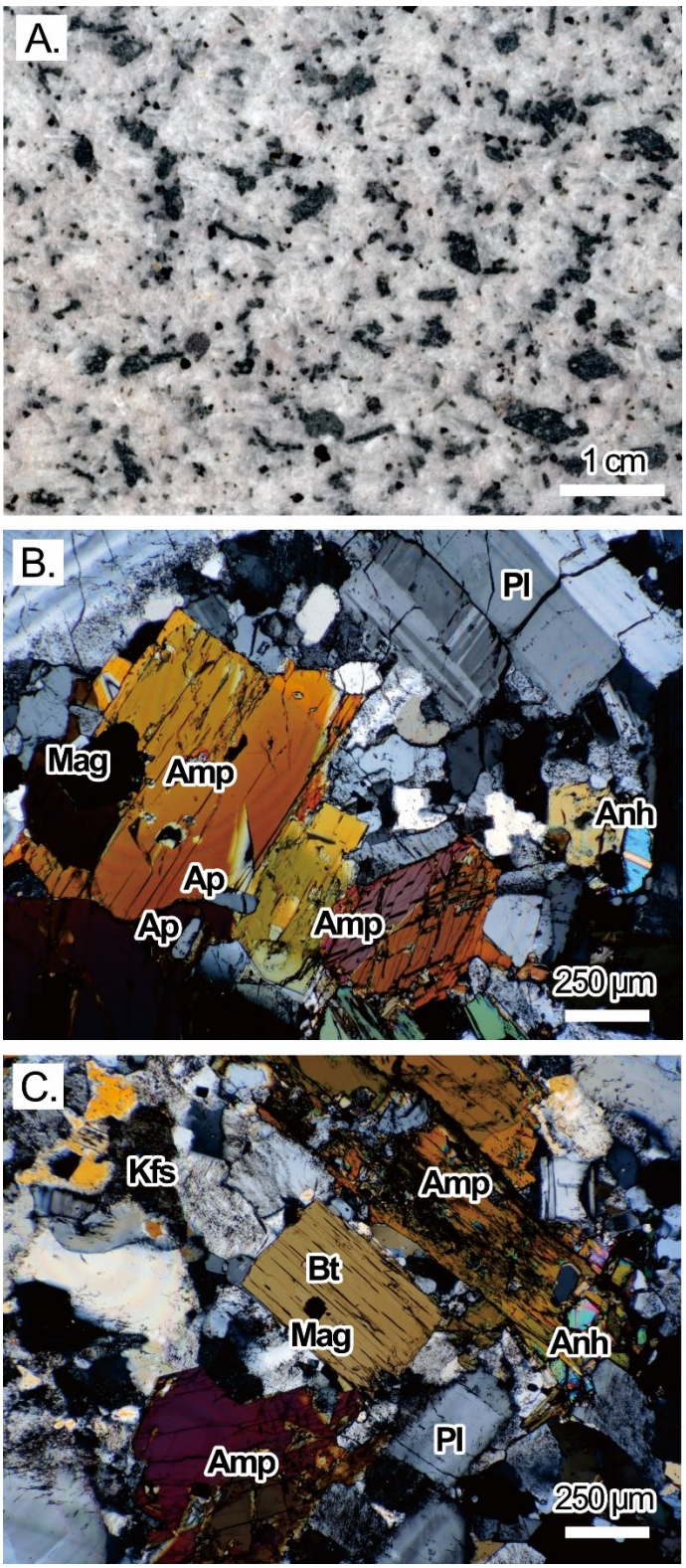

Figure 10. Polished slab (A) and cross-polarized light photomicrograph (B, C) of unaltered syn-mineralization ESKD MD. Sample: ESKDmd-1.

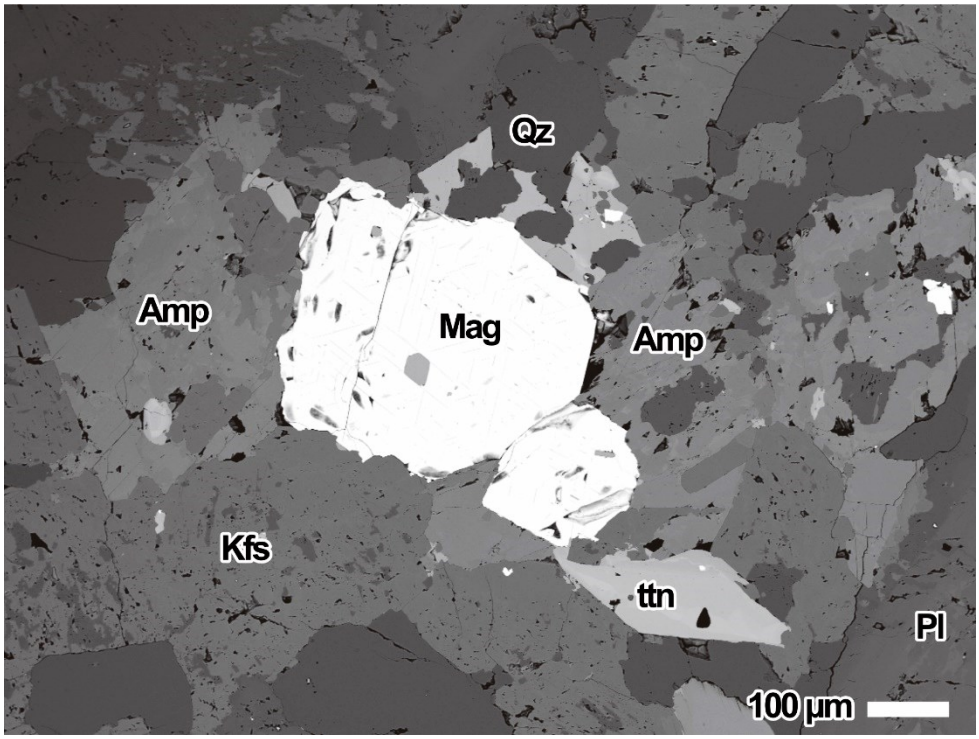

Figure 11. BEI of titanite-magnetite-quartz assemblage associated with amphibole in the ESKD MD. Sample: MGIqmd-2.

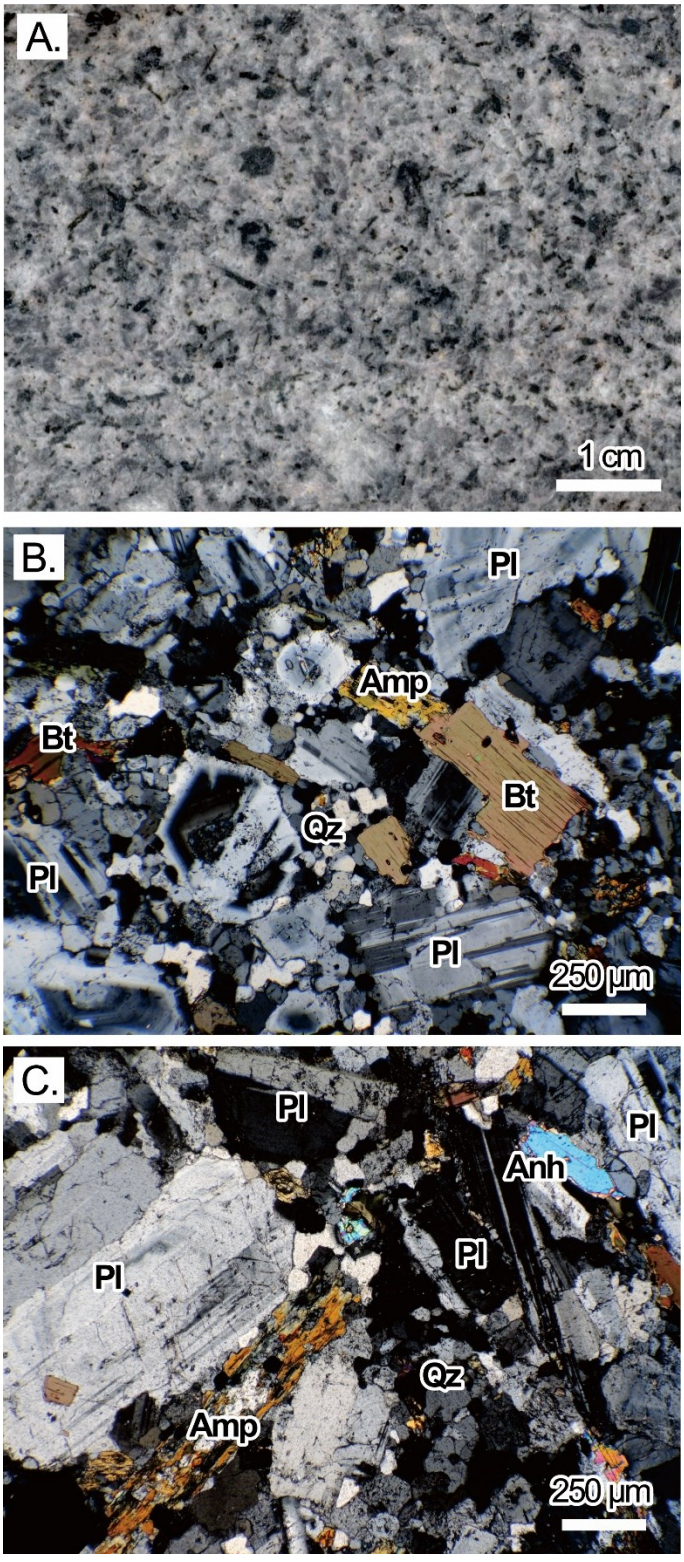

Figure 12. Polished slab (A) and cross-polarized light photomicrograph (B, C) of pre-mineralization LSKD QD. Sample: LSKDqd-2.

3.2.2. Whole-rock geochemistry

Results of bulk rock geochemical analyses are presented in Table 1. The GIC samples show intermediate to acidic SiO_2 compositional variations (55.62–67.27 wt.%) and highly variable K_2O ranging from 3.29 to 12.22 wt.%. Silica content generally increases with decreasing TiO_2 content. Moderately to pervasively altered samples from the DIC (DICdior-1, DICdior-2, DICads-1) show anomalously high K_2O contents ranging from 8.81 to 12.22 wt.%. High K_2O concentrations in these samples are due to potassic alteration of secondary K-feldspar and biotite (Fig. 6). Moderately altered DIC diorite and andesite (DICdior-1 and DICads-1) samples and one weakly altered MGI QMD (MGIqmd-1) sample show high S concentrations ranging from 0.83 to 2.62 wt.% due to hydrothermal sulfide mineralization.

Zircon saturation temperature: Zircon saturation temperatures were calculated (Table 1) using the method of Watson and Harrison (1983), assuming that the contributions of inherited zircons were negligible. Whole-rock major element compositions of unaltered samples yield calculated zircon saturation temperatures of 720 °C and 710 °C for the ESKD and LSKD magmas, respectively. One weakly altered MGI QMD sample records a slightly higher temperature at 750 °C. The moderately to pervasively altered DIC diorite and andesite samples yield variable temperatures ranging from 700 to 800 °C. This variation is interpreted due to hydrothermal alteration which affects the compositional factor that accounts for dependence of zircon solubility on SiO_2 and peraluminosity of the melt ("M" factor; Watson and Harrison, 1983). Thus, I discard the zircon saturation temperature

estimates from these moderately to pervasively altered rocks.

Whole-rock rare earth element (REE): The observed GIC rocks have REE^{tot} ranging from 45 to 165 ppm. The Eu anomaly (Eu/Eu*) values were calculated using a conventional method, where Eu/Eu* is defined as $Eu_N/(Sm_N \times Gd_N)^{0.5}$ ("$_N$" indicates chondrite-normalized value of McDonough and Sun, 1995). The calculated Eu/Eu* values indicate scarce negative Eu anomaly, ranging from 0.71 to 1.02 (Table 1).

Table 1. Whole-rock major and trace element concentrations for the GIC rocks. Pre-min.: pre-mineralization.

Sample	DICdior-1	DICdior-2	DICads-1	MGIqmd-1	ESKImd-1	LSKlqd-3
Rock type	Diorite	Diorite	Andesite	QMD	MD	QD
Timing	Pre-min.	Pre-min.	Pre-min.	Syn-min.	Syn-min.	Post-min.
SiO_2 (wt.%)	61.37	67.27	55.62	63.23	62.55	62.75
Al_2O_3	15.84	14.86	24.05	17.05	16.83	16.56
FeO	4.53	3.51	2.62	6.22	5.88	5.83
MnO	0.03	0.03	0.02	0.03	0.10	0.10
MgO	2.15	1.50	2.60	1.37	1.42	1.64
CaO	3.88	1.45	0.54	3.87	5.12	5.36
Na_2O	1.55	1.96	1.09	3.30	3.99	3.79
K_2O	9.83	8.81	12.22	4.28	3.42	3.29
TiO_2	0.51	0.40	0.78	0.45	0.43	0.44
P_2O_5	0.32	0.20	0.46	0.21	0.25	0.24
H_2O	2.34	0.64	1.31	0.42	0.68	0.33
C	0.09	0.06	0.03	0.03	0.05	0.02
S	2.34	0.33	0.83	2.62	0.24	0.20
Ti (ppm)	2836	2338	4460	2602	2578	2608
Zr	115	118	174	137	122	116
La	20.86	9.37	37.41	33.65	32.03	27.77
Ce	41.03	17.40	70.12	65.11	61.33	52.65
Pr	4.91	2.06	7.94	7.51	6.97	5.97
Nd	19.46	8.33	30.92	28.05	25.83	22.52
Sm	3.91	1.78	5.73	5.01	4.77	4.22
Eu	0.91	0.61	1.47	1.43	1.44	1.23
Gd	3.87	1.90	5.15	4.47	4.57	4.06
Tb	0.50	0.26	0.57	0.53	0.60	0.54
Dy	2.58	1.39	2.79	2.59	3.35	2.97
Ho	0.50	0.29	0.50	0.47	0.67	0.59
Er	1.43	0.79	1.38	1.29	1.98	1.78
Tm	0.19	0.12	0.18	0.17	0.28	0.24
Yb	1.16	0.65	1.00	1.01	1.79	1.62
Lu	0.17	0.11	0.15	0.15	0.27	0.25
Hf	0.16	0.16	0.38	0.17	0.65	0.38
Th	4.71	11.25	10.71	4.43	6.89	5.34
U	0.68	0.98	0.28	0.62	1.56	1.13
Y	13.78	8.05	13.53	12.61	18.56	16.44
Nb	3.86	3.11	4.37	2.94	8.77	7.89
$Na_2O+ K_2O$	11.38	10.77	13.31	7.58	7.41	7.07
M	2.24	1.65	1.31	1.70	2.00	2.02
Zrn sat. T	703 °C	743 °C	800 °C	752 °C	722 °C	717 °C
Eu/Eu*	0.71	1.02	0.82	0.92	0.94	0.90

3.2.3. Amphibole composition

Representative analytical results of both homogeneous and heterogeneous amphiboles of MGI QMD, ESKD MD and LSKD QD are shown in Table 2. Homogeneous amphiboles of these rocks (Fig. 9A) are principally low-Al (Al^{tot} of 0.35–1.04 atoms per formula unit [apfu]), calcic (Ca_A >1.50 apfu), alkali-poor [$(Na+K)_A$ <0.50 apfu; Fig. 13A] magnesiohornblende and rare actinolite with Si and Mg# [$Mg/(Mg+Fe^{2+})$] values of 7.04–7.66 apfu and 0.75–0.87 (Fig. 13B), respectively (hereafter referred to as "low-Al amphibole"). Heterogeneous amphiboles show a chemically distinct core and rim (Fig. 9B). The cores of amphiboles are high in Al (Al^{tot} of 1.53–1.80 apfu), calcic and alkali-rich [$(Na+K)_A$ ≥0.50 apfu; Fig. 13A] (hereafter referred to as "high-Al amphibole"). They are principally magnesiohastingsite ($Al^{VI} < Fe^{3+}$) with Si and Mg# values of 6.41–6.66 apfu and 0.59–0.65 (Fig. 13B), respectively. In contrast, the rims are calcic, alkali-poor (Fig. 13A), low-Al amphibole (Al^{tot} of 0.93–1.03 apfu). These rims are principally magnesiohornblende with Si and Mg# values of 7.05–7.14 apfu and 0.75–0.76 (Fig. 13B), respectively.

The analysis of volatile contents (F, Cl) shows that high-Al and low-Al amphiboles are distinct and characterized by high Cl and low Cl, respectively. Chlorine concentrations in high-Al amphiboles range from 0.18 to 0.26 wt.%, whereas low-Al amphiboles contain lower Cl concentrations of 0.04–0.13 wt.%. Flourine is only detected in some amphiboles (0.01 wt.%) from the ESKD MD and LSKD QD.

The high-Al amphiboles of the ESKD MD show higher REE^{tot}, Y, Cu, Li, V,

Sr, Nb, Ba and Pb contents than the low-Al amphiboles from all samples (Table 2). All high-Al amphiboles of the ESKD MD have a narrow range of REE_N (Fig. 14A). They show REE_N patterns of convex upward with maxima of approximately 130–220 and 120–210 times chondrite at Pr and Nd, respectively and widely variable negative Eu anomaly ranging from 0.47 to 0.87 (avg. 0.65). The low-Al rims have a wider range of REE_N values than the high-Al core and show a convex downward pattern with negative Eu anomaly, similar to the associated homogeneous low-Al amphibole. These low-Al rims and homogeneous low-Al amphibole yield the Eu/Eu* values of 0.44–0.67 (avg. 0.55) and 0.38–0.51 (avg. 0.46), respectively. The low-Al amphiboles of the MGI QMD have a wide range of REE_N and show both convex upward and downward pattern with Eu/Eu* values of 0.42–0.62 (avg. 0.50), whereas the low-Al amphiboles of the LSKD QD yield a narrow range of REE_N and exhibit a convex downward pattern with smaller negative Eu/Eu* (0.62–0.74, avg. 0.69). Low-Al amphiboles of both MGI QMD and LSKD QD show lower La_N values than both high- and low-Al amphiboles of the ESKD MD. Trace element compositions of high-Al and low-Al amphiboles also differ on primitive mantle-normalized diagrams, where the low-Al amphiboles have large negative anomalies in large-ion lithophile elements such as Ba and Sr and low MREE and Y compared with the high-Al amphiboles (Fig. 14B).

Crystallization temperatures and magma oxidation states were calculated using the equations of Ridolfi et al. (2010), whereas crystallization pressures were computed using Al-in-amphibole geobarometer of Mutch et al. (2016) (Table 2). These estimates are not applicable for pre-mineralization intrusions at Grasberg

because amphiboles are hydrothermally altered. The barometer equation of Ridolfi et al. (2010) yields unrealistically lower pressures and correspondingly shallower crustal depths up less than 1 km.

Table 2. Summary statistics of amphibole geochemistry analyzed using electron microprobe and LA-ICP-MS. Formula on the basis of 13 cations (Leake et al., 1997). See Ridolfi et al. (2010) for temperature and fO_2 estimates and Mutch et al. (2016) for pressure estimates.

Sample	MGIqmd-2 (MGI			ESKDmd-1 (ESKD MD)					
Type	Homogeneous low-Al			Heterogeneous					
				High-Al core			Low-Al rim		
n		95			49			24	
Statistic	Min	Mean	Max	Min	Mean	Max	Min	Mean	Max
SiO_2 (wt.%)	51.78	52.70	53.58	42.7	43.59	44.99	48.7	49.02	49.47
TiO_2	0.29	0.44	0.55	1.64	1.83	2.00	0.98	1.14	1.25
Al_2O_3	2.06	3.15	3.63	8.75	9.78	10.22	5.48	5.83	6.04
FeO	9.21	10.17	10.98	15.2	16.10	16.78	12.2	12.55	12.74
MnO	0.47	0.56	0.65	0.54	0.58	0.63	0.68	0.75	0.84
MgO	16.72	17.35	18.14	10.6	11.28	12.06	14.6	14.85	14.99
CaO	11.96	12.13	12.53	11.4	11.56	11.66	11.7	11.82	11.94
Na_2O	0.53	0.73	0.82	1.56	1.73	1.84	1.17	1.28	1.36
K_2O	0.16	0.26	0.32	1.12	1.32	1.47	0.57	0.59	0.60
F	0.00	0.00	0.01	0.00	0.00	0.00	0.00	0.00	0.00
Cl	0.04	0.06	0.08	0.18	0.23	0.26	0.09	0.10	0.11
Total	96.92	97.54	98.16	97.7	98.00	98.32	97.8	97.91	97.97
Si (apfu)	7.38	7.48	7.66	6.41	6.49	6.66	7.05	7.08	7.14
Al^{IV}	0.34	0.51	0.61	1.34	1.51	1.59	0.86	0.92	0.95
Al^{VI}	0.00	0.01	0.04	0.19	0.21	0.24	0.06	0.07	0.08
Ti	0.03	0.05	0.06	0.18	0.21	0.23	0.11	0.12	0.14
Fe^{3+}	0.34	0.48	0.61	0.41	0.44	0.49	0.45	0.48	0.50
Fe^{2+}	0.56	0.73	0.84	1.45	1.56	1.67	1.00	1.04	1.06
Mn	0.06	0.07	0.08	0.07	0.07	0.08	0.08	0.09	0.10
Mg	3.56	3.67	3.87	2.38	2.51	2.66	3.16	3.20	3.22
Ca	1.81	1.85	1.92	1.82	1.85	1.86	1.82	1.83	1.85
Na	0.15	0.20	0.23	0.45	0.50	0.53	0.33	0.36	0.38
K	0.03	0.05	0.06	0.21	0.25	0.28	0.10	0.11	0.11
F	0.00	0.00	0.00	0.00	0.00	0.00	0.00	0.00	0.00
Cl	0.01	0.02	0.02	0.05	0.06	0.06	0.02	0.02	0.03
OH^{calc}	1.98	1.98	1.99	1.94	1.94	1.95	1.97	1.98	1.98
Al^{tot}	0.35	0.53	0.61	1.53	1.72	1.80	0.93	0.99	1.03
(Na+K)A	0.03	0.10	0.18	0.50	0.60	0.64	0.28	0.30	0.31
NaB	0.00	0.15	0.18	0.14	0.15	0.18	0.15	0.17	0.18
Mg#	0.81	0.83	0.87	0.59	0.62	0.65	0.75	0.75	0.76
Molar Si/Al^{tot}	12.12	14.49	22.08	3.55	3.79	4.36	6.86	7.15	7.65
n		5			10			10	
Li (ppm)	0.67	1.34	2.18	2.88	7.53	20.65	2.08	2.87	3.50
V	142	186	219	280	353	392	158	191	241
Co	33.05	40.91	47.21	38.7	41.84	45.26	36.8	39.24	42.42

Sample	MGIqmd-2 (MGI			ESKDmd-1 (ESKD MD)					
Type	Homogeneous low-Al			Heterogeneous					
				High-Al core			Low-Al rim		
n	95			49			24		
Statistic	Min	Mean	Max	Min	Mean	Max	Min	Mean	Max
Ni	12.24	13.80	17.62	4.50	14.23	19.45	15.4	17.08	18.84
Cu	0.41	0.58	0.90	0.78	1.12	1.45	0.40	0.83	1.57
Zn	125	136	151	222	256	281	216	225	235
Rb	0.68	1.33	1.70	2.81	4.55	5.54	1.74	3.91	6.60
Sr	10.01	10.55	11.09	40.1	114.6	147.6	2.65	6.68	15.90
Y	9.85	22.18	42.72	47.5	86.46	111.9	6.96	23.23	60.60
Zr	12.22	21.03	33.63	30.9	45.82	59.10	24.0	31.79	41.16
Nb	1.45	4.77	13.29	14.7	22.00	27.16	1.74	9.43	19.50
Ba	0.41	0.83	1.07	14.0	93.30	163.6	0.63	2.79	6.90
La	5.71	7.04	9.50	22.9	25.72	32.79	10.4	29.85	55.25
Ce	10.84	19.86	26.74	82.6	99.93	124.7	15.6	55.76	120.16
Pr	1.34	2.81	4.04	12.4	16.64	20.52	1.54	5.84	14.41
Nd	5.61	12.88	20.90	54.7	79.27	95.56	5.80	20.35	50.71
Sm	1.46	3.81	7.33	12.2	20.62	26.66	1.21	3.62	9.04
Eu	0.29	0.57	1.06	2.71	4.09	5.45	0.24	0.60	1.35
Gd	1.34	3.63	7.33	9.71	18.89	25.21	1.26	3.36	8.30
Tb	0.23	0.60	1.19	1.45	2.82	3.85	0.18	0.51	1.25
Dy	1.51	3.76	7.52	9.01	17.82	24.46	1.11	3.36	8.74
Ho	0.35	0.78	1.50	1.76	3.47	4.61	0.24	0.76	2.00
Er	1.13	2.39	4.40	5.08	9.87	13.06	0.79	2.60	6.59
Tm	0.19	0.36	0.62	0.77	1.37	1.78	0.14	0.44	1.07
Yb	1.54	2.63	4.34	5.63	8.97	11.27	1.36	3.84	7.54
Lu	0.26	0.44	0.68	0.78	1.21	1.58	0.30	0.73	1.22
Hf	0.79	1.32	2.04	2.13	2.53	2.98	1.46	2.51	3.65
Pb	0.25	0.46	0.72	1.02	2.03	4.69	0.40	0.91	2.65
Th	0.04	0.19	0.42	0.13	0.17	0.26	0.14	0.20	0.27
U	0.03	0.20	0.73	0.02	0.04	0.09	0.02	0.09	0.19
Calculated P, T and fO_2									
T (°C)	700	714	729	854	884	897	771	781	785
ΔFMQ	3.2	3.4	3.7	0.8	1.0	1.4	2.3	2.4	2.5
P (kbar)	0.7	1.0	1.1	3.3	4.0	4.3	1.7	1.8	1.9

Table 2. Continued

Sample	ESKDmd-1 (ESKD MD)						LSKDqd-2		
Type	Homogeneous low-Al			All low-Al Amphibole (rim + homogeneous)			Homogeneous low-Al		
n		37			61			93	
Statistic	Min	Mean	Max	Min	Mean	Max	Min	Mean	Max
SiO_2 (wt.%)	48.63	50.35	52.41	48.63	49.91	52.41	51.04	52.46	53.37
TiO_2	0.43	0.93	1.41	0.43	1.00	1.41	0.49	0.62	0.81
Al_2O_3	3.47	4.84	6.11	3.47	5.17	6.11	2.87	3.62	4.91
FeO	10.70	11.51	12.93	10.70	11.86	12.93	9.75	10.26	11.05
MnO	0.79	0.89	1.04	0.68	0.84	1.04	0.45	0.49	0.56
MgO	14.51	15.83	16.62	14.51	15.50	16.62	16.32	17.14	17.73
CaO	11.61	11.78	12.16	11.61	11.79	12.16	11.92	12.04	12.11
Na_2O	0.81	1.17	1.38	0.81	1.21	1.38	0.71	0.86	1.08
K_2O	0.27	0.46	0.60	0.27	0.50	0.60	0.26	0.32	0.44
F	0.00	0.00	0.02	0.00	0.00	0.02	0.00	0.01	0.03
Cl	0.06	0.08	0.13	0.06	0.09	0.13	0.06	0.07	0.08
Total	97.71	97.84	98.08	97.71	97.87	98.08	97.42	97.88	98.11
Si (apfu)	7.04	7.21	7.46	7.04	7.17	7.46	7.26	7.43	7.54
Al^{IV}	0.54	0.79	0.96	0.54	0.83	0.96	0.46	0.57	0.74
Al^{VI}	0.00	0.03	0.08	0.00	0.05	0.08	0.00	0.04	0.10
Ti	0.05	0.10	0.15	0.05	0.11	0.15	0.05	0.07	0.09
Fe^{3+}	0.41	0.53	0.61	0.41	0.51	0.61	0.38	0.45	0.49
Fe^{2+}	0.68	0.85	1.05	0.68	0.91	1.06	0.67	0.77	0.90
Mn	0.10	0.11	0.13	0.08	0.10	0.13	0.05	0.06	0.07
Mg	3.13	3.38	3.53	3.13	3.32	3.53	3.46	3.62	3.73
Ca	1.77	1.81	1.86	1.77	1.82	1.86	1.82	1.83	1.84
Na	0.22	0.32	0.38	0.22	0.34	0.38	0.20	0.24	0.30
K	0.05	0.08	0.11	0.05	0.09	0.11	0.05	0.06	0.08
F	0.00	0.00	0.01	0.00	0.00	0.01	0.00	0.00	0.01
Cl	0.01	0.02	0.03	0.01	0.02	0.03	0.01	0.02	0.02
OH^{calc}	1.97	1.98	1.99	1.97	1.98	1.99	1.97	1.98	1.99
Al^{tot}	0.58	0.82	1.04	0.58	0.88	1.04	0.48	0.61	0.82
(Na+K)A	0.13	0.22	0.30	0.13	0.24	0.31	0.07	0.12	0.20
NaB	0.14	0.19	0.23	0.14	0.18	0.23	0.16	0.17	0.18
Mg#	0.75	0.80	0.84	0.75	0.78	0.84	0.79	0.83	0.85
Molar Si/Al^{tot}	6.76	9.13	12.81	6.76	8.47	12.81	8.81	12.59	15.71
n		3			13			4	
Li (ppm)	2.19	2.72	3.14	2.08	2.83	3.50	1.58	1.93	2.18
V	175	181	187	158	189	241	139	150	159
Co	39.42	40.39	41.07	36.89	39.50	42.42	42.71	43.21	43.91

Sample	ESKDmd-1 (ESKD MD)						LSKDqd-2		
Type	Homogeneous low-Al			All low-Al Amphibole (rim + homogeneous)			Homogeneous low-Al		
n	37			61			93		
Statistic	Min	Mean	Max	Min	Mean	Max	Min	Mean	Max
Ni	15.29	17.51	18.75	15.29	17.18	18.84	24.71	26.39	28.06
Cu	0.65	0.83	1.02	0.40	0.83	1.57	0.41	0.61	0.99
Zn	224	229	233	216	226	235	142	147	152
Rb	3.84	4.44	5.53	1.74	4.03	6.60	1.26	1.60	2.04
Sr	3.02	4.62	5.99	2.65	6.20	15.90	6.96	7.90	8.56
Y	19.52	27.08	31.91	6.96	24.12	60.60	7.16	8.02	8.62
Zr	32.55	37.51	45.41	24.08	33.11	45.41	9.64	11.72	15.58
Nb	13.30	17.49	23.78	1.74	11.29	23.78	0.96	1.23	1.35
Ba	0.48	1.50	2.39	0.48	2.49	6.90	0.43	1.08	1.45
La	47.25	53.98	65.22	10.42	35.42	65.22	4.11	4.52	5.39
Ce	52.58	86.12	120.69	15.60	62.76	120.69	8.93	9.98	11.34
Pr	3.63	7.14	9.55	1.54	6.14	14.41	1.05	1.20	1.31
Nd	13.17	22.11	26.85	5.80	20.76	50.71	4.36	4.85	5.33
Sm	3.12	3.95	4.70	1.21	3.69	9.04	0.94	1.15	1.30
Eu	0.48	0.57	0.71	0.24	0.60	1.35	0.23	0.26	0.29
Gd	3.13	3.64	4.15	1.26	3.43	8.30	1.04	1.18	1.24
Tb	0.47	0.55	0.62	0.18	0.52	1.25	0.15	0.18	0.21
Dy	3.39	3.87	4.24	1.11	3.48	8.74	1.02	1.18	1.30
Ho	0.65	0.83	0.98	0.24	0.77	2.00	0.23	0.27	0.29
Er	2.20	2.95	3.51	0.79	2.68	6.59	0.77	0.89	1.03
Tm	0.32	0.50	0.62	0.14	0.46	1.07	0.13	0.16	0.18
Yb	2.60	4.45	5.52	1.36	3.98	7.54	1.02	1.26	1.45
Lu	0.46	0.77	0.99	0.30	0.74	1.22	0.20	0.24	0.27
Hf	2.61	3.30	4.25	1.46	2.70	4.25	0.57	0.78	1.13
Pb	0.57	0.98	1.52	0.40	0.93	2.65	0.15	0.34	0.87
Th	0.17	0.20	0.22	0.14	0.20	0.27	0.05	0.06	0.07
U	0.05	0.10	0.13	0.02	0.09	0.19	0.02	0.03	0.05
Calculated P, T and fO_2									
T (°C)	716	757	786	716	765	786	702	721	752
ΔFMQ	2.3	2.8	3.2	2.3	2.7	3.2	2.9	3.3	3.5
P (kbar)	1.0	1.5	1.9	1.0	1.6	1.9	0.9	1.1	1.4

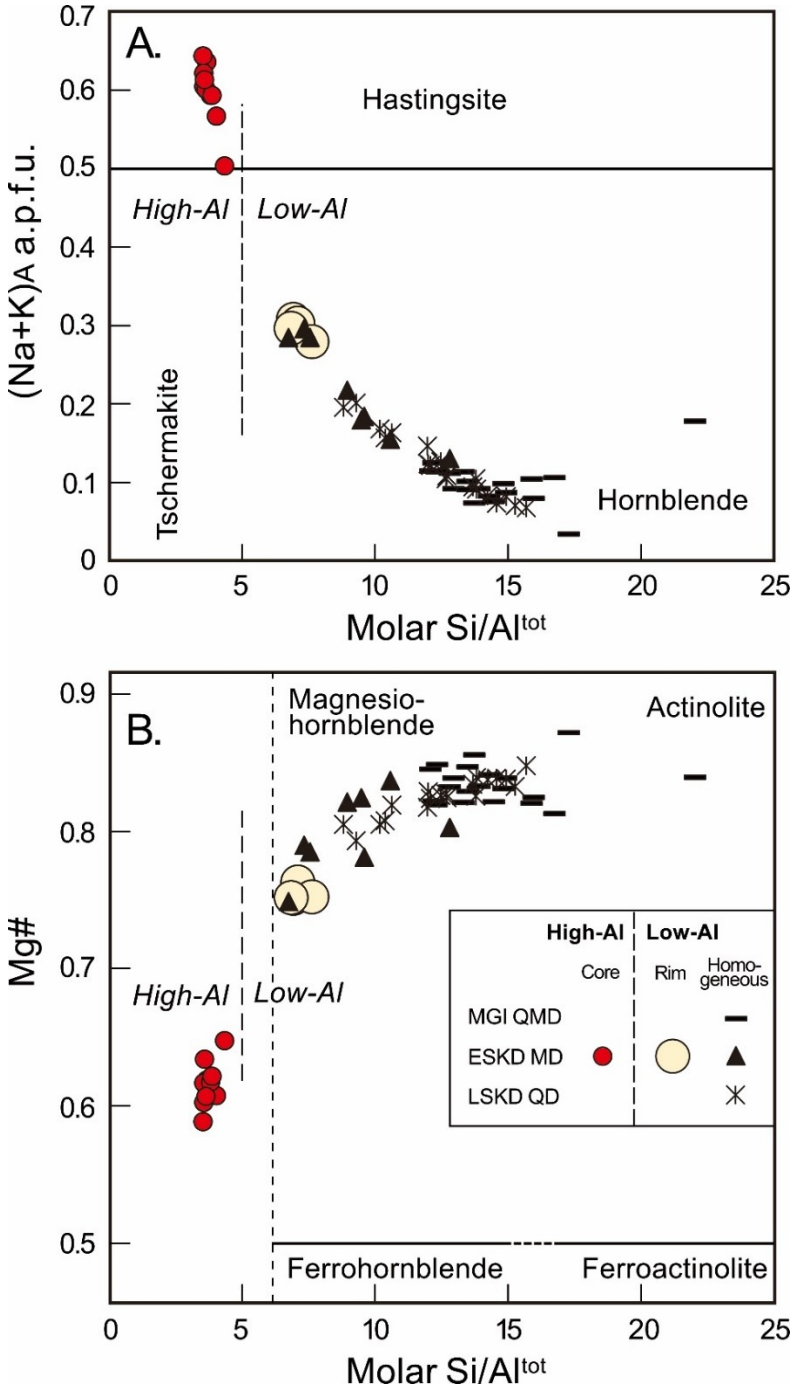

Figure 13. Compositional variations of amphibole in the GIC. (A) Molar Si/Al^{tot} vs. $(Na+K)_A$ (B) Molar Si/Altot vs. Mg# (molar $Mg/[Mg+Fe^{2+}]$).

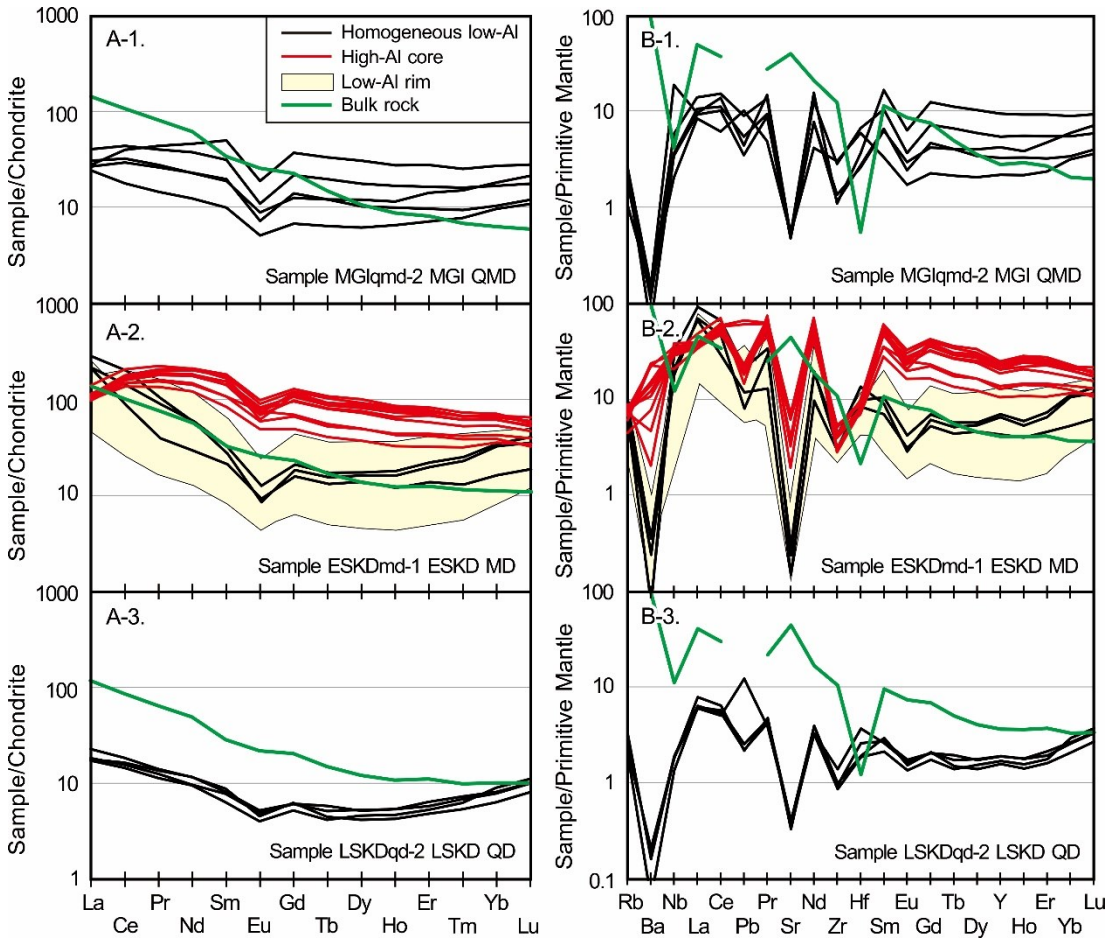

Figure 14. (A) Chondrite-normalized REE patterns for amphibole and whole-rocks from the (A-1) MGI QMD, (A-2) ESKD MD and A-3) LSKD QD. Chondrite normalization values from McDonough and Sun (1995). (B) Trace element patterns for whole-rock and both high-Al and low-Al amphibole normalized to primitive mantle. Primitive mantle composition from Sun and McDonough (1989).

3.2.4. Trace element geochemistry of zircons

All zircons separated from the GIC are euhedral to subhedral, generally 75 to 200 μm in length, rarely up to 300 μm (length to width ratios ranging from approximately 1 to 10). Zircon grains are reddish brown to pinkish. Inherited cores, fractures and melt and mineral inclusions are common. Inherited cores are differentiated from their overgrown rims by irregular or dissolution boundaries, which truncate internal zoning or separate unzoned or irregularly zoned cores from overgrown zoned rims. Although most zircon grains have a combination between oscillatory and sector zoning, zircons with no or minor sector zoning were selected for LA-ICP-MS analysis (Fig. 15).

Apatite inclusions are common and were avoided for LA-ICP-MS analysis because they can cause unrealistically high light REE (LREE) concentrations, but nonetheless I monitored measured Ca and P concentrations. Representative trace element compositions of zircon from the GIC are presented in Table 3. Zircons from the GIC (*n*=137) yield Th/U ranging from 0.22 to 1.42, confirming their magmatic origin (see Hoskin and Ireland, 2000; Hoskin and Schaltegger, 2003). The REE^{tot} (234–1995 ppm) and Yb_N/Gd_N (19.58–71.17) values are also comparable to typical calc-alkaline granitic rocks of 1–15645 ppm and 0.9–85.9, respectively (Table 3). The Ti-in-zircon geothermometer of Ferry and Watson (2007) provides estimates of 800–630 °C for zircon crystallizations (also see Table 1 for zircon saturation temperature). I use the activity (α) of TiO_2 = 0.7 (e.g., Claiborne et al., 2006; Dilles et al., 2015; Lee et al., 2017) to reflect titanite saturation and αSiO_2 = 1 to represent quartz saturation. Variation of αTiO_2 by ±0.1 introduces an error ±10 to 17 °C.

Chondrite-normalized REE diagrams for GIC zircons show a systematic heavy REE (HREE)-enriched pattern with large positive Ce and small negative Eu anomalies (Fig. 16). In this study, Ce and Eu anomalies are expressed as Ce^{4+}/Ce^{3+}, Ce/Nd, Ce/Ce* and Eu/Eu* (Table 3). The Ce^{4+}/Ce^{3+} ratios were calculated following the method of Ballard et al. (2002), which requires concentrations of Ce both in zircon and melt (assuming whole-rock composition as melt) and zircon-melt partition coefficients for Ce^{4+} and Ce^{3+}. These coefficients can be estimated on the basis of a lattice-strain model for mineral-melt partition of elements (Blundy and Wood, 1994). Calculating Ce/Ce* by $Ce_N/(La_N \times Pr_N)^{0.5}$ is not possible because zircon contains very low amounts of La and Pr (10s–100s of ppb, Hoskin and Schalteggar, 2003). These values are frequently bellow the detection limit of LA-ICP-MS method used in this study. Thus, I use Ce/Nd (e.g., Chelle-Michou et al., 2014) and Ce/Ce* calculated on the basis of Nd and Sm, where Ce* is defined as $(Nd_N)^2/Sm_N$ (Loader et al., 2017). The Eu/Eu* values were calculated using a conventional method, the same as that used for bulk rocks.

The oxygen fugacity (fO_2) estimates (Table 3) were computed using the equation of Trail et al. (2012). This equation is based on Ce anomaly in zircon calculated from partition coefficients. Calculation of Eu anomaly provides unrealistically high values compared with the use of Ce. I was unable to calculate magma fO_2 from zircon-melt partitioning of Ce because of unreasonably low H_2O concentrations recorded in the GIC samples (Table 1). This low H_2O content is inconsistent with the abundance of amphibole in the GIC. The abundant occurrence of amphibole suggests a H_2O concentration of at least 2 to 4 wt.% at confining

pressures in excess of 1 to 2 kbar (Naney, 1983).

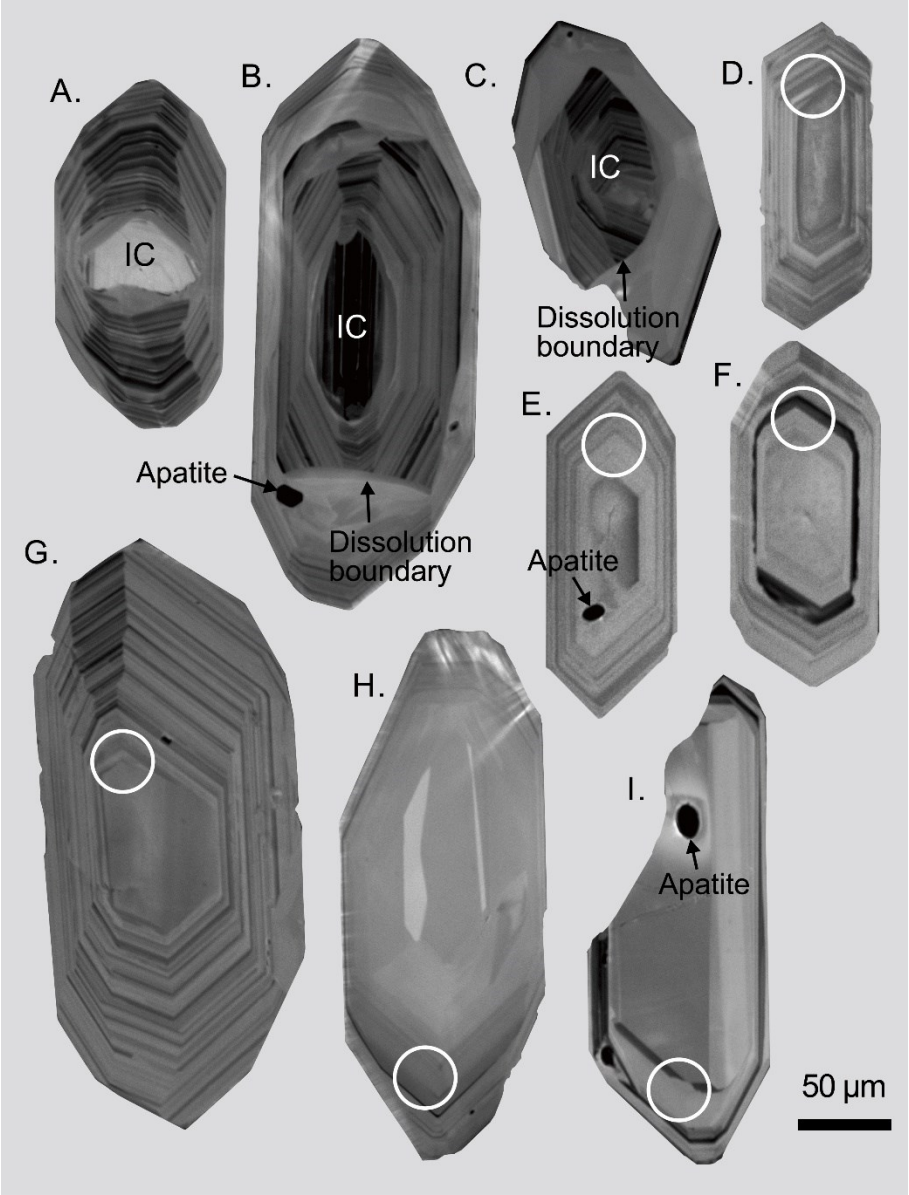

Figure 15. Cathodoluminescence images of magmatic zircon from the GIC. (A-C) Zircons containing inherited cores (IC), which are differentiated from their rim overgrowths by irregular or dissolution boundaries. (D-I) Representative CL images of oscillatory-zoned zircons with no or minor combination of sector zoning used for trace element analysis using LA-ICP-MS. White circle indicates laser diameter (32 µm). Sample: A, MGIqmd-1 MGI QMD; B, ESKDmd-1 ESKD MD; C, LSKDqd-3 LSKD QD; D, DICdior-2 DIC diorite; E, F, DICads-1 DIC andesite; G, MGIqmd-1 MGI QMD; H, ESKDmd-1 ESKD MD; I, LSKDqd-3 LSKD quartz diorite.

Table 3. Summary statistics of zircon geochemistry analyzed using LA-ICP-MS.

Sample	DICdior-1 (DIC diorite)			DICdior-2 (DIC diorite)			All DIC diorite		
n	29			17			46 (DICdior-1+DICdior-2)		
Statistic	Min	Mean	Max	Min	Mean	Max	Min	Mean	Max
Ti (ppm)	3.13	5.29	8.83	3.93	6.53	11.55	3.13	5.75	11.55
Y	659	1,036	1,790	650	1,147	2,016	650	1,077	2,016
La	0.01	0.11	0.37	0.00	0.04	0.22	0.00	0.08	0.37
Ce	15.48	27.58	77.33	10.25	24.39	44.86	10.25	26.40	77.33
Pr	0.04	0.09	0.20	0.04	0.08	0.24	0.04	0.09	0.24
Nd	0.58	1.31	2.58	0.71	1.34	3.93	0.58	1.32	3.93
Sm	1.25	2.80	5.65	1.83	3.02	7.48	1.25	2.88	7.48
Eu	0.66	1.25	1.74	0.83	1.39	2.93	0.66	1.30	2.93
Gd	7.44	16.98	33.06	11.23	18.59	42.87	7.44	17.57	42.87
Tb	2.98	6.26	12.40	3.69	6.76	14.29	2.98	6.44	14.29
Dy	42.17	82.81	161.48	47.96	86.93	159.94	42.17	84.34	161.48
Ho	19.94	34.04	62.17	20.20	37.86	62.87	19.94	35.45	62.87
Er	113.65	179.12	310.43	106.29	196.32	318.45	106.29	185.48	318.45
Tm	28.67	42.46	73.85	25.61	46.07	75.01	25.61	43.80	75.01
Yb	306.60	449.87	778.09	281.20	467.73	751.96	281.20	456.47	778.09
Lu	58.01	87.78	146.30	61.72	96.47	152.40	58.01	90.99	152.40
Hf	7,531	8,350	10,245	7,872	8,931	10,764	7,531	8,564	10,764
Th	119	231	626	78	195	367	78	218	626
U	186	330	810	104	247	490	104	299	810
REE^{tot}	638	932	1,626	575	987	1,578	575	953	1,626
T	675	717	768	694	735	795	675	724	795
Th/U	0.39	0.71	0.91	0.50	0.80	1.32	0.39	0.74	1.32
Yb_N/Gd_N	24.37	34.71	68.36	19.98	33.54	51.68	19.98	34.28	68.36
Ce/Nd	8.3	23.6	58.1	5.7	22.7	54.5	5.7	23.3	58.1
Ce/Ce*	35.2	126.2	361.3	24.8	131.0	343.7	24.8	128.0	361.3
Ce^{4+}/Ce^{3+}	103	381	987	50	329	1,004	50	361	1,004
Eu/Eu*	0.32	0.57	0.67	0.50	0.58	0.70	0.32	0.57	0.70
ΔFMQ	1.1	4.5	7.9	0.2	4.7	8.1	0.2	4.6	8.1

Table 3. Continued.

Sample	DICads-1 (DIC andesite)			MGIqmd-1 (MGI QMD)			ESKDmd-1 (ESKD MD)		
n		30			20			21	
Statistic	Min	Mean	Max	Min	Mean	Max	Min	Mean	Max
Ti (ppm)	2.73	4.79	9.91	1.70	6.56	12.06	2.36	5.26	10.60
Y	403	952	1,474	644	1,042	1,901	479	930	1,489
La	0.01	0.04	0.21	0.01	0.07	0.32	0.01	0.05	0.17
Ce	9.00	27.97	57.08	9.17	23.83	42.97	12.52	22.31	46.91
Pr	0.02	0.06	0.11	0.02	0.08	0.19	0.03	0.07	0.23
Nd	0.27	0.85	1.48	0.56	1.23	2.79	0.44	1.23	3.76
Sm	1.03	2.15	3.41	1.53	2.78	6.57	0.97	2.67	5.78
Eu	0.38	1.07	2.34	0.47	1.15	2.35	0.43	1.08	2.02
Gd	5.95	14.16	27.47	10.36	16.23	39.41	7.21	15.89	27.72
Tb	2.27	5.22	7.92	3.99	6.05	14.08	2.68	5.62	9.56
Dy	29.46	70.19	113.52	52.83	79.67	176.56	36.91	73.80	122.29
Ho	12.97	31.33	57.63	20.52	33.11	67.02	15.62	30.58	49.97
Er	71.69	169.76	352.61	105.77	179.32	324.71	82.60	158.58	260.60
Tm	17.58	39.95	68.68	24.78	43.91	70.94	19.42	36.78	60.69
Yb	185.30	404.09	721.70	258.51	473.29	669.34	203.29	374.87	609.20
Lu	42.29	86.39	144.25	49.68	96.51	144.44	42.28	76.41	123.06
Hf	8,139	9,212	14,018	7,748	9,126	10,657	8,611	9,423	9,941
Th	47	228	493	76	212	459	83	156	321
U	82	295	530	92	382	832	119	217	367
REE^{tot}	379	853	1,457	540	957	1,538	429	800	1,289
T	664	708	779	628	729	800	653	715	786
Th/U	0.34	0.76	1.14	0.25	0.65	1.04	0.53	0.71	1.00
Yb_N/Gd_N	20.43	36.81	51.18	20.49	38.64	71.17	22.02	30.50	44.83
Ce/Nd	10.6	33.8	60.1	7.3	23.8	54.3	5.7	22.2	37.6
Ce/Ce*	49.5	214.3	608.2	32.8	138.4	357.3	20.2	120.8	221.8
Ce^{4+}/Ce^{3+}	183	734	1,518	89	519	1,679	54	248	502
Eu/Eu*	0.47	0.59	0.75	0.26	0.53	0.70	0.44	0.51	0.57
ΔFMQ	1.2	6.3	11.8	1.3	4.8	8.3	0.0	4.2	6.7

Table 3. Continued.

Sample	LSKIqd-3 (LSKD QD)			Typical granite*		
n		20				
Statistic	Min	Mean	Max	Min	Mean	Max
Ti (ppm)	4.64	7.08	9.72	0.93	20.30	838
Y	271	991	2,330	8	1,856	22,190
La	0.01	0.08	0.27	0.002	13.90	5,253
Ce	7.94	25.00	63.25	0.28	58.20	7,011
Pr	0.02	0.07	0.19	0.01	2.35	79
Nd	0.26	1.19	2.98	0.04	13.90	461
Sm	0.68	2.75	6.63	0.30	10.90	337
Eu	0.33	1.20	2.54	0.01	1.55	39
Gd	4.05	16.94	41.33	1.90	44.40	474
Tb	1.62	6.15	14.69	0.73	15.30	100
Dy	20.14	79.97	191.51	1.6	193.0	2,156
Ho	8.19	32.51	77.05	5.00	64.10	339
Er	43.38	170.47	404.48	19.30	733.00	8,241
Tm	10.59	39.31	91.62	2.58	58.30	272
Yb	111.85	403.84	918.92	4.7	579.0	7,109
Lu	25.08	82.13	179.81	2	136	6,513
Hf	8,000	9,191	10,678	870	10,817	99,500
Th	42	217	632	0.01	544	46,210
U	62	249	845	0.01	1,270	1,798,000
REE^{tot}	234	862	1,995	1	1,422	15,645
T	709	745	778			
Th/U	0.60	0.82	1.40	<0.001	0.84	148
Yb_N/Gd_N	22.79	31.43	39.22	0.9	17.6	85.9
Ce/Nd	13.2	23.3	40.5			
Ce/Ce*	60.4	135.3	247.3	0.6	73	1,501
Ce^{4+}/Ce^{3+}	142	258	536			
Eu/Eu*	0.42	0.55	0.66	0.01	0.23	2
ΔFMQ	2.8	5.6	8.4			

*Typical granite data from GEOROC
http://georoc.mpch-mainz.gwdg.de/georoc/Csv_Downloads/Minerals_comp/ZIRCONS.csv

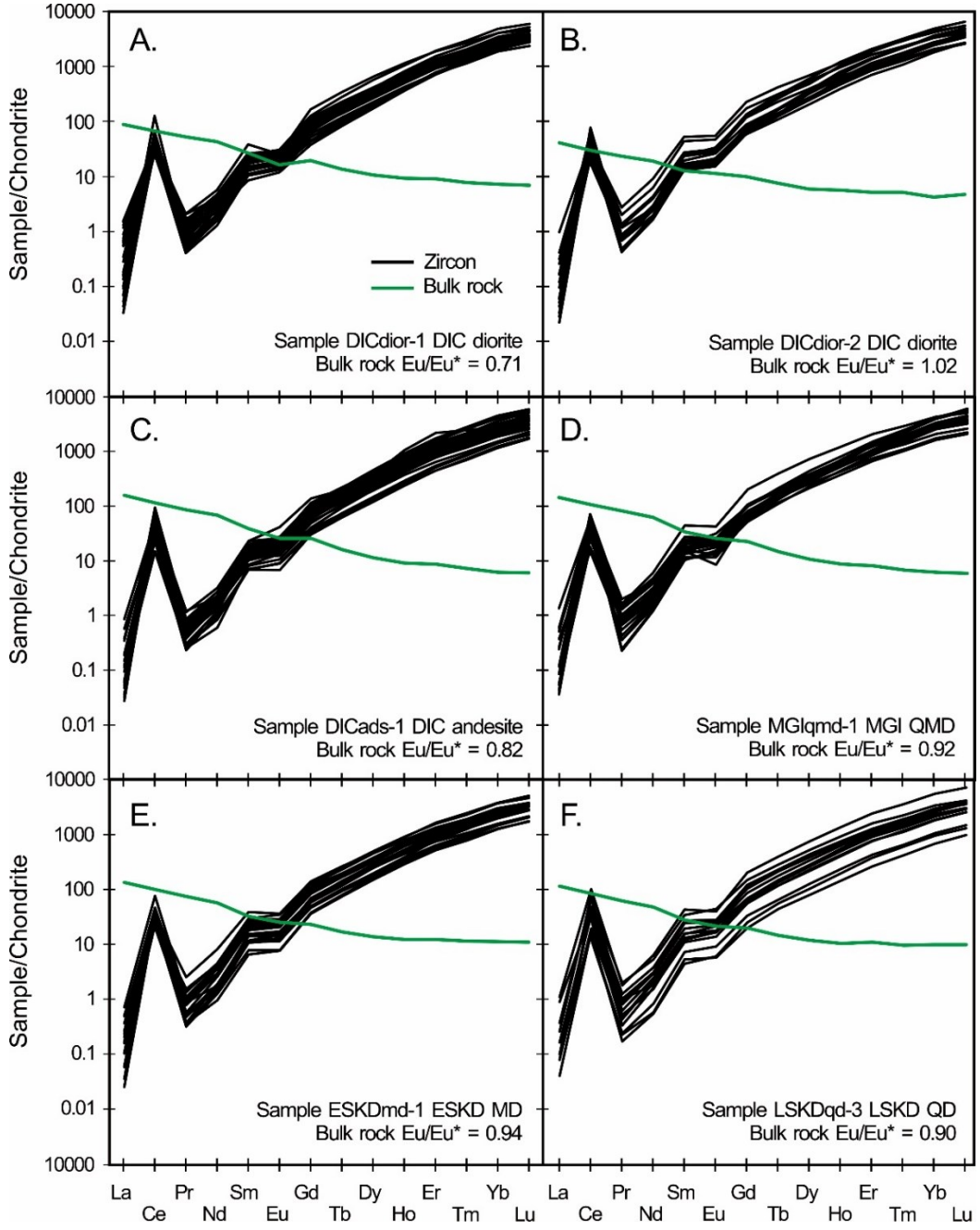

Figure 16. Chondrite-normalized REE diagrams for zircon and igneous rock samples of the GIC. Zircons show a pattern that includes low LREE and elevated HREE, with large positive Ce and small negative Eu anomalies. The bulk rock Eu/Eu* values range from 0.71 to 1.02.

3.2.5. Apatite chemistry

Apatite crystals are generally up to 200 μm in length. Textural relationships between apatite and other magmatic phases are well preserved in the syn- and post-mineralization intrusions (Fig. 17) but not in the pre-mineralization DIC at Grasberg. Apatites associated with (apatite inclusions in— and/or apatite crystals in contact with—) amphibole, plagioclase and anhydrite and apatite crystals within the groundmass were used for electron microprobe (EMP) analysis. Apatites within the groundmass are characteristically subhedral to anhedral and intergranular to the surrounding minerals (Fig. 17D). A summary of apatite EMP analysis is presented in Table 4.

Apatites associated with low-Al amphibole and plagioclase and apatites within the groundmass from the MGI QMD (n=30) are all chemically similar based upon measured SO_3 and Cl concentrations (0.07–0.44 wt.% SO_3 and 0.79–1.09 wt.% Cl) (Fig. 18A). In contrast, apatites associated with high-Al amphibole (n=17), low-Al amphibole and plagioclase (n=25), anhydrite (n=8) and apatites within the groundmass (n=12) from the ESKD MD fall into distinct populations in the SO_3 vs. Cl concentrations diagram (Fig. 18B). High-Al amphiboles from the ESKD MD host apatite inclusions with highest Cl concentrations ranging from 0.68 to 1.01 wt.% with moderate SO_3 contents (0.19–0.39 wt.%), whereas apatite crystals associated with low-Al amphibole and plagioclase contain 0.15–0.34 wt.% SO_3 and 0.58–0.79 wt.% Cl. Apatite grains, in contact with anhydrite from the ESKD MD have highest SO_3 contents ranging from 0.37 to 0.61 wt.%. The groundmass apatites of the ESKD MD have SO_3 and Cl concentrations of 0.16–0.38 and 0.52–0.71 wt.%,

respectively. In the LSKD QD, groundmass apatites show a similar SO_3 and Cl concentrations (0.20–0.57 wt.% SO_3 and 0.68–0.96 wt.% Cl) with those associated with low-Al amphibole, plagioclase and anhydrite (0.20–0.52 wt.% SO_3 and 0.59–0.98 wt.% Cl) (Fig. 18C).

Calibrated apatite/melt partitioning models of Parat el al. (2011) and Li and Hermann (2017) provide estimates of the melt S and Cl concentrations, respectively (Table 4). The melt Cl concentrations were computed at crystalline temperatures of co-existing amphiboles or the formation temperature of groundmass zircon when apatite occurs within the groundmass.

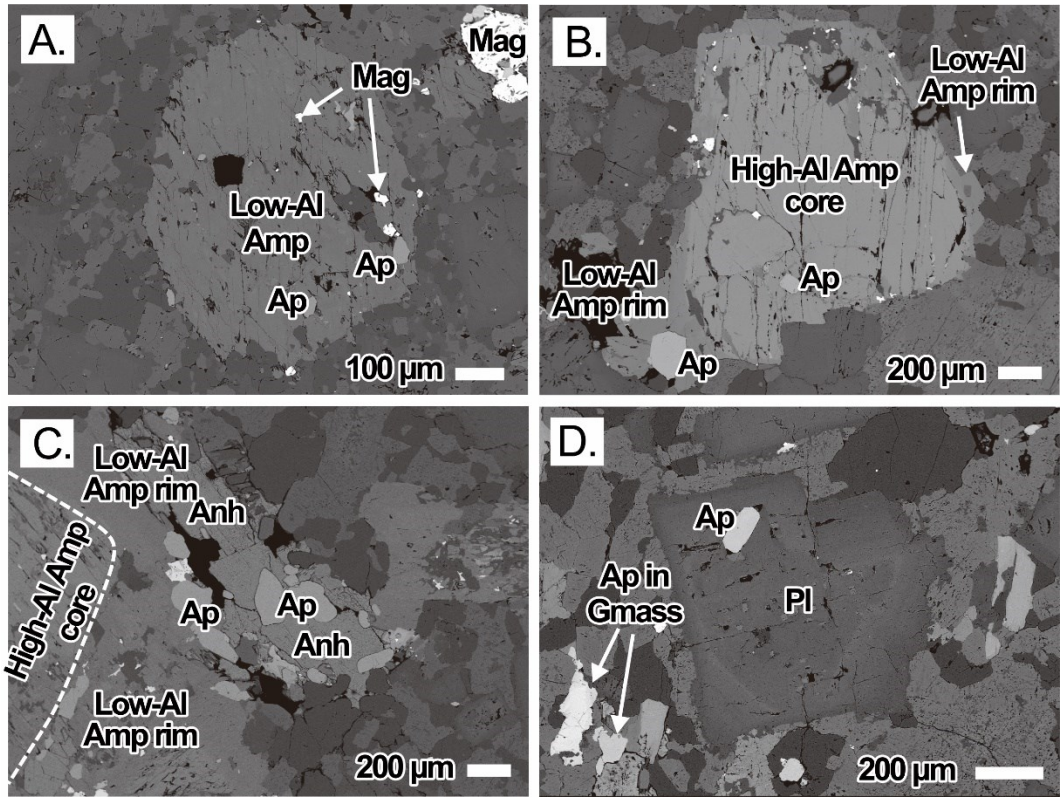

Figure 17. (A) Homogeneous low-Al amphibole phenocryst of the MGI QMD. Also shown are mineral inclusions such as magnetite and apatite. (B) Amphibole with disequilibrium texture of chemically distinct core and rim. The core is high-Al amphibole, whereas the rim is low-Al amphibole. Apatite is hosted in both high-Al core and low-Al rim. (C) The low-Al amphibole that is associated with anhydrite and apatite. (D) Apatite crystals that occur both in plagioclase crystal and within the groundmass. Groundmass apaptite is characteristically subhedral to anhedral and intergranular to the surrounding minerals.

Table 4. Representative analytical results of igneous apatite by EMP. Calibrated apatite/melt partitioning models of Parat el al. (2011) and Li and Hermann (2017) were used to calculate the concentrations of S and Cl in the melt, respectively. The temperature used for calculation is the crystalline temperatures of co-existing amphiboles or the formation temperature of groundmass zircon when apatite occurs within the groundmass.

Sample	MGIqmd-2 (MGI QMD)						ESKImd-1 (ESKI MD)		
Associated minerals (*n*)	Low-Al amphibole and plagioclase (9)			Groundmass (20)			High-Al amphibole (17)		
Avg. T (°C)		716			666			890	
Statistic	Min	Mean	Max	Min	Mean	Max	Min	Mean	Max
CaO (wt.%)	53.88	54.34	55.83	53.29	54.34	55.47	53.07	54.12	54.65
P_2O_5	39.58	40.39	40.87	39.88	40.47	41.14	39.81	40.49	41.14
F	2.76	2.96	3.17	2.36	2.80	3.19	2.38	2.74	3.15
Cl	0.85	0.96	1.09	0.79	0.93	1.09	0.68	0.85	1.01
Na_2O	0.00	0.11	0.20	0.00	0.09	0.21	0.05	0.11	0.21
MgO	0.00	0.00	0.01	0.00	0.00	0.00	0.00	0.01	0.04
SiO_2	0.00	0.00	0.00	0.00	0.00	0.00	0.00	0.00	0.00
MnO	0.07	0.13	0.19	0.09	0.14	0.22	0.11	0.15	0.19
TiO_2	0.00	0.01	0.04	0.00	0.00	0.06	0.00	0.02	0.06
Al_2O_3	0.00	0.01	0.05	0.00	0.00	0.02	0.00	0.01	0.02
SO_3	0.10	0.28	0.44	0.07	0.31	0.44	0.19	0.28	0.39
Total	96.84	97.74	99.24	96.42	97.70	99.52	96.23	97.42	98.67
O=F, Cl	-1.53	-1.46	-1.38	-1.54	-1.39	-1.19	-1.48	-1.35	-1.17
Total	95.38	96.28	97.71	95.13	96.31	98.03	94.95	96.07	97.19
Ca (apfu)	9.62	9.70	9.84	9.56	9.70	9.80	9.59	9.69	9.81
P	5.65	5.69	5.75	5.66	5.71	5.77	5.68	5.73	5.78
F	1.46	1.56	1.66	1.25	1.48	1.67	1.28	1.45	1.64
Cl	0.24	0.27	0.31	0.22	0.26	0.30	0.19	0.24	0.29
Na	0.00	0.04	0.06	0.00	0.03	0.07	0.02	0.04	0.07
Mg	0.00	0.00	0.00	0.00	0.00	0.00	0.00	0.00	0.01
Si	0.00	0.00	0.00	0.00	0.00	0.00	0.00	0.00	0.00
Mn	0.01	0.02	0.03	0.01	0.02	0.03	0.02	0.02	0.03
Ti	0.00	0.00	0.00	0.00	0.00	0.01	0.00	0.00	0.01
Al	0.00	0.00	0.01	0.00	0.00	0.00	0.00	0.00	0.00
S	0.01	0.04	0.06	0.01	0.04	0.05	0.02	0.03	0.05
OH^{calc}	0.09	0.17	0.27	0.08	0.26	0.49	0.17	0.31	0.51
*X*F	0.73	0.78	0.83	0.63	0.74	0.83	0.64	0.72	0.82
*X*Cl	0.12	0.14	0.15	0.11	0.13	0.15	0.09	0.12	0.14
*X*OH	0.05	0.08	0.14	0.04	0.13	0.25	0.08	0.15	0.25
Cl_{melt} (wt%)	0.46	0.74	1.15	0.26	0.50	1.03	0.41	0.68	1.07
S_{melt} (ppm)	13	46	88	11	46	84	21	36	61

Table 4. Continued.

Sample	ESKImd-1 (ESKI MD)			ESKImd-1 (ESKI MD)			ESKImd-1 (ESKI MD)		
Associated minerals (*n*)	Low-Al amphibole and plagioclase (25)			Anhydrite (8)			Groundmass (12)		
Avg. T (°C)		763			763			682	
Statistic	Min	Mean	Max	Min	Mean	Max	Min	Mean	Max
CaO (wt.%)	53.16	54.45	54.93	53.87	54.37	55.02	54.32	54.66	55.18
P_2O_5	39.86	40.94	41.77	40.60	41.08	41.75	40.83	41.33	41.90
F	2.74	3.04	3.42	2.48	2.87	3.15	2.58	3.01	3.48
Cl	0.58	0.66	0.79	0.49	0.67	0.73	0.52	0.65	0.71
Na_2O	0.00	0.09	0.19	0.10	0.14	0.20	0.00	0.10	0.19
MgO	0.00	0.00	0.02	0.00	0.00	0.01	0.00	0.01	0.04
SiO_2	0.00	0.00	0.00	0.00	0.00	0.00	0.00	0.00	0.00
MnO	0.13	0.18	0.25	0.12	0.20	0.24	0.14	0.18	0.22
TiO_2	0.00	0.01	0.02	0.00	0.01	0.02	0.00	0.01	0.02
Al_2O_3	0.00	0.00	0.03	0.00	0.00	0.01	0.00	0.00	0.03
SO_3	0.15	0.26	0.34	0.37	0.49	0.61	0.16	0.24	0.38
Total	96.07	98.21	99.33	97.82	98.47	99.68	98.15	98.77	99.46
O=F, Cl	-1.57	-1.43	-1.31	-1.45	-1.36	-1.21	-1.58	-1.41	-1.24
Total	94.71	96.78	97.76	96.58	97.11	98.30	96.87	97.36	98.12
Ca (apfu)	9.52	9.64	9.79	9.48	9.60	9.66	9.54	9.62	9.74
P	5.64	5.73	5.78	5.69	5.73	5.76	5.70	5.75	5.79
F	1.42	1.59	1.76	1.29	1.50	1.65	1.34	1.56	1.79
Cl	0.16	0.19	0.22	0.14	0.19	0.20	0.14	0.18	0.20
Na	0.00	0.03	0.06	0.03	0.05	0.06	0.00	0.03	0.06
Mg	0.00	0.00	0.01	0.00	0.00	0.00	0.00	0.00	0.01
Si	0.00	0.00	0.00	0.00	0.00	0.00	0.00	0.00	0.00
Mn	0.02	0.03	0.03	0.02	0.03	0.03	0.02	0.03	0.03
Ti	0.00	0.00	0.00	0.00	0.00	0.00	0.00	0.00	0.00
Al	0.00	0.00	0.00	0.00	0.00	0.00	0.00	0.00	0.01
S	0.02	0.03	0.04	0.05	0.06	0.08	0.02	0.03	0.05
OH^{calc}	0.08	0.22	0.39	0.20	0.32	0.51	0.06	0.26	0.47
*X*F	0.71	0.80	0.88	0.65	0.75	0.82	0.67	0.78	0.90
*X*Cl	0.08	0.09	0.11	0.07	0.09	0.10	0.07	0.09	0.10
*X*OH	0.04	0.11	0.19	0.10	0.16	0.25	0.03	0.13	0.23
Cl_{melt} (wt%)	0.33	0.53	1.04	0.29	0.39	0.53	0.23	0.41	0.88
S_{melt} (ppm)	17	32	47	55	118	198	18	30	60

Table 4. Continued.

Sample	LSKIqd-2 (LSKI quartz diorite)								
Associated minerals (*n*)	Low-Al amphibole (11)			Anhydrite (6)			Groundmass (10)		
Avg. T (°C)	739			739			675		
Statistic	Min	Mean	Max	Min	Mean	Max	Min	Mean	Max
CaO (wt.%)	53.71	54.44	54.88	54.42	54.57	54.71	53.18	54.38	55.31
P_2O_5	40.41	41.12	41.91	40.75	41.29	41.80	40.39	41.10	41.61
F	2.16	2.82	3.34	2.48	2.89	3.07	2.26	2.71	3.12
Cl	0.59	0.82	0.95	0.75	0.89	0.98	0.68	0.86	0.96
Na_2O	0.05	0.11	0.17	0.08	0.11	0.15	0.06	0.14	0.21
MgO	0.00	0.00	0.01	0.00	0.00	0.00	0.00	0.00	0.01
SiO_2	0.00	0.00	0.00	0.00	0.00	0.00	0.00	0.00	0.00
MnO	0.08	0.13	0.17	0.10	0.13	0.15	0.09	0.11	0.14
TiO_2	0.00	0.00	0.02	0.00	0.01	0.04	0.00	0.01	0.04
Al_2O_3	0.00	0.00	0.02	0.00	0.01	0.02	0.00	0.00	0.03
SO_3	0.20	0.28	0.41	0.28	0.38	0.52	0.20	0.38	0.57
Total	97.16	98.35	99.58	98.15	98.85	99.48	96.35	98.35	99.73
O=F, Cl	-1.55	-1.37	-1.12	-1.50	-1.42	-1.21	-1.52	-1.34	-1.17
Total	95.75	96.97	98.02	96.90	97.44	98.08	95.19	97.02	98.53
Ca (apfu)	9.53	9.63	9.73	9.52	9.60	9.71	9.55	9.62	9.70
P	5.72	5.75	5.80	5.72	5.74	5.76	5.71	5.75	5.78
F	1.14	1.47	1.71	1.30	1.50	1.60	1.21	1.42	1.61
Cl	0.16	0.23	0.27	0.21	0.25	0.27	0.19	0.24	0.27
Na	0.02	0.03	0.05	0.02	0.03	0.05	0.02	0.04	0.07
Mg	0.00	0.00	0.00	0.00	0.00	0.00	0.00	0.00	0.00
Si	0.00	0.00	0.00	0.00	0.00	0.00	0.00	0.00	0.00
Mn	0.01	0.02	0.02	0.01	0.02	0.02	0.01	0.02	0.02
Ti	0.00	0.00	0.00	0.00	0.00	0.00	0.00	0.00	0.00
Al	0.00	0.00	0.00	0.00	0.00	0.00	0.00	0.00	0.00
S	0.02	0.03	0.05	0.03	0.05	0.06	0.02	0.05	0.07
OH^{calc}	0.11	0.30	0.60	0.14	0.25	0.49	0.14	0.34	0.54
*X*F	0.57	0.74	0.86	0.65	0.75	0.80	0.60	0.71	0.81
*X*Cl	0.08	0.12	0.13	0.10	0.12	0.14	0.09	0.12	0.14
*X*OH	0.05	0.15	0.30	0.07	0.13	0.24	0.07	0.17	0.27
Cl_{melt} (wt%)	0.29	0.48	0.79	0.29	0.57	0.80	0.24	0.37	0.64
S_{melt} (ppm)	22	38	72	36	69	134	22	74	175

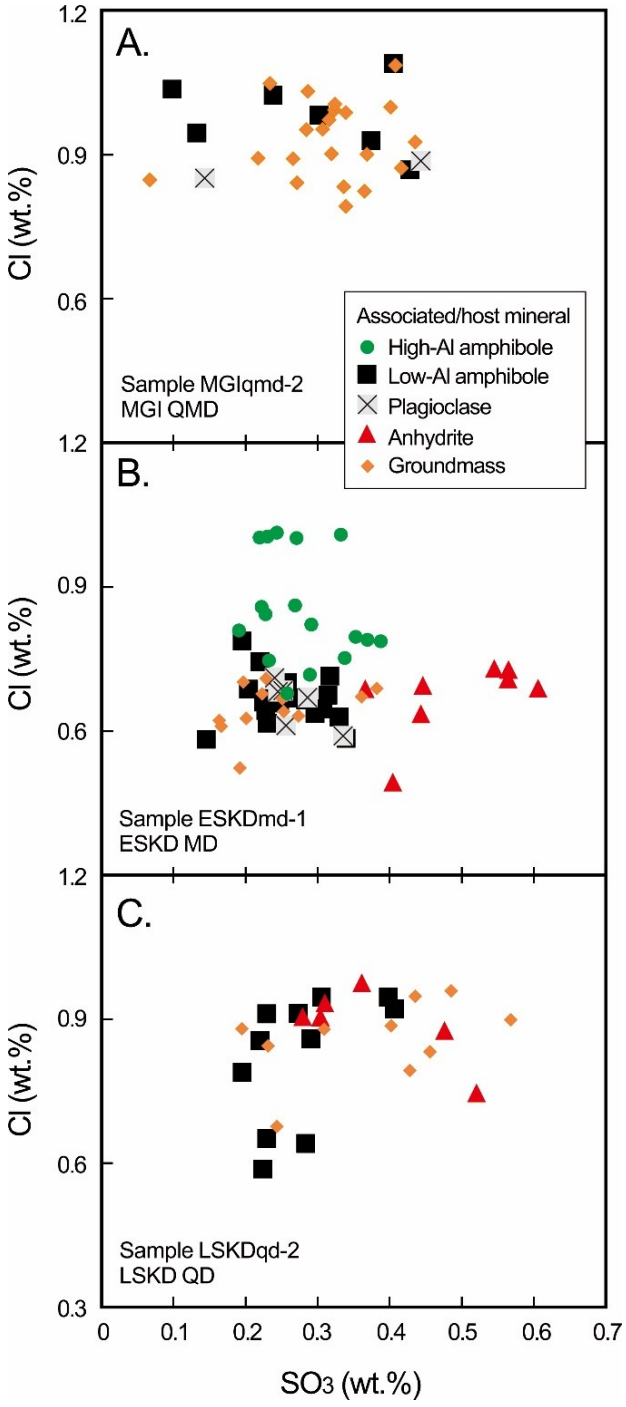

Figure 18. Measured SO_3 vs. Cl concentrations in apatite. (A) Apatite inclusions associated with low-Al amphibole and plagioclase and apatite within the groundmass from the MGI QMD are all chemically similar based upon measured SO_3 and Cl concentrations. (B) The ESKD mozodiorite contains apatite that fall into distinct populations. (C) Groundmass apatite from the LSKD QD is characteristically high in SO_3 and Cl concentrations relative to that associated with low-Al amphibole, plagioclase and anhydrite.

3.3. Discussion

3.3.1. Timing of amphibole, zircon and apatite crystallizations

The amphibole geothermobarometry (Ridolfi et al., 2010; Mutch et al., 2016) applied to the low-Al amphibole from the syn-mineralization MGI QMD showed approximate crystallization temperature and pressure of 730–700 (avg. 710) °C and 1.1–0.7 (avg. 1.0) kbar, respectively. Amphibole-plagioclase thermometry (see Anderson, 1996) indicates a remarkably similar crystallization temperature range of 720–700 °C. The syn-mineralization ESKD MD contains amphiboles with a chemically distinct disequilibrium texture of core and rim; the high-Al cores are estimated to have formed at approximately 900–850 (avg. 880) °C and 4.3–3.3 (avg. 4.0) kbar, whereas the low-Al rims and associated low-Al amphibole phenocrysts crystalized at 790–720 (avg. 760) °C and 1.9–1.0 (avg. 1.6) kbar. The low-Al amphiboles from the post-mineralization LSKD crystallized at 750–700 (avg. 720) °C and 1.4–0.9 (avg. 1.1) kbar.

The combined temperature-pressure estimates indicate that the low-Al amphiboles crystallized in an upper-crustal magma chamber at approximately 5 km depth, whereas the high-Al amphibole in the deeper zone at approximately 15 km depth (mid-crustal zone). These data lead to the following model of magma crystallization. A magma batch containing high-Al amphibole was injected into the bottom of the MGI upper-crustal magma chamber. The MGI QMD porphyry magma rose soon after such an injection. The younger ESKD MD was derived from the mixed magma (hereafter referred to as ESKD magma), as evidenced by the disequilibrium texture of amphibole hosted by the porphyry.

Fractionation of high-Al amphibole may have reduced the middle REE (MREE) contents of residual melts (Rohrlach & Loucks, 2005; Richards, 2011; Chambefort et al., 2013) because amphibole is the major host of MREE (e.g., Watanabe et al., 2016). All ESKD low-Al amphiboles are depleted in the MREE compared with the high-Al amphiboles (Fig. 14), confirming that the low-Al amphibole was formed at lower temperature and pressure than those of high-Al amphibole. Negative Eu and Sr anomalies in high-Al amphiboles (Fig. 14) may indicate co-crystallization of calcic plagioclase. Although Eu and Sr anomalies are observed in high-Al amphiboles, the low-Al amphiboles have larger negative Eu (except for the LSKD QD), Ba and Sr anomalies compared with the high-Al amphibole, indicating a co-crystallization of biotite, plagioclase and K-feldspar in the upper-crustal magma chamber. Barium may substitute for K in biotite and K-feldspar, whereas Eu and Sr substitutes readily for Ca in plagioclase (Wilson, 1989; Wilke and Behrens, 1999). Small negative Eu anomaly in the LSKD low-Al amphibole indicates suppression of prior or co-crystallization of plagioclase. In addition, crystallization of titanite and apatite in the upper-crustal magma chamber may accommodate Y, resulting in the depletion of Y content in low-Al amphibole. These trace element behaviors are in agreement with our petrographic observation where the low-Al amphiboles appear to have been equilibrated chemically with plagioclase, K-feldspar, biotite, titanite (-magnetite-quartz), and some apatite.

Calculated zircon saturation temperatures for the MGI QMD, ESKD MD, and LSKD QD vary from 750 to 710 °C, indicating that their parental magmas were zircon undersaturated when emplaced into the upper crust. The Ti-in-zircon

thermometer of all GIC samples provides estimates for zircon crystallization temperatures ranging from 800 to 630 °C. Zircon crystallization temperatures may fall below the solidus temperature, indicating that temperature, αTiO_2 and αSiO_2 are not the only factors governing Ti partitioning in zircon (Fu et al., 2008). Because of Zr-free modal phase growth (Harrison et al., 2007), zircon started to form at 800 °C, higher the calculated zircon saturation temperatures.

Some zircon and apatite crystals appear to have been equilibrated chemically with low-Al amphibole and associated plagioclase in MGI QMD, ESKD MD and LSKD QD samples. Zircon grains formed at temperature lower than that of the low-Al amphiboles (<700 °C) are represented by those in the groundmass with apatites. Thus, the zircon and apatite in the groundmass may have crystallized both in the upper-crustal magma chamber (~5 km depth) and from the residual melt after low-Al amphibole crystallization toward the end of magma solidification.

The ESKD MD in particular contains apatite that occurs as inclusion in high-Al amphibole. This occurrence indicates that the apatite formed at depth of ~15 km prior to the mixing of the MGI upper-crustal magma and high-Al amphibole-bearing deep-sourced magma. The igneous mineral paragenesis for amphibole, zircon and apatite is illustrated in Figure 19.

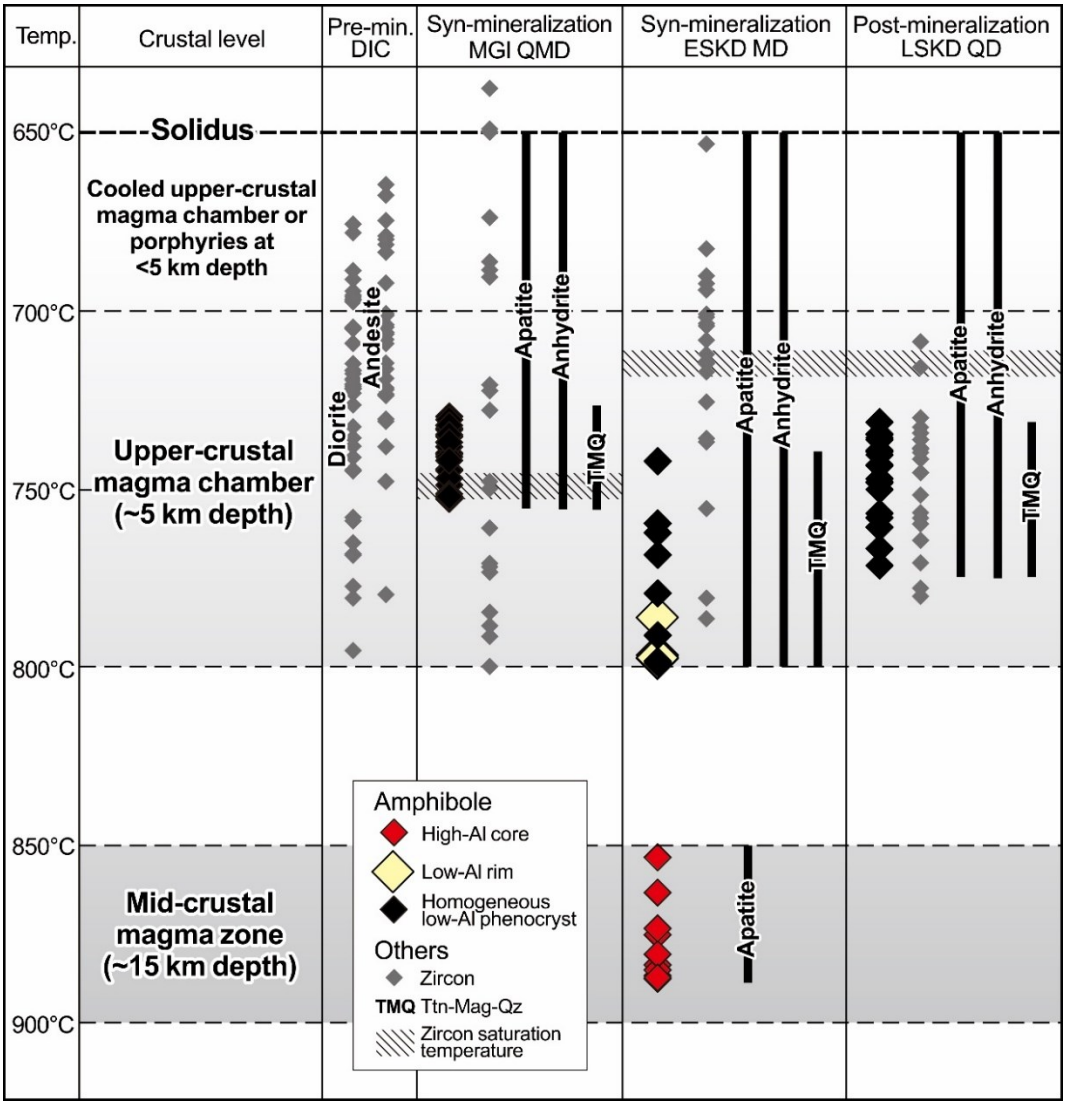

Figure 19. Igneous mineral paragenesis for amphibole, zircon, apatite, anhydrite and the assemblage of titanite-magnetite-quartz with respect to formation temperature and crustal level. The plotted DIC diorite zircons are the combination of two samples DICdior-1 and DICdior-2.

3.3.2. Evolution of the oxidation state of upper-crustal magmas

The high oxidation state of magmas at Grasberg is manifested by the presence of magmatic anhydrite (see Chambefort et al., 2008; Hutchinson and Dilles, 2019) and the assemblage of titanite-magnetite-quartz associated with magnesiohornblende (see Wones, 1989) in the syn- and post-mineralization porphyries. High oxygen fugacity is an important factor for the generation of porphyry Cu deposits because Cu solubility increases with increasing fO_2 (Zajacz et al., 2012). Although trace amounts of fine-grained pyrite and chalcopyrite (~10 μm) in magnetite grains in the ESKD MD are observed, the intrusive rocks are generally sulfide-free. This observation indicates that the contribution to the melt S concentration from sulfide was insignificant (Jugo, 2009) and the fO_2 was above the sulfide-sulfur oxide buffer.

The application of fO_2 equation by Ridolfi et al. (2010) provides estimates for the syn- and post-mineralization intrusions at Grasberg. The low-Al amphiboles from the syn-mineralization MGI QMD record an oxidized condition of approximately FMQ+3.4 for the upper-crustal magma. A less oxidized (FMQ+1), deep-sourced magma batch injected into such a strongly oxidized upper-crustal magma chamber as indicated by high-Al amphiboles contained in the syn-mineralization ESKD MD. This mixing produced a hybrid magma with fO_2 of approximately FMQ+2.7, from which the ESKD MD porphyry was derived. This process is strongly evidenced by the ESKD amphiboles that have a disequilibrium texture of high-Al core (FMQ+1) and low-Al rim (FMQ+2.7). The upper-crustal magma evolved to a more oxidized condition (FMQ+3.3) following the stage of porphyry mineralization as indicated by the post-mineralization LSKD QD low-Al

amphibole.

The amphibole fO_2 estimates are in agreement with V concentration in both high-Al and low-Al amphiboles. Vanadium partitioning between amphibole and melt is related to magma fO_2, becoming more compatible in amphibole crystallized from a more reduced magma (Iveson et al., 2018). The ESKD high-Al amphiboles contain high V (280–392 ppm) compared with the low-Al amphiboles from all samples (139–241 ppm), confirming that the ESKD high-Al amphibole crystallized at lower fO_2 than low-Al amphibole.

As a result of mixing between MGI and deep-sourced magmas, the low-Al amphiboles of the ESKD are different from low-Al amphiboles of other intrusions. The ESKD low-Al amphibole is enriched in LREE compared with low-Al amphiboles from both MGI and ESKD magmas (Fig. 14A-2). Crystallization of LREE-enriched minerals such as allanite could have reduced the melt LREE content. Because crystallization of allanite is related to a high magma oxidation state (Watanabe et al., 2017), elevated LREE content in the ESKD low-Al amphibole may be due to the suppression of allanite crystallization caused by a relatively low fO_2 (FMQ+2.7) compared with both MGI (FMQ+3.4) and LSKD (FMQ+3.3).

Chondrite-normalized REE diagrams for GIC zircons show a typical pattern of oxidized magmas that include large positive Ce and small negative Eu anomalies (Fig. 16). More oxidized conditions would increase Ce and Eu contents in zircon because the proportion of Ce^{4+} and Eu^{3+} are increased. Ce^{4+} is partitioned into zircon because of its identical charge and size to Zr. Because the proportion of Eu^{3+}

increases with increasing oxidation state and it is not partitioned into plagioclase, zircons from a more oxidized magma may have higher Eu/Eu* and correspondingly smaller negative Eu anomaly in the chondrite-normalized diagram (Wilke and Behrens, 1999; Ballard et al., 2002).

In the case of the pre-mineralization DIC, zircon is the most promising mineral for estimating magma oxidation state because amphibole and other indicator minerals are hydrothermally altered. Zircons from the DIC diorite and andesite yield the mean values of Ce^{4+}/Ce^{3+} of 361 and 734, respectively (Fig. 20A). The DIC diorite is slightly older than the DIC andesite (Wafforn, 2017), indicating that the upper-crustal magma evolved to a more oxidized condition during the DIC magmatism. The fact that zircons of the DIC andesite crystallized at lower temperature range indicates that the change in magma fO_2 was related to the cooling of upper-crustal magma chamber. Zircons from the syn-mineralization MGI QMD yield the elevated mean value of the Ce^{4+}/Ce^{3+} of 519, whereas those from the syn-mineralization ESKD MD record a lower value of 248. The post-mineralization LSKD QD zircons have the Ce^{4+}/Ce^{3+} mean value of 258.

The Ce^{4+}/Ce^{3+} ratios are well correlated with both Ce/Ce* and Ce/Nd but poorly correlated with Eu/Eu* (Fig. 21). Europium (Eu^{2+}) is incorporated in plagioclase (Wilke and Behrens, 1999), whereas titanite incorporates Sm and Gd to a greater extent than Eu (Loader et al., 2017). This partitioning could have affected the melt Eu/Eu* and corresponding Eu anomaly in zircon. However, the average values of Eu/Eu* show a similar pattern of fO_2 fluctuation to Ce^{4+}/Ce^{3+}, Ce/Ce*, and Ce/Nd during the evolution of GIC magmas (Fig. 20). The means of fO_2 values

calculated from Ce anomalies in zircons (Table 3; Trail et al., 2012) also indicate a similar fluctuation pattern shown by Ce^{4+}/Ce^{3+}, Ce/Ce*, and Ce/Nd. These results are in agreement with the fO_2 estimated from amphibole and confirm that the syn-mineralization ESKD magma evolved as a result of mixing with a more reduced magma from depth. Although fO_2 estimates computed from zircon have wide interquartile ranges and are relatively more oxidized than those obtained from amphibole (Fig. 22), such a change in magma fO_2 provides essential information for this study.

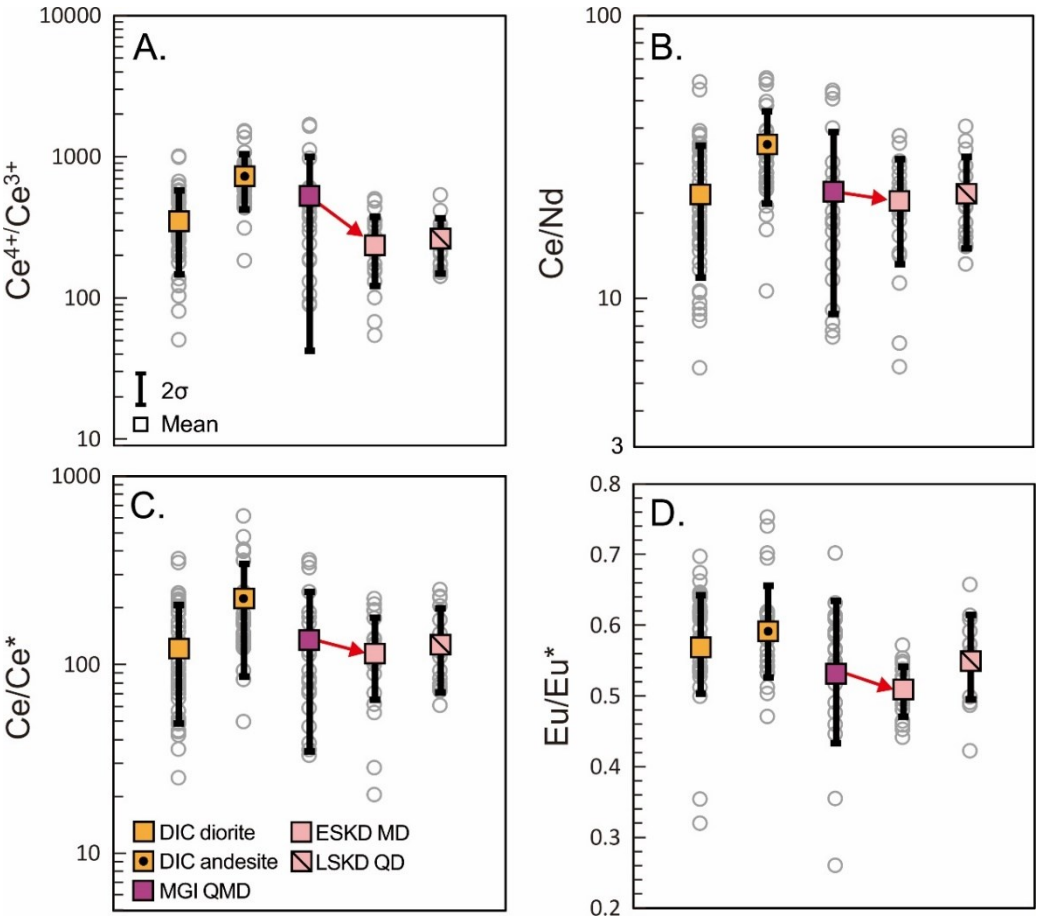

Figure 20. Ce^{4+}/Ce^{3+}, Ce/Nd, Ce/Ce* and Eu/Eu* ratios in zircons from the GIC intrusions. Their mean values show a similar fO_2 fluctuation during the GIC magma evolution. The decrease in magma oxidation state during syn-mienralization period (red arrow) is in agreement with amphibole data, and suggest that upper-crustal magma was evolved to a more reduced condition as a result of mixing of magma of two distinct oxidation states. The plotted DIC diorite zircons are the combination of two samples DICdior-1 and DICdior-2.

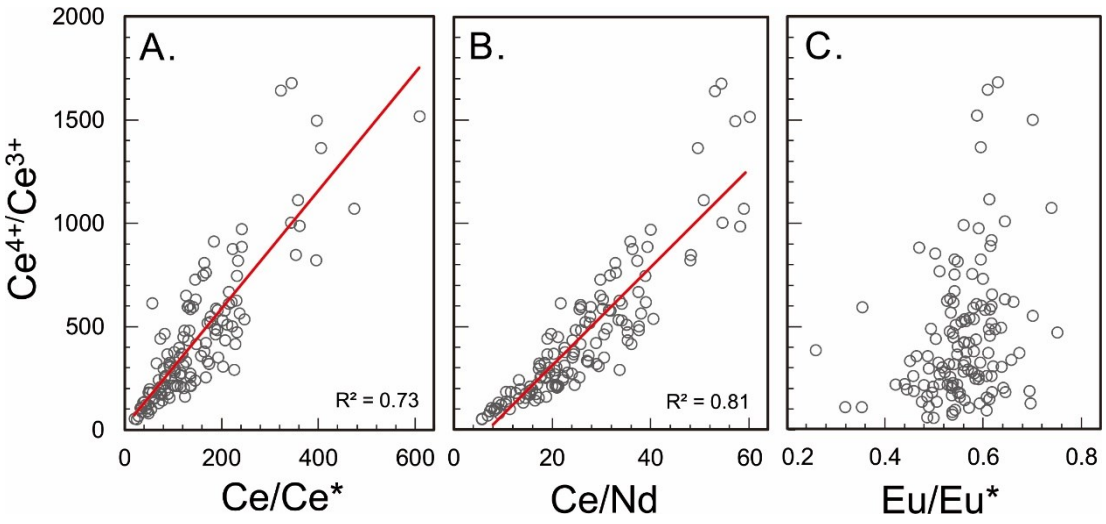

Figure 21. Correlations between Ce and Eu anomalies. (A, B) All Ce anomalies are correlated well with correlation coefficients of 0.73 to 0.81 for Ce/Ce* vs. Ce^{4+}/Ce^{3+} and Ce/Nd vs. Ce^{4+}/Ce^{3+}, respectively. (C) Eu/Eu* is poorly correlated with Ce^{4+}/Ce^{3+}. Such a poor correlation may be due to prior or co-crystallizations of plagioclase and titanite (see text).

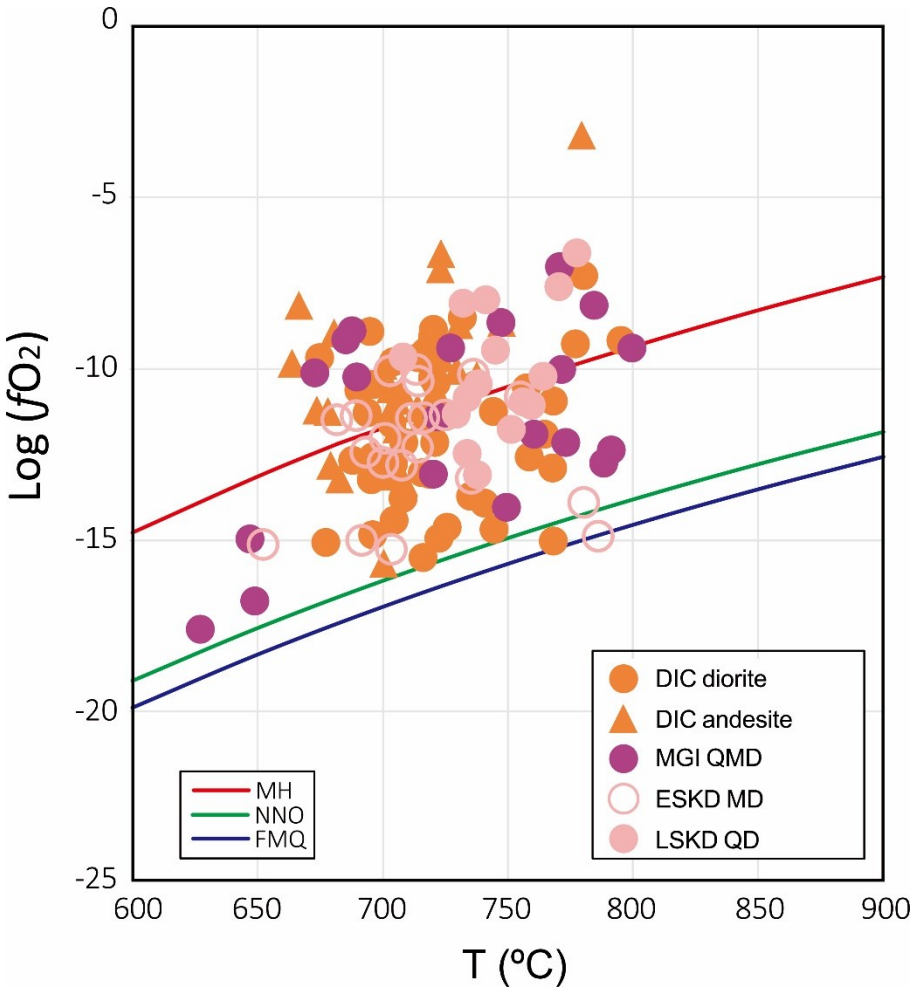

Figure 22. The fO_2 values calculated from Ce anomalies in zircons (see Trail et al., 2012) plotted in the temperature vs. log (fO_2) diagram. Buffer values at given temperature calculated using P = 1500 kbar (average amphibole crystallization pressure in the upper-crustal magma chamber). The fO_2 estimates have wide interquartile ranges and are relatively more oxidized than those obtained from amphibole. These values are not consistent with mineralogical evidence where hematite is not observed (overestimate? as noted by Dilles et al., 2015).

3.3.3. Magmatic degassing of S- and Cl-bearing fluids

The melt S and Cl concentrations were computed on the basis of calibrated apatite/melt partitioning models of Parat el al. (2011) and Li and Hermann (2017), respectively. The variation of melt S and Cl concentrations during the evolution of GIC magmas provides information for the timing of S and Cl partitions into fluids (Fig. 13), which are divided into three main sequences.

Sequence-1: Apatite crystals from the syn-mineralization MGI QMD indicate an upper-crustal magma chamber containing 13–88 ppm S (avg. 46 ppm) and 0.46–1.15 wt.% Cl (avg. 0.74 ppm) at the time of low-Al amphibole and plagioclase phenocryst crystallization (Fig. 23A). The concentration of Cl in the residual melt is lower (0.26–1.05 wt.%, avg. 0.53 wt.%) than the melt during phenocryst crystallization, whereas S content is similar (Fig. 23A). Groundmass apatites that record a melt low in Cl (0.2–0.4 wt.%) are interpreted to have formed after high-Al amphibole and plagioclase had completely crystallized. The crystallization of anhydrous minerals such as plagioclase can have contributed to the fluid saturation of the residual melt (Cloos, 2001). Amphibole only rarely takes up more than about 1 wt.% of the magmatic H_2O, and may slow the increasing rate of H_2O (Cloos, 2001). However, the effect of amphibole crystallization is not significant. The saturation of H_2O may have been attained after at least 60% of the melt crystallized at 2 kbar or higher, under which the exsolved fluids are metal-rich brines (Cline and Bodnar, 1991). Plagioclase alone comprise up to 55 vol.% of the MGI QMD.

Sequence-2: At Grasberg, the magmatic degassing of a large amount of S-bearing fluids occurred following the recharge of the more reduced magma from

depth in the MGI-related upper-crustal magma chamber. The ESKD porphyry formed from such an fO_2-evolved, mixed upper-crustal magma. The melt S concentration had already been depleted when low-amphibole and plagioclase crystallized (avg. 32 ppm vs. 47 ppm for the upper-crustal melt before mixing and degassing; Fig. 23B). This indicates that S-bearing fluids degassed at approximately 800 °C and 2 kbar or higher, prior to the low-Al amphibole and plagioclase crystallization.

Sulfur dioxide is the principal S species in gases evolved from GIC magmas (Henley et al. 2015; Mavrogenes and Blundy 2017; Henley and Seward 2018; Mernagh et al. 2020). However, the bulk of S in oxidized GIC magmas is present as sulfate. The reduction of sulfate to SO_2 may require oxidation of Fe^{2+} in the melt (e.g., Jugo et al., 2005; Jugo, 2009; Dilles et al., 2015). I suggest that mixing of magmas of two distinct oxidation states could have generated SO_2 by the reduction of sulfate via oxidation of Fe^{2+}. The reaction occurred as the following equation of Dilles et al., (2015):

$$CaSO_4 + 2FeO = CaO + SO_2 + 2FeO_{1.5} \quad (1)$$

where in the case of Grasberg, the MGI upper-crustal magma chamber provided sulfate (e.g., as anhydrite), whereas large amounts of Fe^{2+} were derived from the injected reduced magma. Although the MGI upper-crustal magma is more oxidized than that of the ESKD, anhydrite in the MGI QMD is remarkably less abundant. This indicates that anhydrite was decomposed to generate SO_2 during magma evolution.

The apatite data indicate that deep-sourced magma injected into the bottom of the MGI upper-crustal magma chamber was relatively low in S (21–61 ppm, avg. 36 ppm). Thus, the injected magma did not cause sulfur saturation but increased the melt Fe^{2+}/Fe^{tot}.

Sequence-3: Apatite crystals within the groundmass record lowest Cl concentrations for the ESKD magma (0.23–0.88 wt.%, avg. 0.41 wt.%; Fig. 23B). This result is similar to the sequence-1, by which the exsolution of Cl-bearing fluids occurred following low-Al amphibole and plagioclase crystallization. The depletions of both Cl and S are not observed in the post-mineralization LSKD QD (Fig. 23C). The melt S vs. Cl concentrations diagram for the LSKD QD show a scattered pattern, which suggests that some apatites crystallized from the older melt.

3.3.4. High-S apatite associated with anhydrite

Apatite crystals associated with anhydrite have anomalously high S content and correspondingly high calculated melt S concentration (Figs. 18B, 23B). There are two possibilities in which an anhydrite host can affect the measured S content in apatite (e.g., van Hoose et al., 2013): 1) during the analytical measurement, the electron beam interacts with some of the neighboring anhydrite, 2) diffusion of S between anhydrite and apatite. The first scenario is avoided by monitoring measured CaO, P_2O_5, F, and Cl concentrations, whereas S diffusion is more complicated to rule out. In the ESKD MD sample, high S content in apatite is observed only when apatite is associated or in contact with anhydrite. However, high S concentration is also observed in the LSKD apatite associated with

plagioclase and apatite in the groundmass (Fig. 23 C). Systematic line analysis also indicates that high S contents are not restricted to the rim areas of apatite crystals. Thus, assuming that S exchange by diffusion between anhydrite and apatite was negligible, the presence of high-S apatite associated with anhydrite may indicate an elevated melt S concentration at anhydrite saturation (e.g., 1 vol.% anhydrite is approximately 2300 ppm S; Hutchinson and Dilles 2019).

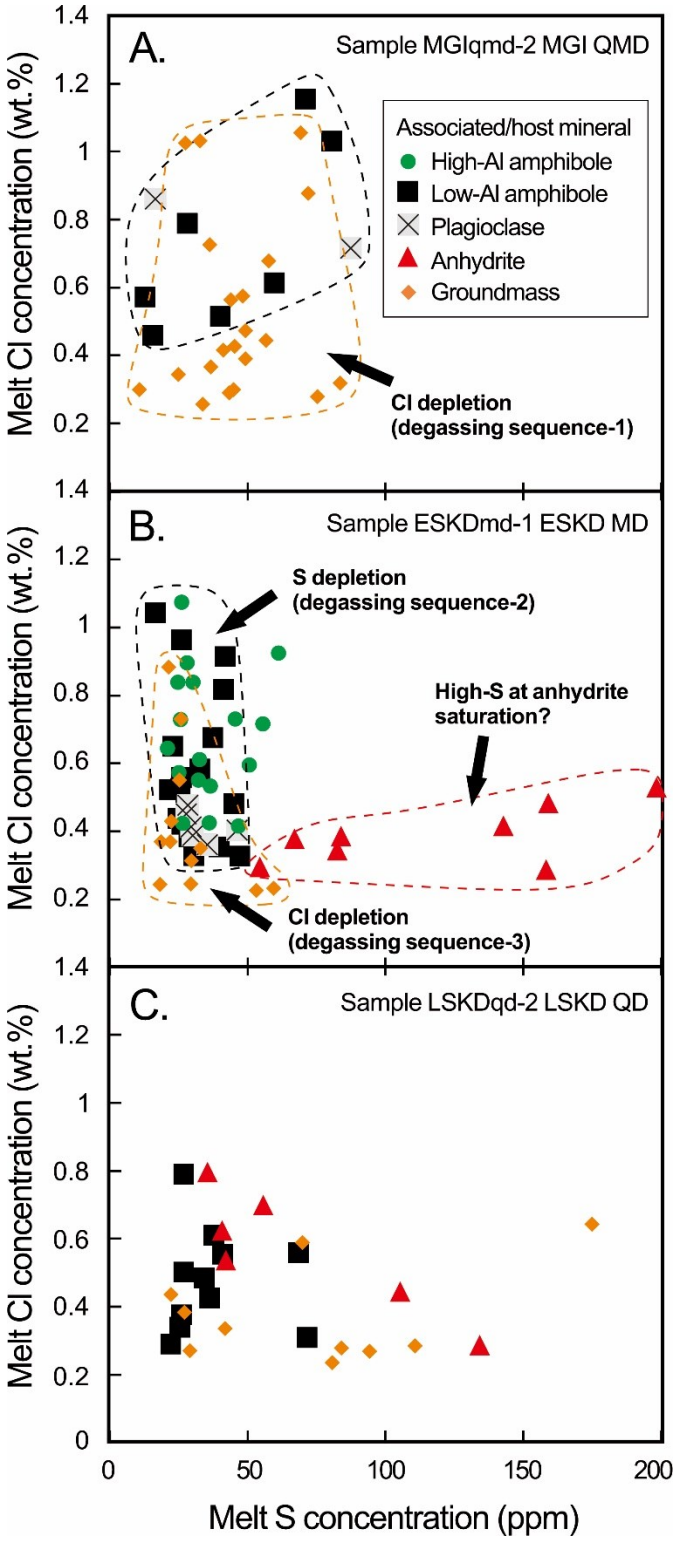

Figure 23. Plots of calculated melt S vs. Cl concentrations on the basis of apatite composition. (A) MGI QMD. (B) ESKD MD. (C) A scattered pattern for the post-mineralization LSKD QD. See Parat el al. (2011) and Li and Hermann (2017) for the calculations.

3.3.5. Implications for the genesis of porphyry Cu deposits

Porphyry Cu deposits form at 2–5 km depth, in the cupola zone, where volatiles degassed from the oxidized upper-crustal magma chamber are channeled (Burnham, 1979; Shinohara and Hedenquist, 1997; Cloos, 2001; Weis, 2015; Richards 2018). Hydrous arc magmas that contain 3–5 wt.% H_2O are generally oxidized with the fO_2 ranging from FMQ+1.7 to FMQ+3.7 (de Hoog et al., 2004; Wang et al., 2007). Shen et al. (2015) proposed that the fO_2 value of magma at FMQ+2.7 discriminates large and intermediate-size porphyry deposits from those of the small deposits. Both low-Al amphibole and zircon chemistry indicates average fO_2 values greater than or equal to FMQ+2.7for the GIC magma. This high magma oxidation state prevented the loss of metals from the melt because sulfide remains undersaturated during magma evolution prior to ore deposit formation (Carroll and Rutherford, 1985, 1988; Hattori and Keith 2001; Jugo et al. 2005; Hattori 2018).

The lifetimes of magmatic systems of porphyry associated plutons are commonly several million years, but focusing of a large volume of fluid in the cupola zone occurs on a time scale of <100 k.y. (e.g., von Quadt et al., 2011; Chiaradia et al., 2013; Large et al., 2018). Such a long-lived magmatic system is arguably essential in preparation for the fluid saturation required for economic mineralization (Halter et al., 2005). My observations strongly indicate that the degassing of volatiles at Grasberg occurred intermittently during magma evolution (Fig. 24). This implies that Cl and S may not be necessarily degassed from the upper-crustal magmas at the same time and localized accumulation of ore-forming fluids is required for an efficient hydrothermal system. Cloos (2001) suggested that

mineralizing fluids are stored in a stable fluid pocket beneath the cupola zone and the discharge of these fluids may begin when a sufficiently large amount of fluid accumulates. Richards (2018) emphasized that a sudden fluid flow triggered by an external factor such as earthquake or volcano sector collapse could lead to efficient fluid flux in the copula zone. At Grasberg, such a sudden pulse can be indicated by highly-mineralized, brecciated pre-mineralization DIC, which was interpreted by MacDonald and Arnold (1994) to represent the root of a volcanic system. The matrix of the brecciated DIC is dominated by anhydrite and chalcopyrite in ore bidies, which formed at a temperature range of 645–475 °C (Sulaksono et al., 2021). This temperature range indicates that mineralization occurred immediately after a sudden discharge of ore-forming fluids.

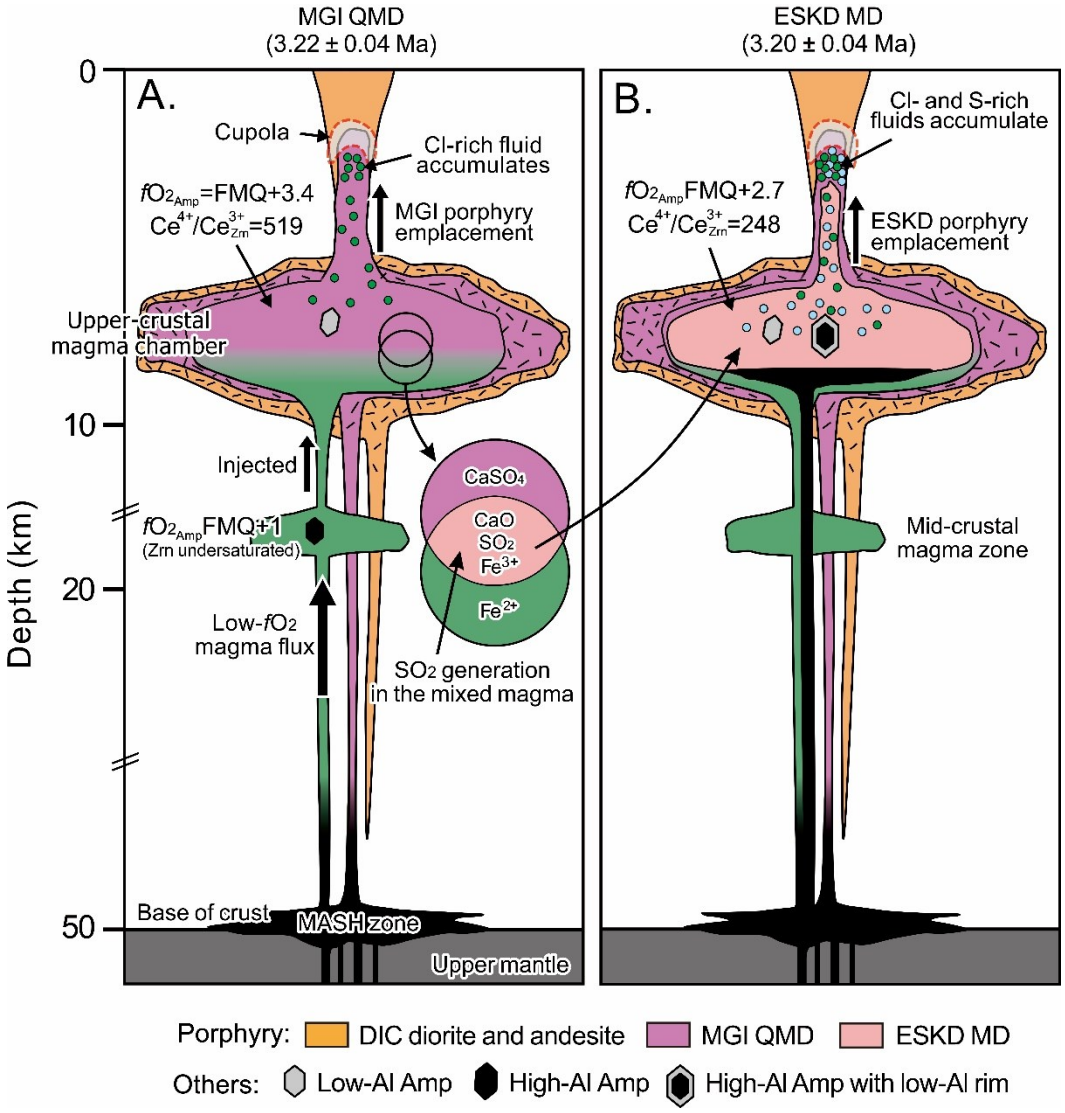

Figure 24. Conceptual model of syn-mineralization magmatic processes related to the degassing of volatiles and their accumulation in a pocket beneath the cupola. (A) The degassing sequence-1 (Cl-rich; see text) occurred during cooling and crystallization of the oxidized MGI upper-crustal magma. The rise of the bubbly MGI QMD porphyry occurred soon after the injection of a reduced magma from depth. Mixing of magmas of two distinct oxidation states generate SO_2 via the oxidation of Fe^{2+} (see text). (B) SO_2-rich (sequence-2) fluid degassed from the mixed magma prior to low-Al amphibole and plagioclase crystallization, followed by Cl-rich volatiles (sequence-3) after such silicate phenocrysts had already crystalized. The fluids are stored in a stable fluid pocket beneath the cupola zone. The discharge occurred after a sufficiently large amount of fluid accumulates (Cloos, 2001) or due to an external trigger such as earthquake or volcano sector collapse (Richards, 2018).

Chapter 4: Reduction of Oxidized Sulfur during Hydrothermal Processes

4.1. Samples and analytical methods

For this study, 198 samples were collected from four drill holes (IF3580-99, INF41-02, GRD39-01 and KL98-10-21) which in combination intersect a ~2 km depth range through the Grasberg porphyry Cu deposit (from ~3600 to ~1600 m elevation; Fig. 25). Most samples come from 3600–2600 m elevation because there are few deep drill holes below 2600 m elevation, and no samples were taken between 3600 m elevation and the pre-mine surface at 4400 m because drill cores from there are strongly weathered. Samples from IF3580-99, INF41-02 and GRD39-01 are weakly to pervasively altered, whereas samples from KL98-10-21 (1900–1600 m elevation) are generally unaltered. One mineralized vein sample was also collected from the Grasberg open pit at 3100 m elevation. Magnetic susceptibilities used to determine magnetite abundance were measured using a SM30 MS meter. Vein and alteration mineral paragenesis was determined from core logging observations and from thin section examinations using a Nikon ECLIPSE LV100N POL microscope and a JEOL® JSM-6610 LV SEM equipped with an Oxford X-Max^N energy-dispersive X-ray detector at Akita University. Biotite was analyzed for major elements, whereas sulfur-bearing veins were analyzed for sulfur isotope ratios.

1. Biotite

Thin sections were examined using a Nikon ECLIPSE LV100N POL microscope

and a JEOL® JSM-6610 LV scanning electron microscope equipped with an Oxford X-MaxN energy-dispersive X-ray detector at Akita University (accelerating voltage = 15 kV, beam current = 2.2 nA). Crystals selected for quantitative analysis include unaltered biotite, hydrothermal biotite that replace both igneous amphibole and biotite, and hydrothermal biotite that present as vein. Quantitative mineral microanalyses were conducted using a JEOL® JXA-8230 SuperProbe at Akita University with an accelerating voltage of 15 kV, a 20 nA beam current, and a 5 μm electron beam size. Astimex Inc., USA mineral standards were used such as fluorite (F), jadeite (Na), periclase (Mg), An65 plagioclase (Al and Ca), quartz (Si), tugtupite (Cl), orthoclase (K), rutile (Ti,), rhodonite (Mn) and hematite (Fe) for biotite and amphibole. All analytical data were corrected using the ZAF matrix-correction program.

2. Sulfur isotope ratio

Sulfide and coexisting sulfate minerals were handpicked from vein samples. Purity of the minerals was checked using binocular microscope. Approximately 20 mg of sulfides was decomposed by adding 20 mL concentrated HNO_3 and 2 mL Br_2 at ~90°C, whereas ~100 mg of anhydrite was dissolved with HCl at room temperature. Approximately 200 mg of powdered sulfide-free bulk-rock sample was also dissolved with HCl. Anhydrite (1.5 vol.%) and apatite (0.1vol.%) are the main sulfur-bearing minerals in this sample. The acidified solution was passed through a cation exchange column to avoid coprecipitation with other cations. 10 mL of 10% $BaCl_2 \cdot 2H_2O$ was added to the eluent to precipitate $BaSO_4$. The $BaSO_4$ was packed

with V_2O_5 in tin foil. The packed samples were then loaded into the automatic sampler attached to a Thermo Fisher Flash 2000 Elemental Analyzer, where the samples were combusted in a quartz tube at 1020°C. SO_2 gas was liberated by gas chromatography. Isotopic ratios were measured using a Thermo Fisher Scientific Delta V Advantage isotope ratio monitoring mass spectrometer at Akita University. We used standards of International Atomic Energy Agency (IAEA), including sea water sulfate (IAEA-NBS-127, $\delta^{34}S$ = 20.30‰) and barium sulfate (IAEA-SO-5, 0.50‰) and IAEA-SO-6, –34.10‰). The sulfur isotopic ratios are presented in the standard $\delta^{34}S$ nomenclature in permil difference relative to Canyon Diablo troilite. The analytical uncertainty is ±0.2‰.

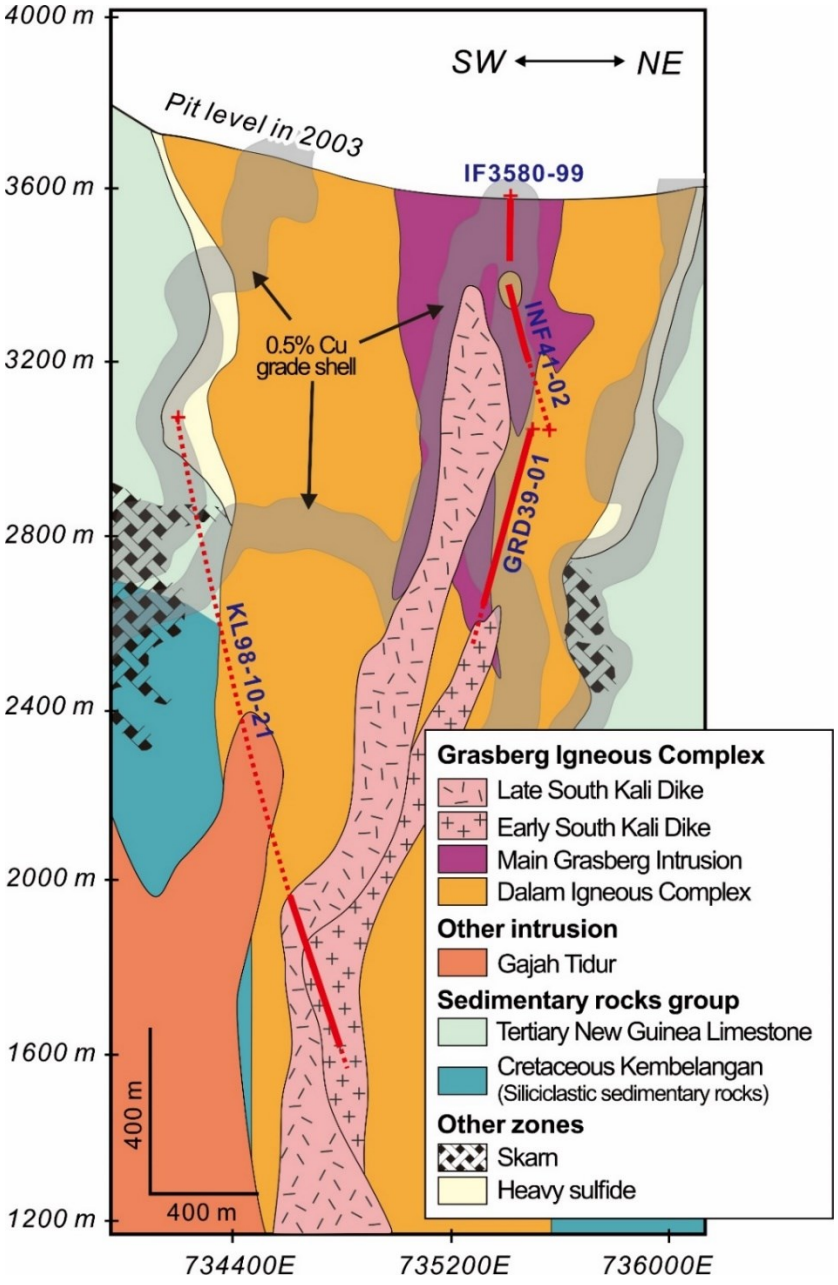

Figure 25. General SW-NE cross section of the GIC with the drill holes IF3580-99, INF41-02, GRD39-01 and KL98-10-21 (red solid lines are samples studied). All samples from the IF3580-99, INF41-02 and GRD39-01 are hydrothermally altered, whereas samples from the KL98-10-21 are unaltered. Heavy sulfide zone contains >20% pyrite, with covellite, galena, enargite and sphalerite.

4.2. Results

4.2.1. Hydrothermal alteration-mineralization

The Grasberg porphyry deposit is dominated by a sub-vertical, cylindrical zone of potassic alteration centered on the MGI that is surrounded by a selvage of sericite alteration that extends to the margins of the GIC. These alteration zones are patchily overlap the margins of the ESKD but are truncated by the LSKD (Leys et al., 2012). The highest Cu grades (>2% Cu) are associated with the strongest and most pervasive potassic, and to a lesser extent sericite alteration zones. Almost all of the drill core samples studied lie within the predominantly potassic-altered Grasberg >0.5 wt.% Cu zone, with only a few from a lower-grade, deeper zone in drill hole GRD39-01 (Fig. 25).

Most samples studied are potassic altered that comprises K-feldspar, biotite, magnetite, quartz, anhydrite, chalcopyrite, bornite, apatite and rutile. Very few samples contain sericite alteration that overprints potassic alteration and comprises white mica, quartz, chlorite, anhydrite, pyrite, chalcopyrite, bornite, apatite and rutile. This alteration typically replaces plagioclase and K-feldspar in centimeter-scale (<5 cm wide) alteration selvages to 1–10 mm-wide chalcopyrite and quartz-pyrite-chalcopyrite veins. Sericite alteration is uncommon in the samples studied because sampling was focused on MGI and DIC intrusions within the central potassic alteration zone, however, in DIC rocks outboard of this zone sericite alteration is intense and pervasive (Leys et al., 2012).

Based on detailed mineralogical and textural relationships, the potassic and

sericite alteration zones are sub-divided into 10 detailed alteration and vein stages:

1. K-feldspar alteration

K-feldspar is one of the most abundant hydrothermal minerals in potassically-altered rocks, and typically replaces plagioclase phenocrysts and groundmass phases. K-feldspar has mostly irregular crystal shapes with serrate or wavy margins. K-feldspar also occurs as selvages around anhydrite veinlets (Fig. 26A) as well as within them (Fig. 26B). Locally, K-feldspar and magnetite replace igneous biotite.

2. Replacement Biotite

Hydrothermal biotite within the potassic alteration zone is common in samples from drill holes IF3580-99, INF41-02 and GRD39-01 as pseudomorphs after igneous amphibole (Fig. 26C), and less commonly replaces primary biotite phenocrysts (Fig. 26D). Igneous amphibole is replaced by shreddy hydrothermal biotite, with or without magnetite, K-feldspar, quartz, rutile, apatite, anhydrite and minor chalcopyrite and bornite. Igneous biotite is replaced by fine-grained biotite aggregates which occasionally contain hydrothermal magnetite (Fig. 26D).

Hydrothermal biotite after amphibole and biotite phenocrysts is characterized by higher Mg# and lower Fe, Ti and Al^{tot} contents than igneous biotite (Table 5). In annite-siderophyllite-phlogopite-eastonite quadrilateral diagrams most hydrothermal biotites have chemical compositions more enriched in the phlogopite component than igneous biotite (Fig. 27).

3. Magnetite veins

In addition to replacing mafic minerals within the GIC potassic alteration zone, magnetite is commonly found as veins (Figs. 26E, F) in samples from drill holes IF3580-99 and INF41-02 and the upper part of GRD39-01. These magnetite veins may also contain quartz and biotite, are generally <3 cm thick and lack selvages. Magnetite veins are particularly abundant in a sample from drill hole INF41-02 where they occur as sheeted structures (Fig. 26F).

4. Biotite veinlets

Biotite veinlets are common within GIC potassic alteration and are typically <1 mm thick, discontinuous and irregular and in places associated with magnetite, K-feldspar, anhydrite, quartz and minor chalcopyrite and bornite (Fig. 26E). K-feldspar selvages around biotite veinlets which cut plagioclase phenocrysts are often significantly wider than the veinlets. Vein biotites have chemical compositions enriched in the phlogopite component (Fig. 27).

5. Sugary quartz veins

Sugary quartz veins are widely seen in potassically-altered samples from drill hole INF41-02 and the upperpart of GRD39-01 as locally intense stockworks. The veins are wavy, irregular and discontinuous, generally <5 cm thick, and consist of fine-grained, polygonal quartz aggregates often with magnetite, biotite, chalcopyrite, bornite and molybdenite (Figs. 26E, G, K).

6. Comb quartz veins

Comb quartz veins are abundant in potassically-altered samples from well-

mineralized (1~4% Cu) sections of drill hole IF3580-99 and INF41-02 and are characterized by subhedral quartz crystals (Figs. 26G, H). These veins are typically 1 to 5 cm thick, lack selvages and often contain central zones rich in chalcopyrite and bornite especially in their wider segments (Fig. 26H).

7. Planar quartz veins

Planar quartz veins (Figs. 26H, J) are common in potassically-altered samples from holes GRD39-01 and INF41-02 and in places contain minor amounts of biotite, chalcopyrite, and bornite. Veins vary from <1 cm up to 5 cm and typically have sharp planar walls with no selvages.

8. Anhydrite-chalcopyrite veins

Anhydrite-chalcopyrite veins are generally 1 to 5 cm thick, although they can reach >50 cm in places, and are seen in all IF3580-99, INF41-02 and GRD39-01 potassically-altered samples, especially in zones containing high Cu grades up to ~4% Cu. Veins lack selvages (Figs. 26I, J), display increasing amounts of anhydrite relative to chalcopyrite with depth and are associated with quartz, biotite, bornite and molybdenite.

9. Chalcopyrite veins ± sericite selvages

Chalcopyrite veins are widely observed within all potassically-altered samples from IF3580-99, INF41-02 and GRD39-01 drill holes and are characteristically narrow (~1 to 5 mm) but may reach 3 cm and are mostly planar. The veins locally contain bornite, anhydrite, quartz and apatite, and have sericite selvages (Fig. 26E). The

selvages contain white mica with or without chlorite, anhydrite, quartz, pyrite, chalcopyrite, bornite, apatite and rutile. This vein type typically occurs in the well-mineralized transition zone from the GIC potassic to the sericite alteration zone where grades can locally reach up to ~3% Cu.

10. Pyrite-chalcopyrite-quartz veins with sericite selvages

Pyrite-chalcopyrite-quartz (± anhydrite) veins are common in samples from INF41-02 and GRD39-01, are mostly 1 to 10 mm thick and have associated sericite selvages that are mainly <5 cm thick (Fig. 26K). The selvages comprise white mica that replaces plagioclase and K-feldspar that can have associated chlorite, anhydrite, quartz, pyrite, chalcopyrite, bornite, apatite and rutile. Veins of this type are abundant within GIC sericite alteration zones and where veining is most intense all wallrock minerals are completely replaced by sericite.

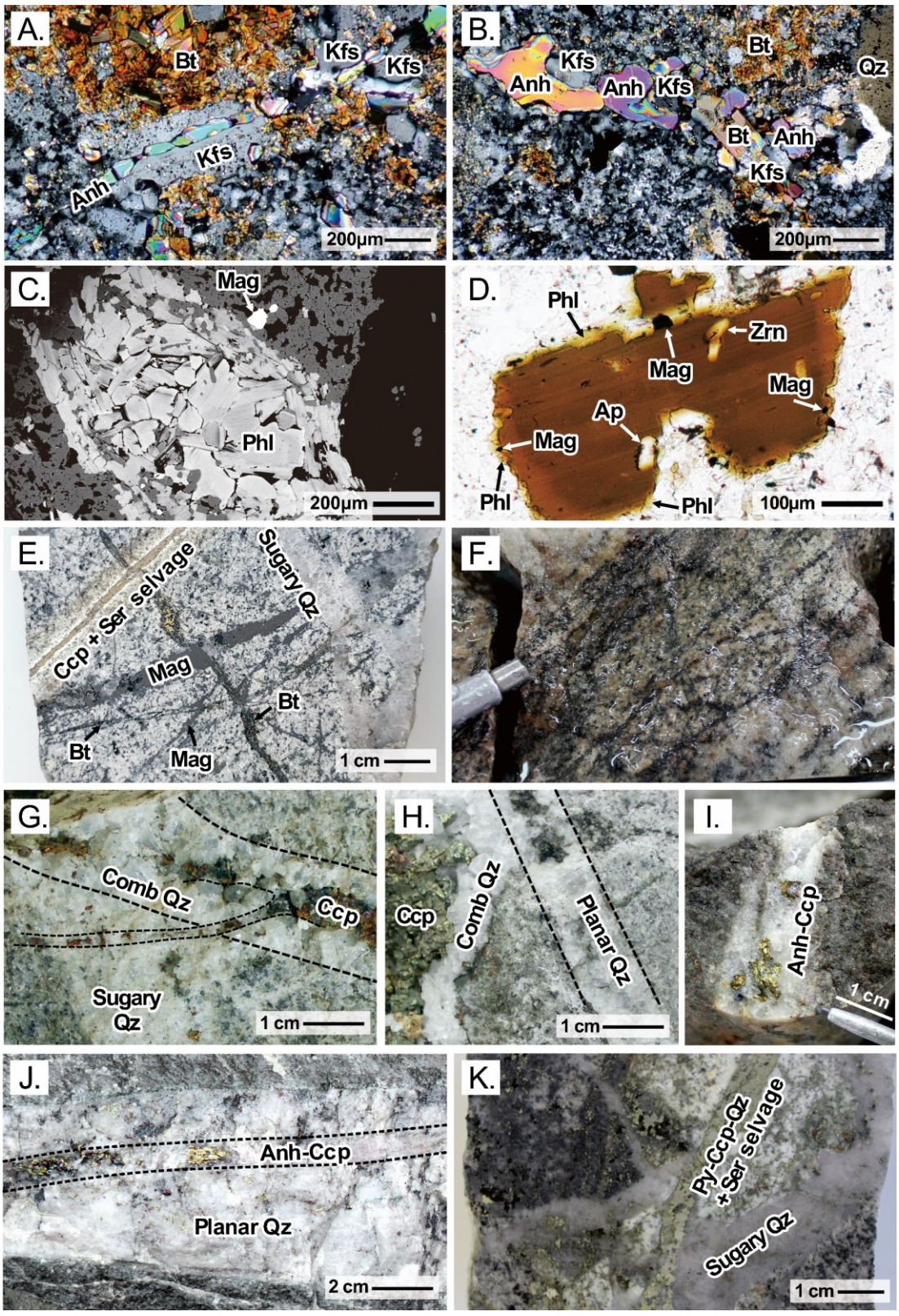

Figure 26. Successive vein and alteration stages observed in the drill cores studied. (A) Anhydrite veinlet with K-feldspar alteration selvage. Sample GRD-35, 2887 m elevation. (B) Discontinuous, wavy anhydrite-dominated veinlet associated with K-feldspar and biotite. Sample GRD-35. (C) BEI of hydrothermal biotite with chemical compositions more enriched in phlogopite component after igneous amphibole. Sample INF-11, 3215 m elevation. (D) Hydrothermal phlogopite after igneous biotite. Also shown are associated hydrothermal magnetite grains. Sample INF-11. (E) Cross cutting vein relationships: magnetite veins are cut by biotite stage veins, and both magnetite and biotite veins are cut by a sugary quartz vein and a chalcopyrite vein with sericite selvage. Sample INF-22, 3296 m elevation. (F) Parallel, sheeted vein structure of magnetite. Sample GMCINF-12. (G) Sugary quartz vein, cut by a comb quartz vein, which contains a centerline of chalcopyrite. A chalcopyrite seam extending form the chalcopyrite centerline also cuts the sugary quartz vein. Sample INF-8, 3199 m elevation. (H) Comb quartz vein that contains a chalcopyrite centerline, cut by planar quartz vein with minor biotite. Sample INF-13, 3218 m elevation. (I) Anhydrite-chalcopyrite veins with some quartz and molybdenite. Sample GRD-45, 2838 m elevation. (J) Planar quartz vein with minor chalcopyrite and bornite cut by an anhydrite-chalcopyrite vein (Grasberg open pit mine, 3100 m elevation). (K) Pyrite-chalcopyrite-quartz vein with sericite alteration selvage cutting an earlier sugary quartz vein. Sample INF-18, 3275 m elevation. See Figure 3 caption for mineral abbreviations.

Table 5. Representative analytical results of igneous and hydrothermal biotite by electron microprobe. Formula unit calculations based on 22 oxygen. Total iron as FeO. Abbreviations: Ig, igneous; H-B hydrothermal biotite that replaces igneous biotite; H-V, hydrothermal biotite in veins; H-P, hydrothermal biotite in amphibole pseudomorphs. ※, Igneous biotite that is partly replaced by hydrothermal biotite. Samples: FrESKD-1, unaltered ESKD MD from 1850 m elevation; FrMGI-3, weakly-altered MGI QMD (3184 m elevation); INF-11, moderately-altered MGI QMD (3215 m elevation); GRD-03, pervasively-altered DIC diorite (3032 m elevation).

Sample	FrESKD-1	FrMGI-3				INF-11			
Grain	A	B	C	D	E	F ※		G ※	
Occurrence	Ig	Ig	Ig	Ig	Ig	Ig	H-B	Ig	H-B
n	3	10	9	9	10	5	8	5	7
SiO_2	37.04	37.97	38.07	37.73	37.67	37.55	39.03	38.9	39.62
TiO_2	4.39	4.6	4.35	4.56	4.48	4.33	3.69	4.1	3.47
Al_2O_3	13.48	13.66	13.42	13.66	13.5	13.53	12.55	12.88	12.4
FeO	18.34	16.29	16.25	16.46	16.13	15.38	14.13	14.32	13.95
MnO	0.41	0.22	0.18	0.2	0.18	0.15	0.15	0.14	0.13
MgO	13.85	15.11	15.21	14.98	15.03	15.49	16.91	16.33	17.04
CaO	0.04	0.01	0.06	0	0.03	0.01	0.01	0.02	0.06
Na_2O	0.22	0.28	0.21	0.25	0.27	0.24	0.14	0.15	0.12
K_2O	9.03	9.39	9.13	9.4	9.14	9.22	9.17	9.23	8.94
Cl	0	0.23	0.24	0.25	0.24	0.19	0.19	0.18	0.18
F	0.15	0	0.01	0	0	0.09	0.24	0.21	0.24
O=F,Cl	0.06	0.05	0.06	0.06	0.06	0.08	0.15	0.13	0.14
Total	96.89	97.71	97.06	97.44	96.62	96.09	96.06	96.33	96.01
Si	5.55	5.58	5.62	5.57	5.6	5.59	5.76	5.74	5.83
Al^{IV}	2.38	2.37	2.34	2.38	2.36	2.37	2.19	2.24	2.15
Al^{VI}	0	0	0	0	0	0	0	0	0
Ti	0.49	0.51	0.48	0.51	0.5	0.49	0.41	0.45	0.38
Fe	2.3	2	2.01	2.03	2	1.92	1.75	1.77	1.72
Mn	0.05	0.03	0.02	0.02	0.02	0.02	0.02	0.02	0.02
Mg	3.09	3.31	3.35	3.3	3.33	3.44	3.72	3.59	3.74
Ca	0.01	0	0.01	0	0.01	0	0	0	0.01
Na	0.06	0.08	0.06	0.07	0.08	0.07	0.04	0.04	0.03
K	1.73	1.76	1.72	1.77	1.73	1.75	1.73	1.74	1.68
Cl	0	0.06	0.06	0.06	0.06	0.05	0.05	0.05	0.04
F	0.07	0	0	0	0	0.04	0.11	0.1	0.11
Mg#	0.57	0.62	0.63	0.62	0.62	0.64	0.68	0.67	0.69
Al^{tot}	2.38	2.37	2.34	2.38	2.36	2.37	2.19	2.24	2.15

Table 5. Continued.

Sample	INF-11		GRD-03					
Grain	H ※		I	J	K	L	M	N
Occurrence	Ig	H-B	H-V	H-V	H-P	H-P	H-V	H-P
n	5	7	15	21	21	20	14	13
SiO_2	37.72	38.11	40.07	40.12	39.98	39.01	40.25	40.36
TiO_2	4.03	3.82	2.76	2.8	2.69	2.6	2.77	2.84
Al_2O_3	13.31	13.16	12.52	12.29	12.64	12.79	12.1	12.19
FeO	14.79	14.69	13.3	13.11	13.07	13.75	12.86	12.98
MnO	0.13	0.15	0.11	0.12	0.13	0.14	0.13	0.13
MgO	15.88	16.3	18.05	18.26	17.78	17.99	18.11	17.95
CaO	0.01	0.01	0.12	0.04	0.12	0.08	0.1	0.1
Na_2O	0.22	0.16	0.13	0.13	0.12	0.11	0.16	0.15
K_2O	9.45	9.42	8.86	9.2	8.86	8.62	8.81	8.98
Cl	0.2	0.2	0.2	0.19	0.19	0.19	0.19	0.19
F	0.12	0.16	0.43	0.41	0.38	0.29	0.49	0.48
O=F,Cl	0.09	0.11	0.23	0.21	0.2	0.17	0.25	0.25
Total	95.75	96.07	96.32	96.46	95.75	95.4	95.73	96.12
Si	5.63	5.66	5.86	5.86	5.87	5.77	5.91	5.91
Al^{IV}	2.34	2.3	2.14	2.12	2.13	2.23	2.09	2.09
Al^{VI}	0	0	0.02	0	0.06	0	0.01	0.01
Ti	0.45	0.43	0.3	0.31	0.3	0.29	0.31	0.31
Fe	1.85	1.82	1.63	1.6	1.61	1.7	1.58	1.59
Mn	0.02	0.02	0.01	0.02	0.02	0.02	0.02	0.02
Mg	3.53	3.61	3.93	3.98	3.89	3.97	3.96	3.92
Ca	0	0	0.02	0.01	0.02	0.01	0.02	0.02
Na	0.06	0.05	0.04	0.04	0.03	0.03	0.05	0.04
K	1.8	1.78	1.65	1.71	1.66	1.63	1.65	1.68
Cl	0.05	0.05	0.05	0.05	0.05	0.05	0.05	0.05
F	0.06	0.08	0.2	0.19	0.17	0.14	0.23	0.22
Mg#	0.66	0.66	0.71	0.71	0.71	0.7	0.72	0.71
Al^{tot}	2.34	2.3	2.16	2.12	2.19	2.23	2.1	2.1

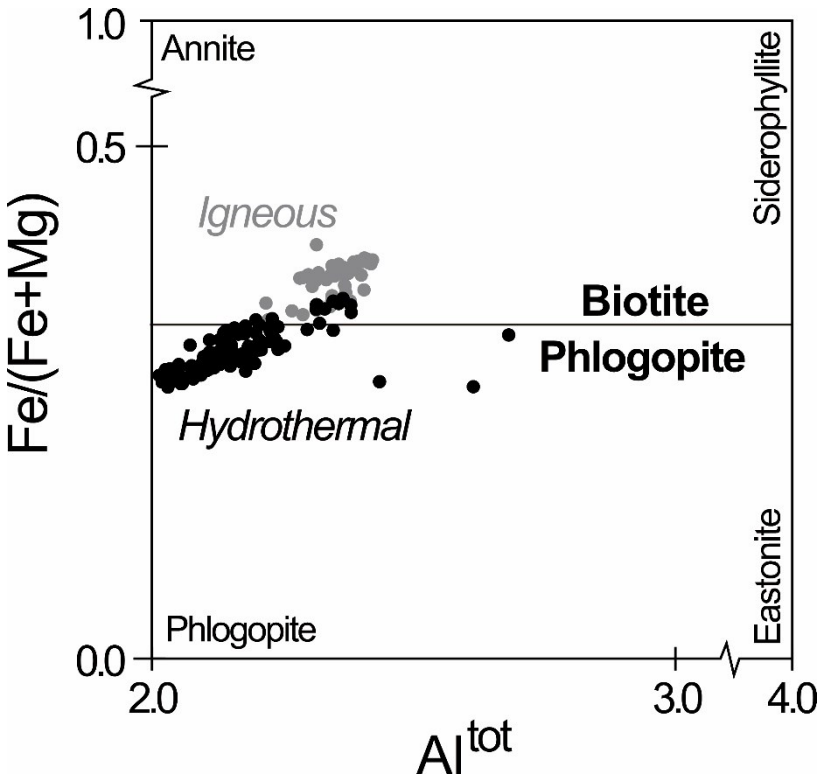

Figure 27. Composition of hydrothermal and igneous biotite crystals from the DIC diorite and MGI QMD expressed in the Fe/(Fe+Mg) versus Al^{tot} diagram. Most hydrothermal biotite crystals, including those replacing igneous amphibole and biotite minerals, have chemical compositions more enriched in phlogopite component than igneous biotite crystals.

4.2.2. Hydrothermal anhydrite and magnetite abundance in relation to Cu grade

To study the relationship between hydrothermal anhydrite and magnetite with Cu grade the abundance of these minerals was estimated both visually and in thin section. Magnetite estimation was supported by magnetic susceptibility measurements, since little to no relict igneous magnetite occurs within GIC altered units. Between 3600 and 2600 m elevation hydrothermal magnetite content correlates negatively with anhydrite (Fig. 28). Magnetic susceptibility measurements are highest (>100 × 10^{-3} SI) at 3300~3360 m elevation, where the DIC diorite contains >15 vol.% magnetite and 1~3% Cu. In the upper part of drill hole GRD39-01 at 2900~3040 m elevation, the highest Cu values (2~4% Cu) are associated with magnetic susceptibilities ranging from 10 to 100 × 10^{-3} SI, which corresponds to 2~15 vol.% magnetite from visual estimates. In the middle part of hole GRD39-01, the DIC diorite contains no magnetite but has grades of ≤2% Cu due to sericite alteration that overprints the potassic alteration and has removed its hydrothermal magnetite.

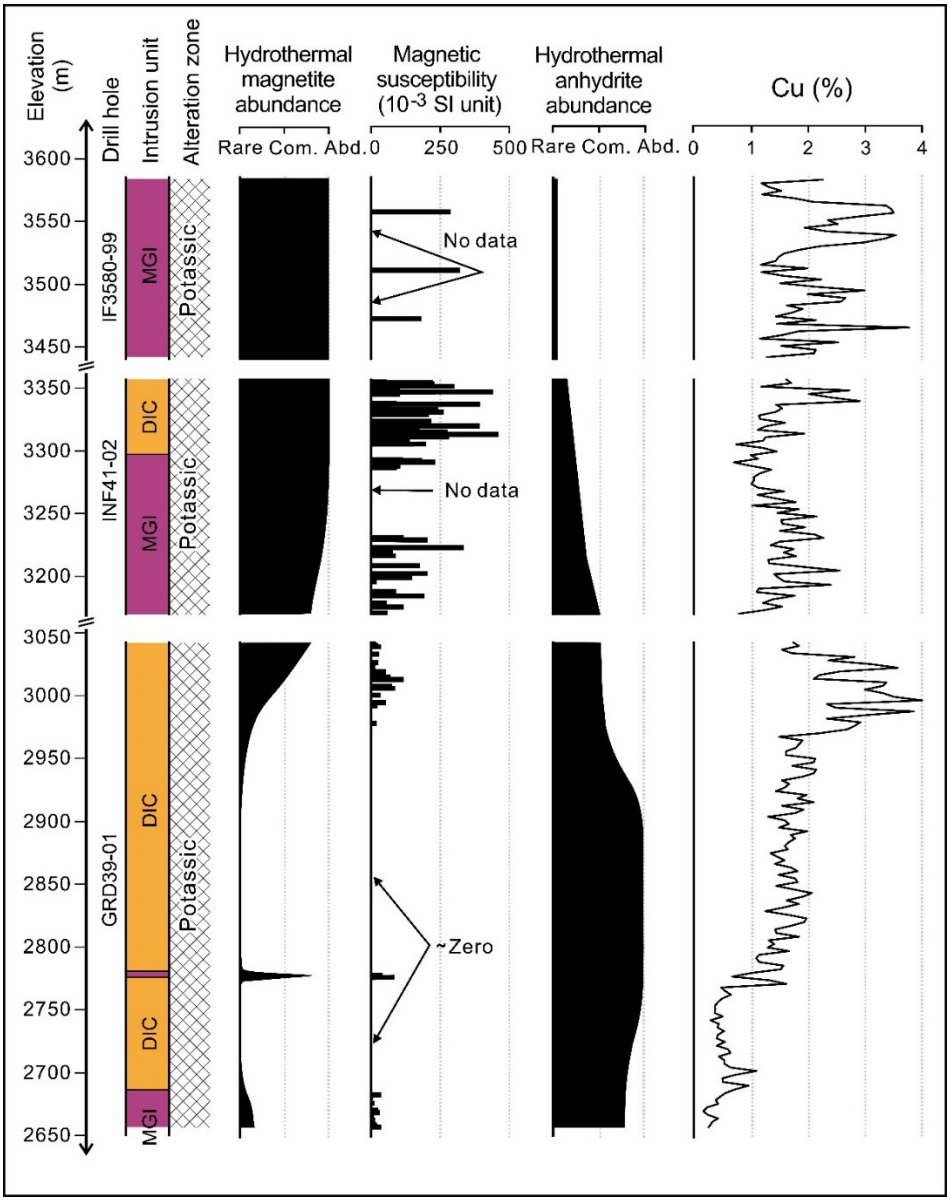

Figure 28. Relationships among rock unit, alteration, hydrothermal magnetite abundance, magnetic susceptibility, hydrothermal anhydrite abundance, and Cu concentration. Potassic alteration zone contains centimeter scale sericite alteration of ~1 vol.%. Copper mineralization has a positive correlation with the abundance of hydrothermal magnetite and magnetite susceptibility, which is in inverse proportion to the abundance of hydrothermal anhydrite. Abbreviations: Com., common; Abd., abundant.

4.2.3. Sulfur isotope ratios and temperature estimates

The sulfur isotope ratio of sulfur-bearing minerals in sixty altered and one unaltered igneous samples was measured (Table 6, Fig. 29). Sulfur-bearing minerals analyzed include those contained in a) comb quartz veins with chalcopyrite centerlines, b) anhydrite-chalcopyrite veins, c) chalcopyrite veins with sericite selvages and d) anhydrite-bearing pyrite-chalcopyrite-quartz veins with sericite selvages.

The $\delta^{34}S$ values of anhydrite are invariably higher than those of coexisting sulfides. The ranges of $\delta^{34}S$ values of sulfur-bearing minerals hosted in the anhydrite-chalcopyrite veins are 1.2–4.2‰ for chalcopyrite (n=24; avg. 2.3‰), 1.1 and 2.1‰ for bornite (n=2) and 10.5–13.8‰ for anhydrite (n=26; avg. 12.2‰). Two chalcopyrite samples that occur along the centerlines of comb-textured quartz veins have $\delta^{34}S$ values of 2.4 and 2.5‰ (n=2). One chalcopyrite vein that is accompanied by sericite alteration has $\delta^{34}S$ = 2.1‰. The $\delta^{34}S$ values for pyrite in a veinlet with sericite selvage are 2.8 to 4.8‰ (n=3; avg. 3.7‰), and those of anhydrite are 14.6–15.2‰ (n=2). A sample of the syn-mineralization ESKD MD yields a $\delta^{34}S$ of 9.4‰.

The $\delta^{34}S$ values of chalcopyrite in comb quartz veins and anhydrite-chalcopyrite veins are similar, whereas pyrite from pyrite-chalcopyrite-quartz veins with sericite selvages has higher average $\delta^{34}S$ than chalcopyrite in anhydrite-chalcopyrite veins. Likewise, anhydrite from pyrite-chalcopyrite-quartz veins with sericite selvages has a heavier isotopic composition than anhydrite in anhydrite-chalcopyrite veins.

Assuming equilibrium and using fractionation calculations from Ohmoto and Rye (1979) and Ohmoto and Lasaga (1982), the Δ values of coexisting sulfate and

sulfide minerals in anhydrite-chalcopyrite-bearing veins within high-grade (1–4% Cu) core intervals indicate temperatures of 645–475 °C (Fig. 29). By contrast, temperatures

Table 6. Sulfur isotope data sorted by elevation.

No	Sample	Elev. (m)	Vein mineralogy/rock sample	$\delta^{34}S$ (‰)				
				Anh	Ccp	Py	Bn	Bulk
1	IF-1	3549.2	Qz-Bt + Ccp-Bn centerline		2.5			
2	IF-2	3509.8	Qz-Bt + Ccp-Bn centerline		2.4			
3	IF-3	3462.5	Anh-Qz-Ccp-Bn	11.9	2.6			
4	INF-28	3317.4	Anh-Qz-Ccp	12.3	3.2			
5	INF-27	3313.5	Anh-Qz-Ccp	12.4	2.7			
6	INF-18	3275.4	Py-Ccp-Anh-Qz + Ser selvages	14.6		2.8		
7	INF-16	3272.5	Py-Ccp-Anh-Qz + Ser selvages	15.2		3.6		
8	INF-12	3216.5	Anh-Qz-Ccp	11.2	2.9			
9	INF-9	3206.0	Anh-Qz-Ccp-Bt	13.3	2.6			
10	INF-6	3194.2	Anh-Ccp	11.8	3.3			
11	INF-4	3180.3	Anh-Ccp	12.3	2.5			
12	GOP-1	3100.0	Anh-Qz-Ccp-Bn	12.6	2.0		2.1	
13	GRD-12	3007.3	Bt-Anh-Qz-Ccp-Bn	12.2	2.1			
14	GRD-15	2996.8	Anh-Qz-Ccp-Bn	12.1	2.9			
15	GRD-20	2981.4	Anh-Qz-Ccp-	11.0	2.4			
16	GRD-21	2975.8	Ccp + Ser selvages		2.1			
17	GRD-27	2917.1	Anh-Qz-Ccp-Mol	13.0				
18	GRD-30	2911.2	Anh-Qz-Ccp-Bn	10.5	2.1			
19	GRD-33	2898.9	Anh-Qz-Ccp	13.6	2.3			
20	GRD-35	2887.0	Anh-Ccp	13.2	2.7			
21	GRD-36	2885.3	Anh-Qz-Ccp	12.9	2.5			
22	GRD-40	2861.2	Anh-Qz-Ccp	12.9	1.5			
23	GRD-45	2838.2	Anh-Qz-Ccp-Mol	13.8	1.6			
24	GRD-50	2807.8	Anh-Qz-Ccp	11.7	2.1			
25	GRD-53	2794.2	Anh-Qz-Ccp-Bn	11.0			1.1	
26	GRD-55	2780.4	Anh-Qz-Ccp-Bn	12.9	4.2			
27	GRD-60	2750.3	Py-Qz + Ser selvages			4.8		
28	GRD-63	2738.8	Anh-Qz-Ccp	11.8	1.3			
29	GRD-66	2720.9	Anh-Qz-Ccp	12.8	1.2			
30	GRD-71	2700.9	Anh-Qz-Ccp-Bn-Bt	11.3	1.3			
31	GRD-77	2684.2	Anh-Ccp	11.8	2.4			
32	GRD-78	2679.5	Anh-Ccp	11.3	1.3			
33	FrESKD-2	1703.0	Monzodiorite (ESKD)					9.4

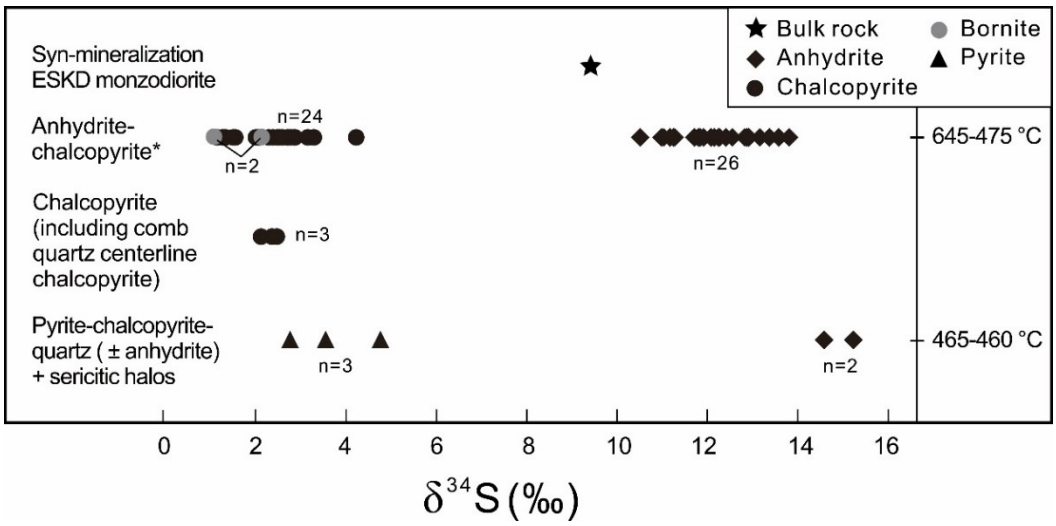

Figure 29. The $\delta^{34}S$ values projected for magmatic and hydrothermal stages. (*) Some anhydrite-chalcopyrite veins are interpreted to be formed at the earliest stage of potassic alteration.

estimated with sulfate-sulfide pairs from anhydrite-bearing pyrite-chalcopyrite-quartz veins with sericite selvages indicate formation temperatures of 465–460 °C. This matches observations from many other porphyry deposits whose potassic alteration is believed to be the product of high-temperature hydrothermal fluids that cool as they ascend and radiate outwards, forming a sericite alteration halo around a core of potassic alteration (Seedorff et al., 2005).

4.3. Discussion

4.3.1. High-temperature SO_2 disproportionation

Sulfur dioxide is the principal sulfur species in gases evolved from GIC magmas in which SO_4^{2-} greatly exceeds H_2S (Henley et al., 2015; Mavrogenes and Blundy, 2017; Henley and Seward, 2018; Mernagh et al., 2020). The decrease in SO_2/H_2S during hydrothermal processes may be related to disproportionation of magmatic SO_2 (Whitney, 1988; Holland, 1965; Kusakabe et al., 2000):

$$4SO_{2(g)} + 4H_2O_{(aq)} \rightarrow H_2S_{(aq)} + 3H_2SO_{4(aq)} \quad (2)$$

This reaction occurs progressively as magmatic-hydrothermal fluids cool below 400–350 °C (Holland, 1965; Henley and McNabb, 1978; Kusakabe et al., 2000). However, my sulfur isotope data indicate that coexisting sulfate and sulfide minerals formed at temperatures of 645 to 460 °C.

Alternatively, the decrease in SO_4^{2-}/H_2S (e.g., Ertsberg skarn system; Gibbins, 2006) within hydrothermal fluids may be due to addition of H_2S degassed from mafic magma at depth (Ohmoto and Rye, 1979) and/or by the leaching and

reprecipitation of sulfides (Ohmoto and Goldhaber, 1997). Another mechanism for the evolution from oxidized sulfur-dominant (S^{6+} and/or S^{4+}) to reduced sulfur-dominant (S^{2-}) fluid is by reaction between the hydrothermal fluid and igneous wallrocks (Carmichael and Ghiorso, 1986; Rye, 1993; Ohmoto and Goldhaber, 1997; Liang et al., 2009; Henley et al., 2015; Mavrogenes and Blundy, 2017; Henley and Seward, 2018).

Recent studies provide evidence for SO_2 disproportionation at high temperature and pressure by reaction with high-anorthite plagioclase within igneous wallrocks (Henley et al., 2015; Mavrogenes and Blundy, 2017; Watanabe et al., 2018; Henley and Seward, 2018). This process may be written synoptically as follows (Henley and Seward, 2018):

$$3CaAl_2Si_2O_8 + 4SO_{2(g)} + 22H_2O_{(g)} \rightarrow$$
$$3CaSO_4 + 6Al(OH)_{3(g)} + 6H_4SiO_{(g)} + 3SiO_2 + H_2S \quad (3)$$

Although my microscopic observations found no clear evidence for the conversion of plagioclase to anhydrite ± andalusite ± sulfide minerals or the growth of anhydrite on the surfaces of plagioclase crystals, hydrothermal andalusite has been observed in DIC and MGI rocks (Paterson and Cloos, 2005) and other alteration minerals such as biotite, muscovite or K-feldspar are ubiquitous in the GIC. These alteration minerals may incorporate Al and Si generated by Reaction (3) if they react with alkalis, iron and magnesium (Henley and Seward, 2018), and andalusite that accommodates Al from Reaction (3) may have been altered to diaspore and pyrophyllite during retrograde cooling and hydrolysis (Henley and Seward, 2018).

Sulfur isotopes from anhydrite and sulfide minerals formed at >620 °C show a significant increase in their $\delta^{34}S$ ratios (Fig. 30), that may be due to enrichment of ^{34}S in the SO_4^{2-}- and H_2S-bearing liquid (Field et al., 2005) after unmixing of a single-phase magmatic SO_2 gas into liquid and vapor. Hereafter, I assume that SO_2 gas was the main sulfur species exsolved from GIC magmas (Henley et al., 2015; Mavrogenes and Blundy, 2017; Henley and Seward, 2018; Mernagh et al., 2020). When SO_2 disproportionates, H_2S is partitioned as both aqueous and gaseous species into the liquid and low-density vapor, respectively, whereas SO_4^{2-} remains in the liquid as an aqueous species since the concentration of H_2SO_4 gas is negligible. Although the partition coefficient for H_2S between liquid and vapor is unknown, removal of the H_2S-bearing vapor would cause the remaining liquid to become enriched in ^{34}S because H_2S is depleted in ^{34}S relative to SO_4^{2-}.

Plots of $\delta^{34}S$ values for associated sulfate and sulfide minerals versus the Δ values of the mineral pairs provide an estimation of the molar proportion of SO_4^{2-}/H_2S (Field and Gustafson, 1976; Kusakabe et al., 1984; Imai, 2000; Field et al., 2005; Hedenquist et al., 2017). The suites of coexisting sulfate-sulfide mineral pairs in anhydrite-chalcopyrite veins suggest that in the temperature range of 645 to 475 °C, the bulk sulfur isotope composition ($\delta^{34}S_{\Sigma S}$) was 6.4‰ and the SO_4^{2-}/H_2S molar proportion was ~2:3 (XSO_4^{2-}=0.42; XH_2S=0.58), assuming that their proportion remained constant as temperature decreased (Fig. 30A). These results are not consistent with Reaction (3), from which a molar SO_4^{2-}/H_2S of 3:1 is predicted, and the calculated $\delta^{34}S_{\Sigma S}$ of 6.4‰ is also much lower than the 9.4‰ observed in syn-mineralization ESKD MD.

An alternative interpretation is that the proportion of SO_4^{2-}/H_2S was not constant during cooling of hydrothermal fluids, as indicated by the sulfur isotope data that vary with temperature. Above 550 °C the SO_4^{2-}/H_2S was ~4:1 (XSO_4^{2-} =0.83; XH_2S=0.17) (Fig. 30B) and more reduced at 1:1 below 550 °C (Fig. 30C). The ~4:1 proportion of SO_4^{2-}/H_2S is slightly higher than the expected value of 3:1, perhaps indicating removal of H_2S within magmatic vapor. Sulfur isotope results at >550 °C show values of $\delta^{34}S_{\Sigma S}$=10.2‰, which, although reasonable, are much higher than the expected value of ~7‰ for an oxidized magma (e.g., Ohmoto and Rye, 1979). The elevated $\delta^{34}S_{\Sigma S}$ could be due to incorporation of wallrock sulfate-bearing sediments into the magma (e.g., Butte district, Montana: Field et al., 2005; Ertsberg skarn system: Gibbins, 2006). A potential source of evaporite exists in the New Guinea Limestone Group, in which anhydrite nodules have $\delta^{34}S$ values between 20 and 22‰ (Claypool et al., 1980).

Reaction (3) ideally yields SO_4^{2-} and H_2S in the molar proportion of 3:1 (XSO_4^{2-} =0.75; XH_2S=0.25). Assuming that the SO_4^{2-} and H_2S formed by such a reaction are subsequently incorporated into anhydrite and sulfides formed at >550 °C, I can obtain the $\delta^{34}S_{\Sigma S}$ from:

$$\delta^{34}S_{\Sigma S} = 0.75(\delta^{34}S_{sulfates}) + 0.25(\delta^{34}S_{sulfides}) \quad (4)$$

by substituting the mean $\delta^{34}S$ values for anhydrite and sulfide minerals (Field et al., 2005). The result of this calculation gives a $\delta^{34}S_{\Sigma S}$ of 9.4‰ that equals the measured $\delta^{34}S$ value of syn-mineralization ESKD MD, suggesting that this intrusion directly represents the $\delta^{34}S_{\Sigma S}$ of the system.

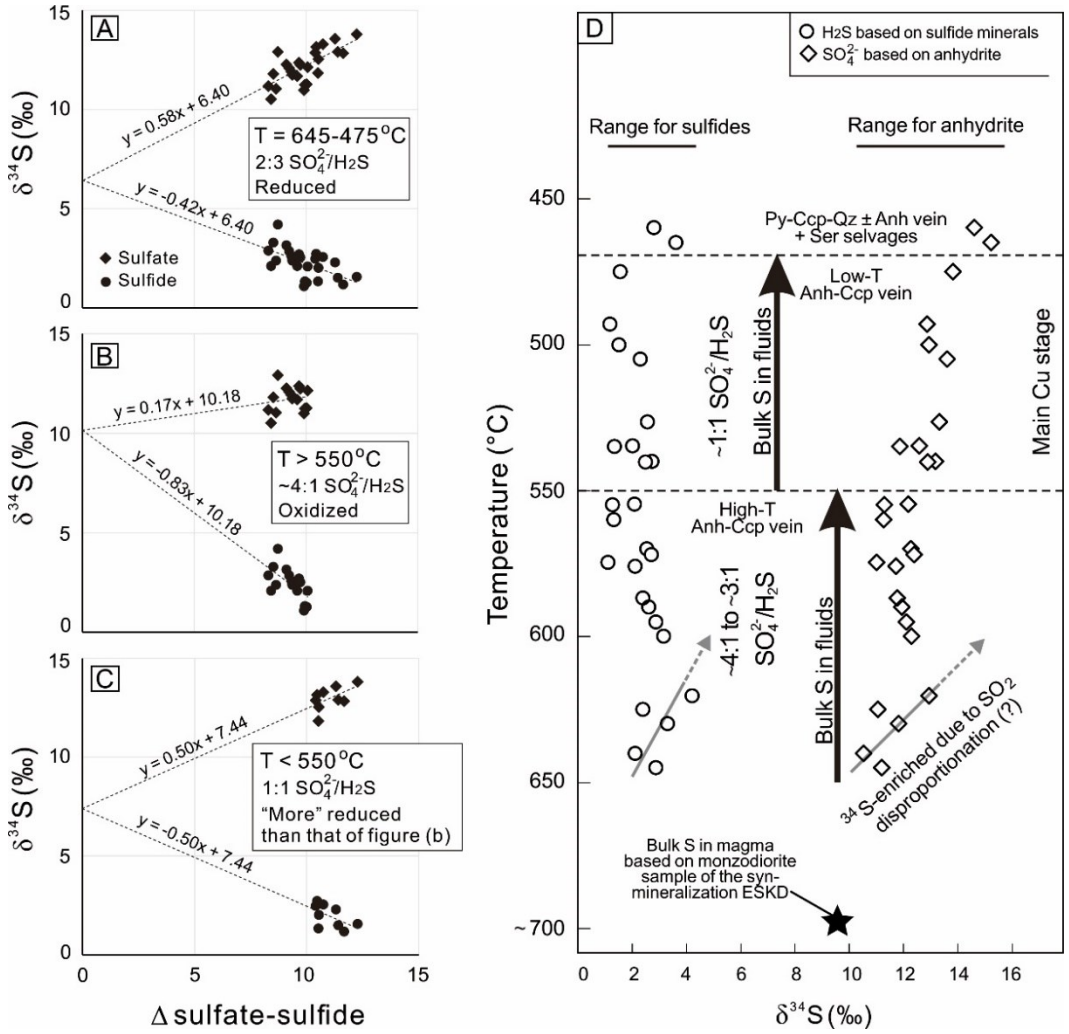

Figure 30. (A) Plot of $\delta^{34}S$ values for associated sulfate and sulfides of veins vs. the Δ value of the pair. Assuming a constant proportion of SO_4^{2-}/H_2S, the convergence and slopes of the two regression lines offer an approximation of the bulk sulfur isotope composition ($\delta^{34}S_{\Sigma S}$) ≈ 6.4‰ and the proportion of oxidized to reduced sulfur (~2:3 SO_4^{2-}/H_2S) in the hydrothermal system. (B) Assuming that the proportion of SO_4^{2-}/H_2S was not constant, the SO_4^{2-}/H_2S proportion was ~4:1 at >550 °C, with $\delta^{34}S_{\Sigma S}$ ≈ 10.2‰. (C) The SO_4^{2-}/H_2S proportion was 1:1 at <550 °C, with $\delta^{34}S_{\Sigma S}$ ≈ 7.4‰. (D) Evolution of the oxidation state of hydrothermal fluids based on sulfur isotope as a function of temperature. The fluid at >550 °C record the SO_4^{2-} and H_2S end-products of SO_2 disproportionation which yields SO_4^{2-} and H_2S in the molar proportion of ~4:1 to ~3:1, and $\delta^{34}S_{\Sigma S}$ of ~9.4‰. The decreases in $\delta^{34}S_{\Sigma S}$ and SO_4^{2-}/H_2S proportion are interpreted to be due to early anhydrite precipitation and reduction of SO_4^{2-} to H_2S via a coupled oxidation of Fe^{2+} to Fe^{3+} (see text).

4.3.2. Reduction of SO_2-derived aqueous sulfate

Hydrothermal anhydrite with a negligible amount of sulfide minerals is observed in the earliest K-feldspar and biotite alteration (Figs. 26A, B). Because SO_4^{2-} is enriched in ^{34}S relative to the $\delta^{34}S_{\Sigma S}$ of SO_4^{2-}-bearing liquid, the precipitation of anhydrite removes ^{34}S-enriched SO_4^{2-} so that the remaining liquid becomes depleted in ^{34}S, assuming that aqueous SO_4^{2-} and H_2S in liquid contributed sulfur to the precipitation of anhydrite ± sulfide vein/alteration. The ~3:1 proportion of SO_4^{2-}/H_2S at >550 °C indicates a high activity of SO_4^{2-} in high-temperature magmatic-hydrothermal fluids (Brimhall et al., 1985; Liang et al., 2009). The SO_4^{2-}/H_2S proportion was not constant during cooling of fluids as described above, such that SO_4^{2-}/H_2S became more reduced (1:1) at <550 °C.

My observations suggest that Grasberg potassic alteration evolved through several alteration and vein stages (Fig. 26) from initial anhydrite-bearing K-feldspar and biotite alteration (Henley and Seward, 2018), followed by magnetite, biotite, quartz and anhydrite-chalcopyrite veining (Pollard and Taylor, 2002). Early K-feldspar and biotite alteration is frequently associated with hydrothermal magnetite that replaces igneous mafic minerals (Figs. 26C, D). Magnetite veins (Figs. 26E, F) formed during the mid-stage of potassic alteration, whereas end-stage potassic alteration formed anhydrite-chalcopyrite and chalcopyrite veins (Figs. 26G–J). Hydrothermal magnetite is interpreted to have formed coincident with the reduction of SO_4^{2-} during the potassic episode. This process is consistent with drill core analysis, in which Cu mineralization has a positive correlation with the abundance of hydrothermal magnetite, which is inversely correlated with the abundance of

hydrothermal anhydrite (Fig. 28). I infer that in addition to early anhydrite precipitation, Fe in igneous wall rocks could have reduced SO_4^{2-} to H_2S via a coupled oxidation of Fe^{2+} to Fe^{3+} (Carmichael and Ghiorso, 1986; Sun et al., 2004; Liang et al., 2009) and thus decreased the XSO_4^{2-} in the hydrothermal fluid.

The earliest K-feldspar and associated magnetite replace biotite phenocrysts, where magnetite formation was likely due to oxidation of Fe^{2+} in biotite by aqueous SO_4^{2-}. The process is believed to have followed the reaction path predicted by Liang et al. (2009):

$$8KFe_3AlSi_3O_{10}(OH)_2 + 2H_2SO_{4(aq)} \rightarrow 8KAlSi_3O_8 + 8Fe_3O_4 + 8H_2O + 2H_2S \quad (5)$$

Replacement of igneous amphibole and biotite by hydrothermal biotite is observed in many porphyry deposits around the world (Bingham, Utah: Moore and Czamanske, 1973; Santa Rita, New Mexico: Jacobs and Parry, 1979; Casino, Canada: Selby and Nesbitt, 2000). Brimhall et al. (1985) also report replacement of edenite (amphibole endmember) by an anhydrite-bearing alteration assemblage:

$$NaCa_2Mg_5(AlSi_7O_{22})(OH)_2 + 0.5K_2SO_{4(aq)} + 4H_2SO_{4(aq)} \rightarrow$$
$$KMg_3(AlSi_3O_{10})(OH)_2 + 4SiO_2 + 2CaSO_4$$
$$+ 0.5Na_2SO_{4(aq)} + 2\,MgSO_{4(aq)} + 4H_2O \quad (6)$$

This reaction applies to early alteration produced by SO_4^{2-}-bearing hydrothermal fluid, but note that there is no magnetite precipitation and sulfur remains as sulfate. Most amphibole phenocrysts in the DIC diorite and MGI QMD have been replaced by biotite (Fig. 26 C), and biotite phenocrysts have re-equilibrated into hydrothermal biotite with lower Fe content (Figs. 26D, 27). Hydrothermal biotite is

commonly associated with hydrothermal magnetite, indicating that Fe^{2+} was liberated and oxidized to form magnetite, resulting in the reduction of sulfur (Carmichael and Ghiorso, 1986; Sun et al., 2004; Liang et al., 2009):

$$12FeO_{(rock)} + SO_4^{2-} + 2H^+ \rightarrow 4Fe_3O_4 + H_2S \quad (7)$$

The role of this reaction in Grasberg porphyry Cu mineralization is illustrated in Figure 31 that explains the increase in hydrothermal fluid H_2S concentration required to precipitate the abundant Cu sulfides (Kouzmanov and Pokrovski, 2012). The Grasberg-related system contains 52.5 Mt of Cu (7.5 Gt of ore at 0.7% Cu) with Cu primarily contained in chalcopyrite ($CuFeS_2$) and bornite (Cu_5FeS_4) with a relative abundance of 75% and 25%, respectively (Leys et al., 2012). Thus, approximately 45 Mt of S^{2-} is required to precipitate 52.5 Mt of Cu. According to Reaction (7), the formation of approximately 1.3 Gt of hydrothermal magnetite could have reduced approximately 45 Mt of S^{2-}. The total amount of hydrothermal magnetite of 1.9 Gt in the Grasberg deposit (internal report by PT Freeport Indonesia) is more than enough to generate the observed 52.5 Mt of Cu. Therefore, not all S^{2-} was incorporated in Cu minerals, some formed pyrite as veins, disseminations or as massive bodies at the GIC periphery such as the heavy sulfide zone and the rest was outgassed.

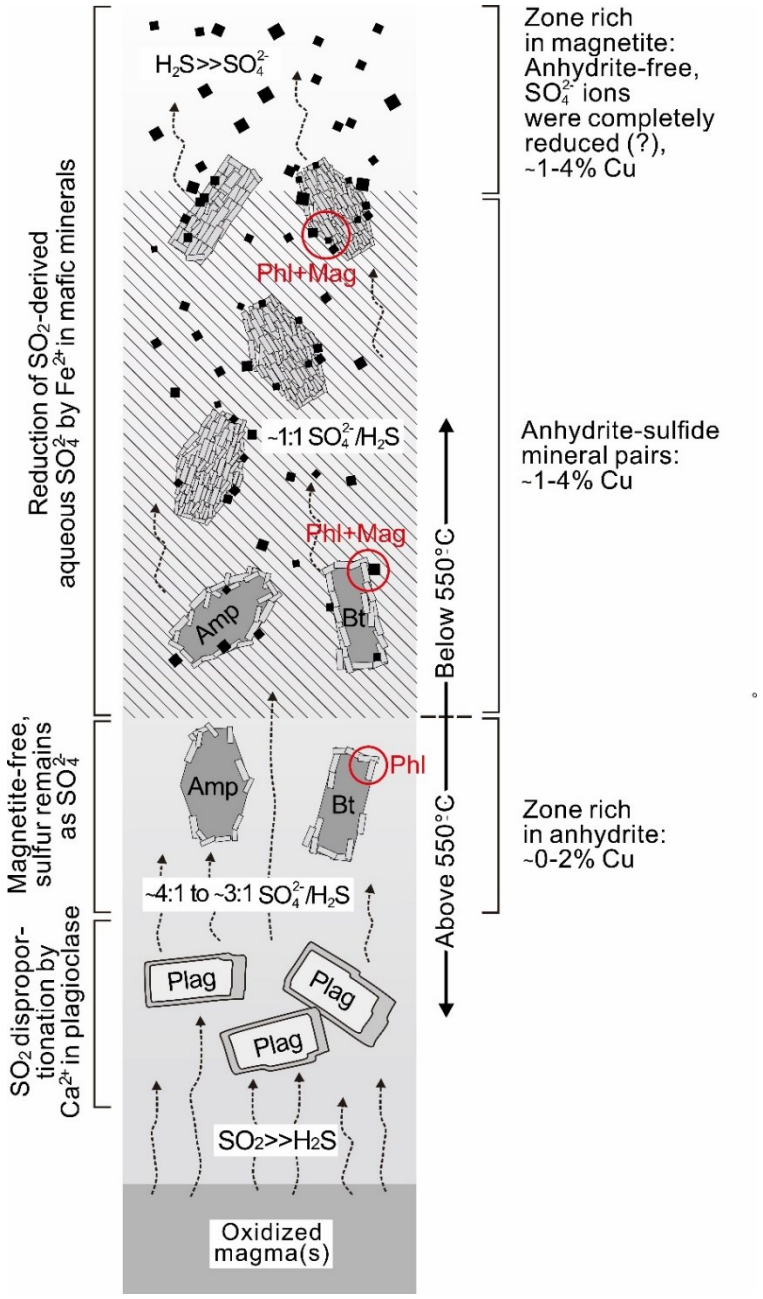

Figure 31. Schematic model showing the evolutions of sulfur species and oxidation state of hydrothermal fluid at Grasberg with respect to mineral assemblage and Cu mineralization. The ~4:1 to ~3:1 proportion of SO_4^{2-}/H_2S produced by SO_2 disproportionation is associated with magnetite-free, anhydrite-rich zone with ~0–2% Cu. Higher concentration of Cu (~1–4% Cu) in the magnetite-bearing zone indicate that mineralization is related to the increase in H_2S by the reduction of aqueous SO_4^{2-} (see text).

Chapter 5: Conclusion

The combined physical and chemical indicate that magmatic degassing of Cl occurs following the crystallization of phenocryst in the upper crust, whereas the partitioning of S from magma into fluids requires another process that occurs at higher pressure and temperature (e.g., at ~800 °C and ~2 kbar). Mixing of magmas of two distinct oxidation states could have generated SO_2 by the reduction of sulfate via oxidation of Fe^{2+}, where in the case of Grasberg, the MGI upper-crustal magma provided sulfate (e.g., as anhydrite), and large amounts of Fe^{2+} were derived from the injected, deep-sourced reduced magma. Anhydrite melt as a source for sulfur has been recently proposed by numerous authors (e.g., Chambefort et al., 2008; Dilles et al., 2015; Hutchinson and Dilles, 2019). Magmatic degassing of volatiles that occurred intermittently at Grasberg implies that localized accumulation is required for an efficient hydrothermal system. Ore-forming fluids may be accumulated and stored in a stable fluid pocket beneath the cupola zone before a sudden discharge (Cloos, 2001; Richards, 2018). Such a short-lived fluid discharge is in agreement with the fact that most porphyry deposits occur in a short period of time compared to their associated magmatic systems (von Quadt et al., 2011; Chiaradia et al., 2013; Large et al., 2018).

Just after the discharge, S is not ready for economic mineralization due to its unsuitable valences (SO_2>>H_2S). Phase separation of magmatic SO_2 into liquid (aqueous SO_4^{2-} and H_2S) and vapor (gaseous H_2S) led to the enrichment in the ^{34}S of SO_4^{2-}- and H_2S-bearing liquid, as indicated by sulfur isotope data. The high proportion of SO_4^{2-}/H_2S derived from SO_2 gas (e.g., ~4:1 to ~3:1 at Grasberg) is

interpreted to have further decreased due not only to early anhydrite precipitation but additionally by the reduction of aqueous SO_4^{2-} to H_2S via a coupled oxidation of Fe^{2+} in igneous wallrocks and/or fluids to Fe^{3+}. At Grasberg, SO_4^{2-}-rock interaction is suggested by the replacement of amphibole by hydrothermal biotite and of igneous biotite by phlogopitic hydrothermal biotite. Fe^{2+} was liberated from igneous amphibole and biotite and oxidized to form magnetite. The S^{2-} reacted with Cu in hydrothermal fluids to precipitate the abundant Grasberg Cu sulfide mineralization. The frequent association of Cu sulfides with hydrothermal magnetite in porphyry systems suggests that this may be a common process in such deposits.

References

Anderson, J.L., 1996, Status of thermobarometry in granitic batholiths: Geo-logical Society of America Special Paper, v. 315, p. 125–138.

Ballard, J.R., Palin, J.M., and Campbell, I.H., 2002, Relative oxidation states of magmas inferred from Ce(IV)/Ce(III) in zircon: Application to porphyry copper deposits of northern Chile: Contributions to Mineralogy and Petrology, v. 144, p. 347–364.

Blundy, J., and Wood, B., 1994, Prediction of crystal-melt partition coefficients from elastic moduli: Nature, v. 372, p. 452–454.

Brimhall, G.H., Agee, C., and Stoffregen, R., 1985, The hydrothermal conversion of hornblende to biotite: Canadian Mineralogist, v. 23, p. 369–379.

Burnham, C.W., 1979, Magmas and hydrothermal fluids, in Barnes, H.L., ed., Geochemistry of hydrothermal ore deposits, 2nd edition: New York, John Wiley and Sons, p. 71–136.

Candela, P.A., and Holland, H.D., 1984, The partitioning of copper and molybdenum between silicate melts and aqueous fluids: Geochimica et Cosmochimica Acta, v. 48, p. 373–380.

Carmichael, I.S.E., and Ghiorso, M.S., 1986, Oxidation-reduced relations in basic magma: A case for homogenous equilibria: Earth and Planetary Science Letters, v. 78, p. 200–210.

Carroll, M.R., and Rutherford, M.J., 1985, Sulfide and sulfate saturation in hydrous silicate melts: Proceedings of the Fifteenth Lunar and Planetary Science Conference Part 2. Journal of Geophysical Research, v. 90, p. C601–C612.

Carroll, M.R., and Rutherford, M.J., 1988, Sulfur speciation in hydrous experimental glasses of varying oxidation state: Results from measured wavelength shifts of sulfur X-rays: American Mineralogist, v. 73, p. 845–849.

Chambefort, I., Dilles, J.H., and Kent, A.J.R., 2008, Anhydrite-bearing andesite and dacite as a source for sulfur in magmatic-hydrothermal mineral deposits: Geology, v. 36, p. 719−722.

Chambefort, I., Dilles, J.H., and Longo, A.A., 2013, Amphibole geochemistry of the Yanacocha Volcanics, Peru: Evidence for diverse sources of magmatic volatiles related to gold ores: Journal of Petrology, v. 54, p. 1017−1046.

Chelle-Michou, C., Chiaradia, M., Ovtcharova, M., Ulianov, A., and Wot-zlaw, J.-F., 2014, Zircon petrochronology reveals the temporal link between porphyry systems and the magmatic evolution of their hidden plutonic roots (the Eocene Coroccohuayco deposit, Peru): Lithos, v. 198, p. 129–140.

Chiaradia, M., Schaltegger, U., Spikings, R., Wotzlaw, J.-F., and Octcharova, M., 2013, How accurately can we date the duration of magmatic-hydrother-mal intrusive events in porphyry systems?—An invited paper: Economic Geology, v. 108, p. 565–584.

Clairborne, L.L., Miller, C.F., Walker, B.A., Wooden, J.L., Mazdab, F.K., and Bea, F., 2006, Tracking magmatic processes through Zr/Hf ratios in rocks and Hf and Ti zoning in zircons: An example from the Spirit Mountain batholith, Nevada: Mineralogical Magazine, v. 70, p. 517–543.

Claypool, G.H., Holser, W.T., Kaplan, I.R., Sakai, H., and Zak, I., 1980, The age curves of sulfur and oxygen isotopes in marine sulfate and their mutual

interpretation: Chemical Geology, v. 28, p. 199–260.

Cline, J.S., and Bodnar, R.J., 1991, Can economic porphyry copper mineralization be generated by a typical calc-alkaline melt? Journal of Geophysical Research, v. 96, p. 8113–8126.

Cloos, M., 2001, Bubbling magma chambers, cupolas, and porphyry copper deposits: International Geology Review, v. 43, p. 285–311.

Cloos, M., Sapiie, B., Quarles van Ufford, A., Weiland, R.J., Warren, P.Q, and McMahon, T.P., 2005, Collisional delamination in New Guinea: The geotectonics of subducting slab breakoff: Geological Society of America Special Paper 400, 51 p.

Cooke, D.R., Hollings, P., and Walshe, J.L., 2005, Giant porphyry deposits: characteristics, distribution, and tectonic controls: Economic Geology, v. 100, p. 801–818.

Cooper, P., and Taylor, B., 1987, Seismotectonics of New Guinea: A model for arc reversal following arccontinent collision: Tectonics, v. 6, p. 53–68.

de Hoog, J.C.M., Hattori, K.H., and Hoblitt, 2004, Oxidized sulfur-rich mafic magma at Mount Pinatubo, Philippines: Contributions to Mineralogy and Petrology, v. 146, p. 750–761.

Dewey, J.F., and Bird, J.M., 1970, Mountain belts and the new global tectonics: Journal of Geophysical Research, v. 75, p. 2625–2647.

Dozy, J.J., 1939, Geological results of the Carstensz expedition, 1936: Leidsche Geologische Mededelingen, v. 11, p. 68–131.

Dilles, J.H., Kent, A.J.R., Wooden, J.L., Tosdal, R.M., Kolezar, A., Lee, R.G., and

Farmer, L.P., 2015, Zircon compositional evidence for sulfur-degassing from ore-forming arc magmas: Economic Geology, v. 110, p. 241–251.

Ferry, J., and Watson, E., 2007, New thermodynamic models and revised cali-brations for the Ti-in-zircon and Zr-in-rutile thermometers: Contributions to Mineralogy and Petrology, v. 154, p. 429–437.

Field, C.W., and Gustafson, L.B., 1976, Sulfur isotopes in the porphyry copper deposit at El Salvador, Chile: Economic Geology, v. 71, p. 1533–1548.

Field, C.W., Zhang, L., Dilles, J.H., Rye, R.O., and Reed, M.H., 2005, Sulfur and oxygen isotopic record in sulfate and sulfide minerals of early, deep, pre-main stage porphyry Cu-Mo and late main stage base-metal mineral deposits, Butte district, Montana: Chemical Geology, v. 215, p. 61–93.

Fu, B., Page, F.Z., Cavosie, A.J., Fournelle, J., Kita, N.T., Lackey, J.S., Wilde, S.A., and Valley, J.W., 2008, Ti-in-zircon thermometry: applications and limitations. Contributions to Mineralogy and Petrology, v. 156, p. 197–215.

Gibbins, S.L., 2006, The magmatic and hydrothermal evolution of the Ertsberg intrusion in the Gunung Bijih (Ertsberg) mining district, West Papua, Indonesia: Unpublished PhD. Dissertation, The University of Arizona, 384 p.

Halter, W.E., Heinrich, C.A., and Pettke, T., 2005, Magma evolution and the formation of porphyry Cu-Au ore fl uids: Evidence from silicate and sulfi de melt inclusions: Mineralium Deposita, v. 39, p. 845–863.

Hamilton, W.B., 1979, Tectonics of the Indonesian region: U.S. Geological Survey Professional Paper 1078, 345 p.

Harrison, T.M., Watson, E.B., Aikman, A.B., 2007, Temperature spectra of zircon

crystallization in plutonic rocks: Geology, v. 35, p. 635–638.

Hattori, K.H., 2018, Porphyry copper potential in Japan based on magmatic oxidation state: Resource Geology, v. 68, p. 126–137.

Hattori, K.H., and Keith, J.D., 2001, Contribution of mafic melt to porphyry copper mineralization: Evidence from Mount Pinatubo, Philippines, and Bingham Canyon, Utah, USA: Mineralium Deposita, v. 36, p. 799−806.

Hedenquist, J.W., and Lowenstern, J.B., 1994, The role of magmas in the formation of hydrothermal ore deposits: Nature, v. 370, p. 519–527.

Hedenquist, J.W., Arribas, A., and Aoki, M., 2017, Zonation of sulfate and sulfide minerals and isotopic composition in the Far Southeast porphyry and Lepanto epithermal Cu-Au deposits, Philippines: Resource Geology, v. 67, p. 174–196.

Henley, R.W., and McNabb, A., 1978, Magmatic vapor plumes and ground-water interaction in porphyry copper emplacement: Economic Geology, v. 73, p. 1–20.

Henley, R.W., and Seward, T.M., 2018, Gas-solid reactions in arc volcanoes: Ancient and modern: Reviews in Mineralogy and Geochemistry, v. 84, p. 309–349.

Henley, R.W., King, P.L., Wykes, J.L., Renggli, C.J., Brink, F.J., Clark, D.A., and Troitzsch, U., 2015, Porphyry copper deposit formation by sub-volcanic sulphur dioxide flux and chemisorption: Nature Geoscience, v. 8, p. 210–215.

Hildreth, W., and Moorbath, S., 1988, Crustal contributions to arc magmatism in the Andes of central Chile: Contributions to Mineralogy and Petrology, v. 98, p. 455–489.

Holland, H.D., 1965, Some applications of thermochemical data to problems of ore deposits II. Mineral assemblages and the composition of ore forming fluids: Economic Geology, v. 60, p. 1101–1166.

Hoskin, P.W.O., and Ireland, T., 2000, Rare earth element chemistry of zircon and its use as a provenance indicator: Geology, v. 28, p. 627–630.

Hoskin, P.W.O., and Schaltegger, U., 2003, The composition of zircon and igneous and metamorphic petrogenesis: Reviews in Mineralogy and Geochemistry, v. 53, p. 27–62.

Hutchinson, M.C., and Dilles, J.H., 2019, Evidence for magmatic anhydrite in porphyry copper intrusions: Economic Geology, v. 114, p. 14–152.

Imai, A., 2000, Mineral paragenesis, fluid inclusions and sulfur isotope systematics of the Lepanto Far Southeast Porphyry Cu-Au deposit, Mankayan, Philippines: Resource Geology, v. 50, p. 151–168.

Ishihara, S., 1977, The magnetite-series and ilmenite-series granitic rocks: Mining Geology v. 27, p. 293–305.

Iveson, A.A., Rowe, M.C., Webster, J.D., and Neill, O.K., 2018, Amphibole-, clinopyroxene- and plagioclase- melt partitioning of trace and economic metals in halogen-bearing rhyodacitic melts: Journal of Petrology, v. 59, p. 1579–1604.

Jacobs, D.C., and Parry, W.T., 1979, Geochemistry of biotite in the Santa Rita porphyry copper deposit, New Mexico: Economic Geology, v. 74, p. 860–887.

Jugo, P., Luth, R., and Richards, J., 2005, An experimental study of the sulfur content in basaltic melts saturated with immiscible sulfi de or sulfate liquids at 1300 °C and 1.0 GPa: Journal of Petrology, v. 46, p. 783–798.

Jugo, P.J., 2009, Sulfur content at sulfide saturation in oxidized magmas: Geology, v. 37, p. 415−418.

Kouzmanov, K., and Pokrovski, G.S., 2012, Hydrothermal controls on metal distribution in porphyry Cu (-Mo-Au) systems. Society of Economic Geology Special Publication, v. 16, p. 573–618.

Kusakabe, M., Komoda, Y., Takano, B., and Abiko, T., 2000, Sulfur isotopic effects in the disproportionation reaction of sulfur dioxide in hydrothermal fluids: implications for the δ34S variations of dissolved bisulfate and elemental sulfur from active crater lakes: Journal of Volcanology and Geothermal Research, v. 97, p. 287–307.

Kusakabe, M., Nakagawa, S., Hori, S., Matsuhisa, Y., Ojeda, J.M., and Serrano, L., 1984, Oxygen and sulfur isotopic compositions of quartz, anhydrite, and sulfide minerals from the El Teniente and Rio Blanco porphyry copper deposits, Chile: Bulletin of Geological Survey of Japan, v. 35, p. 583–614.

Large, S.J.E., von Quadt, A., Wotzlaw, J.-F., Guillong, M., and Heinrich, C.A., 2018, Magma evolution leading to porphyry Au-Cu mineralization at the Ok Tedi deposit, Papua New Guinea: trace element geochemistry and high-precision geochronology of igneous zircon: Economic Geology, v. 113, p. 39–61.

Leake, B.E., Woolet, A.R., Arps, C.E.S., Birch, W.D., Gilbert, M.C., Grice, J.D., Hawthorne, F.C., Kato, A., Kisch, H.J., and Krivovichev, E.A., 1997, Nomenclature of amphiboles: Report of the subcommittee on amphiboles of the International Mineralogical Association, Commission on New Min-erals

and Mineral Names: The Canadian Mineralogist, v. 35, p. 219–246.

Lee, R.G., Dilles, J.H., Tosdal, R.M., Wooden, J.L., and Mazdab, F.K., 2017, Magmatic evolution of granodiorite intrusions at the El Salvador porphyry copper deposit, Chile, based on trace element composition and U/Pb age of zircons: Economic Geology, v. 112, v. 245–273.

Leys, C.A., Cloos, M., New, B.T.E., and MacDonald, G.D., 2012, Copper-gold±molybdenum deposits of the Ertsberg-Grasberg district, Papua, Indonesia: Society of Economic Geology Special Publication, v. 16, p. 215–236.

Li, H., and Hermann, J., 2017, Chlorine and fluorine partitioning between apatite and sediment melt at 2.5 GPa, 800 °C: a new experimentally derived thermodynamic model: American Mineralogist, v. 102, p. 580–594.

Liang, H., Sun. W., Su, W., and Zartman, R.E., 2009, Porphyry copper-gold mineralization at Yulong, China, promoted by decreasing redox potential during magnetite alteration: Economic Geology, v. 104, p. 587–596.

Loader, M.A., Wilkinson, J.J., and Armstrong, R.N., 2017, The effect of titanite crystallisation on Eu and Ce anomalies in zircon and its implications for the assessment of porphyry Cu deposit fertility: Earth and Planetary Science Letters, v. 472, p. 107–119.

MacDonald, G.D., and Arnold, L.C., 1994, Geological and geochemical zoning of the Grasberg Igneous Complex, Irian Jaya, Indonesia: Journal of Geochemical Exploration, v. 50, p. 143–178.

Mavrogenes, J., and Blundy, J., 2017, Crustal sequestration of magmatic sulfur

dioxide: Geology, v. 45, p. 211–214.

McDonough, W.F., and Sun, S-s., 1995, The composition of the Earth: Chemical Geology, v. 120, p. 223–253.

McMahon, T., 1999, The Ertsberg intrusion and the Grasberg complex: Contrasting styles of magmatic evolution and Cu-Au mineralization in the Gunung Bijih (Ertsberg) mining district, Irian Jaya, Indonesia: Buletin Geologi, Jurusan Teknik Geologi–Institut Teknologi Bandung, v. 31, no. 3, p. 123–132.

Mernagh, T.P., Leys, C.A., and Henley, R.W., 2020, Fluid inclusion systematics in porphyry copper deposits: The super-giant Grasberg deposit, Indonesia, as a case study: Ore Geology Review, v. 123, p. 103–570.

Moore, W.J., and Czamanske, G.K., 1973, Compositions of biotites from unaltered and altered monzonite rocks in the Bingham Mining District, Utah: Economic Geology, v. 68, p. 269–274.

Mungall, J.E., 2002, Roasting the mantle: Slab melting and the genesis of major Au and Au-rich Cu deposits: Geology, v. 30, p. 915–918.

Muntean, J.L., and Einaudi, M.T., 2000, Porphyry gold deposits of the Refugio district, Maricunga belt, northern Chile: Economic Geology, v. 95, p. 1445–1472.

Mutch, E.J.F., Blundy, J.D., Tattitch, B.C., Cooper, F.J., and Brooker, R.A., 2016, An experimental study of amphibole stability in low-pressure granitic magmas and a revised Al-in-hornblende geobarometer: Contributions to Mineralogy and Petrology, v. 171, 27 p.

Naney, M.T., 1983, Phase equilibria of rock-forming ferromagnesian silicates in

granitic systems: American Journal of Science, v. 283, p. 993–1033.

New, B.T.E., 2006, Controls of copper and gold distribution in the Kucing Liar deposit, Ertsberg mining district, West Papua, Indonesia: Unpublished Ph.D. Dissertation, Queensland, James Cook University, 233 p.

Ohmoto, H., and Goldhaber, M.B., 1997, Sulfur and carbon isotopes. In: Barnes, H.L., ed., Geochemistry of hydrothermal ore deposits, 3rd edition: New York, John Wiley and Sons, p. 517–611.

Ohmoto, H., and Lasaga, A.C., 1982, Kinetics of reactions between aqueous sulfates and sulfides in hydrothermal systems: Geochimica et Cosmochimica Acta, v. 46, p. 1727–1745.

Ohmoto, H., and Rye, R.O., 1979, Isotopes of sulfur and carbon. In: Barnes, H.L., ed., Geochemistry of hydrothermal ore deposits, 2nd edition: New York, John Wiley and Sons, p. 509–567.

Parat, F., Holtz, F., and Streck, M.J., 2011, Sulfur-bearing magmatic accessory minerals: Reviews in Mineralogy and Geochemistry, v. 73, p. 285–314.

Peterson, J.T., and Cloos, M., 2005, Grasberg porphyry Cu-Au deposit, Papua, Indonesia: 1. Magmatic history, in Porter, T.M., eds., Super porphyry copper and gold deposits: a global perspective: PGC Publishing, Adelaide, p. 313–329.

Pokrovski, G.S., Kokh, M.A., Guillaume, D., et al., 2015, Sulfur radical species form gold deposits on Earth: Proceedings of the National Academy of Sciences of the United States of America, v. 112, p. 13484–13489.

Pollard, P.J., and Taylor, R.G., 2002, Paragenesis of the Grasberg Cu-Au deposit, Irian Jaya, Indonesia: results from logging section 13: Mineralium Deposita, v.

37, p. 117–136.

Richards, J.P., 2011, Magmatic to hydrothermal metal fluxes in convergent and collided margins: Ore Geology Reviews, v. 40, p. 1–26.

Richards, J.P., 2015, The oxidation state, and sulfur and Cu contents of arc magmas: implications for metallogeny: Lithos, v. 233, p. 27–45.

Richards, J.P., 2018, A shake-up in the porphyry world?: Economic Geology, v. 113, p. 1225–1233.

Ridolfi, F., Renzulli, A., and Puerini, M., 2010, Stability and chemical equi-librium of amphibole in calc-alkaline magmas: An overview, new thermo-barometric formulations, and application to subduction-related volcanoes: Contributions to Mineralogy and Petrology, v. 160, p. 45–66.

Rohrlach, B.D., and Loucks R.R., 2005, Multi-million-year cyclic ramp-up of volatiles in a lower crustal magma reservoir trapped below the Tampakan Cu-Au deposit by Mio-Pliocene crustal compression in the southern Philippines, in Porter, T.M., ed., Super porphyry copper and gold deposits: Porter Geoconsultancy Publishing, v. 2, p. 369−407.

Rubin, J.R., 1996, Skarn formation and ore deposition at the Gunung Bijih Timur (Ertsberg East) complex, Irian Jaya, Indonesia: Unpublished Ph.D. dissertation, University of Texas at Austin, 311 p.

Rusk, B., Reed, M., and Dilles, J.H., 2008, Fluid inclusion evidence for magmatic-hydrothermal fluid evolution in the porphyry copper-molybdenum deposit, Butte, Montana: Economic Geology, v. 103, p. 307–334.

Rye, R.O., 1993, The evolution of magmatic fluids in the epithermal environment:

the stable isotope perspective: Economic Geology, v. 88, p. 733–752.

Sapiie, B., and Cloos, M., 2004, Strike-slip faulting in the core of the Central Range of west New Guinea: Ertsberg mining district, Indonesia: Geological Society of America Bulletin: v. 116, p. 277–293.

Seedorff, E., Dilles, J.H., Proffett, J.M., Jr., Einaudi, M.T., Zurcher, L., Stavast, W.J.A., Johnson, D.A., and Barton, M.D., 2005, Porphyry deposits: Characteristics and origin of hypogene features: Economic Geology 100th Anniversary Volume, p. 251–298.

Selby, D., and Nesbitt, B.E., 2000, Chemical composition of biotite from the Casino porphyry Cu-Au-Mo mineralization, Yukon, Canada: evaluation of magmatic and hydrothermal fluid chemistry: Chemical Geology, v. 171, p. 77–93.

Shen, P., Hattori, K., Pan, H., Jackson, S., and Seitmuratova, E., 2015, Oxidation condition and metal fertility of granitic magmas: zircon traceelement data from porphyry cu deposits in the Central Asian Orogenic Belt: Economic Geology, v. 110, p.1861–1878.

Shinohara, H., and Hedenquist, J.W., 1997, Constraints on magma degassing beneath the Far Southeast porphyry Cu-Au deposit, Philippines: Journal of Petrology, v. 38, p. 1741−1752.

Sillitoe, R.H., 2010, Porphyry copper systems. Economic Geology, v. 105, p. 3–41.

Simon, A.C., Pettke, T., Candela, P.A., Piccoli, P.M., and Heinrich, C.A., 2004, Magnetite solubility and iron transport in magmatic–hydrothermal environments: Geochimica et Cosmochimica Acta, v. 68, p. 4905–4914.

Simon, A.C., Pettke, T., Candela, P.A., Piccoli, P.M., and Heinrich, C.A., 2006,

Copper partitioning in a melt vapor brine magnetite pyrrhotite assemblage: Geochimica et Cosmochimica Acta, v. 70, p. 5583–5600.

Sulaksono, A., Watanabe, Y., Arribas, A., Echigo, T., Al Furqan, R, Leys, C.A., 2021, Reduction of oxidized sulfur in the formation of the Grasberg porphyry copper-gold deposit, Papua, Indonesia: Mineralium Deposita, https://doi.org/10.1007/s00126-021-01040-9.

Sun, S., and McDonough, W.F., 1989, Chemical and isotopic systematics of oceanic basalts: implications for mantle composition and processes. In: Saunders, A.D., Norry, M.J. Eds., Magmatism in Ocean Basins. Geological Society Special Publication, London, pp. 313–345.

Sun, W.D., Arculus, R.J., Kamenetsky, V.S., and Binns, R.A., 2004, Release of gold-bearing fluids in convergent margin magmas prompted by magnetite crystallization: Nature, v. 431, p. 975–978.

Tatsumi, Y., 1989, Migration of fluid phases and genesis of basalt magmas in subduction zones: Journal of Geophysical Research, v. 94, p. 4697–4707

Tattitch, B.C., and Blundy, J.D., 2017, Cu–Mo partitioning between felsic melts and saline-aqueous fluids as a function of XNaCleq, $fO2$, and $fS2$: American Mineralogist, v. 102, p. 1987–2006.

Trail, D., Watson, E.B., and Tailby, N.D., 2012, Ce and Eu anomalies in zircon as proxies for the oxidation state of magmas: Geochimica et Cosmochimica Acta, v. 97, p. 70–87.

van Hoose, A.E., Streck, M.J., Pallister, J.S., and Wälle, M., 2013, Sulfur evolution of the 1991 Pinatubo magmas based on apatite: Journal of Volcanology and

Geothermal Research, v. 257, p. 72–89.

van Nort, S., Atwood, G.W., Collinson, T.B., Flint, D.C., and Potter, D.R., 1991, Geology and mineralization of the Grasberg porphyry copper-gold deposit, Irian Jaya, Indonesia: Mining Engineering, v. 43, p. 300–303.

von Quadt, A., Erni, M., Martinek, K., Moll, M., Peytcheva, I., and Heinrich, C.A., 2011, Zircon crystallization and the lifetimes of ore-forming magmatic-hydrothermal systems: Geology, v. 39, p. 731–734.

Wafforn, S., 2017, Geo- and thermochronology of the Ertsberg-Grasberg Cu-Au mining district, west New Guinea, Indonesia: Unpublished Ph.D. Dissertation, The University Texas at Austin, 357 p.

Wang, J., Hattori, K.H., Kilian, R., and Stern, C.R., 2007, Metasomatism of sub-arc mantle peridotites below southern South America: Reduction of fO2 by slab-melt: Contributions to Mineralogy and Petrology, v. 153, p. 607–624.

Watanabe, Y., Kon, Y., Echigo, T., and Kamei, A., 2017, Differential fractionation of rare earth elements in oxidized and reduced granitic rocks: Implication for heavy rare-earth enriched ion-adsorption mineralization. Resource Geology, v. 67, p. 35–52.

Watanabe, Y., Sato, R., and Sulaksono, A., 2018, Role of potassic alteration for porphyry Cu mineralization: Implication for the absence of porphyry Cu deposits in Japan: Resource Geology, v. 68, p. 195–207.

Watson, E.B., and Harrison, T.M., 1983, Zircon saturation revisited: Temperature and composition effects in a variety of crustal magma types: Earth and Planetary Science Letters, v. 64, p. 295–304.

Weis, P., 2015, The dynamic interplay between saline fluid flow and rock permeability in magmatic-hydrothermal systems: Geofluids, v. 15, p. 350–371.

Whitney, J.A., 1988, Composition and activity of sulfurous species in quenched magmatic gases associated with pyrrhotite-bearing silicic systems: Economic Geology v. 83, p. 86–92.

Wilke, M., and Behrens, H., 1999, The dependence of the partitioning of iron and europium between plagioclase and hydrous tonalitic melt on oxygen fugacity: Contributions to Mineralogy and Petrology, v. 137, p. 102–114.

Wilkinson, J.J., 2013, Triggers for the formation of porphyry ore deposits in magmatic arcs: Nature Geoscience, v. 6, p. 917–925.

Williams, T.J., Candela, P.A., and Piccoli, P.M., 1995, The partitioning of copper between silicate melts and two-phase aqueous fluids: an experimental investigation at 1 kbar, 800 °C and 0.5 kbar, 850 °C. Contributions to Mineralogy and Petrology, v. 121, p. 388–399.

Williams, T.J., Candela, P.A., and Piccoli, P.M., 1997, Hydrogen-alkali exchange between silicate melts and two-phase aqueous mixtures: an experimental investigation. Contributions to Mineralogy and Petrology, v. 128, p. 114–126.

Wilson, F.K., 1981, Conquest of Copper Mountain: New York, Atheneum Press, 243 p.

Wilson, M., 1989, Igneous petrogenesis: a global tectonic approach. Unwin Hyman, London, 466 p.

Wones, D.R., 1989, Significance of the assemblage titanite + magnetite + quartz in granitic rocks: American Mineralogist, v. 74, p. 744–749.

Zajacz, Z., Candela, P.A., Piccoli, P.M., Wälle, M., Sanchez-Valle, C., 2012, Gold and copper in volatile saturated mafic to intermediate magmas: solubilities, partitioning, and implications for ore deposit formation: Geochimica et Cosmochimica Acta, v. 91, p. 140–159.